Title
Wideband Cyclostationary Spectrum Sensing and Modulation Classification

Author
Rebeiz, Eric

Publication Date
2013

Peer reviewed|Thesis/dissertation

University of California

Los Angeles

Wideband Cyclostationary Spectrum Sensing and Modulation Classification

A dissertation submitted in partial satisfaction

of the requirements for the degree

Doctor of Philosophy in Electrical Engineering

by

Eric Rebeiz

2014

Abstract of the Dissertation

Wideband Cyclostationary Spectrum Sensing and Modulation Classification

by

Eric Rebeiz

Doctor of Philosophy in Electrical Engineering

University of California, Los Angeles, 2014

Professor Danijela Cabric, Chair

Wideband spectrum sensing is a key enabling functionality for Cognitive Radios (CRs) since it detects unoccupied bands and allows throughput increase. Due to prioritized spectrum sharing between CRs and primary owners of the spectrum, it is not only sufficient to detect occupancy but also distinguish among different users in order to manage interference. To realize this functionality in a practical radio, there are several implementation challenges that we address in this thesis: 1) high computational complexity and energy cost for the detection and classification of a broad range of communication signal types over a wideband spectrum, and 2) impact of wideband receiver impairments including nonlinearities, carrier and sampling offsets, and multipath.

The approach we take for joint sensing and classification is based on extracting and processing cyclostationary features of modulated signals. Conventionally, cyclostationary feature detectors are considered as robust detectors under noise uncertainties. However, estimation of cyclic features under constrained sensing time suffers from cyclic frequency offsets resulting from non-synchronous sampling and local oscillator offsets. We propose a new frame-based cyclic feature

estimator and optimize its frame length for a given carrier and sampling offset distribution. For identifying signals with unknown parameters in an energy efficient way, we develop a hierarchical reduced complexity cyclostationary-based classification algorithm by optimizing the search of cyclic features. The reduction in complexity and energy cost comes from discretization of feature space based on tolerable frequency offsets for the required classification accuracy. Next, we study the impact of wideband receiver nonlinearities on feature detection and show that performance loss depends on blockers strengths and modulation types. Based on this result, we devise a compensation algorithm that incorporates modulation classification into intermodulation terms cancellation. Finally, we investigate how the signal sparsity in the cyclic domain can be utilized to reduce the sampling rate requirements via a compressive sensing approach. As a result of the additional sparsity in the cyclic domain, our results show that a compression rate smaller than the conventional Landau rate can be achieved. In summary, this thesis provides a comprehensive analysis of cyclostationarity based sensing and classification under practical signal and radio conditions, and proposes a set of algorithms for a robust performance and energy-efficient implementation.

The dissertation of Eric Rebeiz is approved.

Mario Gerla

Ali H. Sayed

Greg Pottie

Danijela Cabric, Committee Chair

University of California, Los Angeles

2014

To my family.

Table of Contents

List of Figures

List of Tables

Acknowledgments

As most of my fellow colleagues would agree, going through a Ph.D. program is by no means a walk in the park. I believe the support and help of my friends and family played a tremendous role in my journey.

Growing up in Lebanon, I was taught to value education as once knowledge is acquired, it cannot be taken from me. I would like to thank my parents for their love and for nurturing me from halfway around the globe. My brother Paul has had an unwavering confidence in me from the start of my doctoral studies, and I will never forget the good memories in Los Angeles we shared together.

My gratitude goes to my advisor Professor Danijela Cabric for the great opportunity she has given me at UCLA. I thank her for both her motivation and criticism as they both were key elements in defining and executing my research goals. I am also grateful to the members of my doctoral committee, namely Ali H. Sayed, Greg Pottie, and Mario Gerla for their helpful feedback and suggestions.

I would like to thank my girlfriend Emily Dwyer from the bottom of my heart for her unconditional love, compassion, and support. Having Emily and our two dogs Reese and Ariel around was a fundamental part of my success in my journey, and for that I will always be thankful. My heart goes out to my colleagues at UCLA who I have spent countless hours with over the course of my Ph.D studies. My experience would have not been the same had I not been fortunate enough to be part of such a diverse and pleasant research group. I would like to thank Ali Shahed, Chun-Hao Liu, Fang-Li Yuan, Jason Tran, Jun Wang, Mihir Laghate, Paschalis Sofotasios, Paulo Urriza, Przemyslaw Pawelczak, Roja Bandari, Shaunak Joshi, Tsung-Han Yu, Varun Jain, and Wesam Gabran.

Finally, I would like to thank my the Defense Advanced Research Projects Agency (DARPA) who have funded me throughput my studies at UCLA. In addition, I would like to thank the Aerospace Corporation, in particular Philip Dafesh, for his interest in my research and for funding my Ph.D. studies.

Vita

2004–2008	B.Sc. in Electrical Engineering, University of Massachusetts Amherst, MA
2008–2009	M.Sc. in Electrical Engineering, University of Southern California, CA
Summer 2009	Systems Engineer, Qualcomm Inc., CA
2009–2010	Systems Engineer, ITT Exelis, CA
2011–2013	Member of the Technical Staff, The Aerospace Corporation, CA

Publications

E. Rebeiz, A. Shahed, M. Valkama, D. Cabric, Spectrum Sensing under RF Non-Linearities: Performance Analysis and DSP-Enhanced Receivers, submitted to IEEE Transactions on Signal Processing

E. Rebeiz, P. Urriza, D. Cabric, Optimizing Wideband Cyclostationary Spectrum Sensing under Receiver Impairments, IEEE Transactions on Signal Processing, vol. 61, no. 15, pp. 3931-3943, Aug. 2013

E. Rebeiz, F. Yuan, P. Urriza, D. Markovic, D. Cabric, Energy-Efficient Processor for Blind Signal Classification in Cognitive Radio Networks, to appear in IEEE Transactions Circuits and Systems I

E. Rebeiz, G. Caire, and A.F. Molisch, Energy-Delay Tradeoff and Dynamic Sleep Switching for Bluetooth-Like Body-Area Sensor Networks, IEEE Transactions Communications, vol. 60, no. 9, pp. 2733-2746, Sept. 2012

E. Rebeiz, D. Cabric, How wideband receiver nonlinearities impact spectrum sensing, in Proc. IEEE Global Conference on Signal and Information Processing, 3-5 Dec. 2013, Austin, TX, USA

E. Rebeiz, D. Cabric, Blind Modulation Classification Based on Spectral Correlation and Its Robustness to Timing Mismatch, in Proc. IEEE Military Communications Conference, 7-10 Nov. 2011, Baltimore, MD, USA

E. Rebeiz, D. Cabric, Low Complexity Feature-based Modulation Classifier and its Non-Asymptotic Analysis, in Proc. IEEE Global Communications Conference (GLOBECOM), 5-9 Dec. 2011, Houston, TX, USA

E. Rebeiz, A. Shahed, M. Valkama, and D. Cabric, Suppressing RF Front-End Nonlinearities in Wideband Spectrum Sensing, in Proc. IEEE Conference on Cognitive Radio Oriented Wireless Networks (CROWNCOM) 2013

E. Rebeiz, P. Urriza, D. Cabric, Experimental Analysis of Cyclostationary Detectors Under Cyclic Frequency Offsets, in Proc. Asilomar Conference on Signals, Systems and Computers 2012

E. Rebeiz, V. Jain and D. Cabric, Cyclostationary-Based Low Complexity Wideband Spectrum Sensing using Compressive Sampling, in Proc. IEEE International Conference on Communications, 10-15 Jun. 2012, Ottawa, Canada

P. Urriza, **E. Rebeiz**, D. Cabric, Multiple Antenna Cyclostationary Spectrum

Sensing Based on the Cyclic Correlation Significance Test, IEEE Journal on Selected Areas in Communications: Cognitive Radio Series, vol. 31, no. 11, pp. 2185–2195, Nov. 2013

P. Urriza, **E. Rebeiz**, P. Pawelczak, D. Cabric, Computationally Efficient Modulation Level Classification Based on Probability Distribution Distance Functions, IEEE Communications Letters, vol. 15, no. 5, pp. 476-478, May 2011

P. Urriza, **E. Rebeiz**, D. Cabric, Optimal Discriminant Functions Based On Sampled Distribution Distance for Modulation Classification, accepted for publication in IEEE Communications Letters

P. Sofotasios, **E. Rebeiz**, L. Zhang, T. Tsiftsis, S. Freear, D. Cabric, Energy Detection-Based Spectrum Sensing over Generalized and Extreme Fading Channels, in IEEE Transactions Vehicular Technology, vol. 62, no. 3, pp. 1031-1040, Mar. 2013

C-H. Liu, **E. Rebeiz**, P. Pawelczak, D. Cabric, Primary User Traffic Classification in Dynamic Spectrum Access Networks, in Proc. IEEE Globecom 2013

D. Cohen, **E. Rebeiz**, Y. Eldar, D. Cabric, Cyclostationary Detection from Sub-Nyquist Samples for Cognitive Radios and Minimal Sampling Rates, accepted to IEEE Fifth International Workshop on Computational Advances in Multi-Sensor Adaptive Processing, 15-18 Dec. 2013, Saint Martin

P. Urriza, **E. Rebeiz**, D. Cabric, Hardware Implementation of Kuiper-based Modulation Level Classification, in Proc. Asilomar Conference on Signals, Systems and Computers, 6-9 Nov. 2011, Pacific Grove, CA, USA

P. Urriza, **E. Rebeiz**, D. Cabric, Eigenvalue-based Cyclostationary Spectrum Sensing Using Multiple Antennas, accepted for publication in IEEE Global Communications Conference, 3-7 Dec. 2012, Anaheim, CA, USA

D. Cohen, **E. Rebeiz**, V. Jain, Y. Eldar, D. Cabric, Cyclostationary Feature Detection from Sub-Nyquist Samples, in Proc. IEEE Fourth International Workshop on Computational Advances in Multi-Sensor Adaptive Processing, 13-16 Dec. 2011, San Juan, Puerto Rico

D. Cohen, **E. Rebeiz**, Y. Eldar, D. Cabric, Cyclic Spectrum Reconstruction and Cyclostationary Detection from Sub-Nyquist Samples, in IEEE Proc. Signal Processing Advances in Wireless communications (SPAWC), 16-19 Jun. 2013, Darmstadt, Germany

CHAPTER 1

Introduction

The Radio Frequency (RF) spectrum has become a scarce resource as a result of higher data rate applications. Transitioning from voice-only to multimedia communications is further amplified by the explosive growth of mobile devices as a result of their decreasing cost. However, the RF spectrum resource is naturally limited due to both physics and electromagnetics. Without addressing this issue, the development of radio technologies become unsustainable.

In order to address the spectrum scarcity problem, innovative techniques must be developed with the aim of providing new and more efficient ways of utilizing the available spectrum. In several spectrum measurement campaigns [Yan05, SCZ10, WRP09, MTM06], it has been shown that the current fixed allocation of spectrum (such as that of the FCC, shown graphically in Fig. 1.1) is very inefficient as most channels are underutilized. One such result, from measurements done in Chicago, IL, is presented in Fig. 1.2. We observe that a significant portion of the spectrum allocated to licensed services shows little to no usage over time, with all observed channels being used $< 25\%$ of the time on average.

The Cognitive Radio (CR) concept was first proposed by Mitola [MM99], whereby a radio can adapt and dynamically reconfigure itself based on its RF environment. By making CRs flexible, the burden has been shifted from the analog to the digital side. After a decade of research, CRs have attracted a lot of interest have shown much promise. The main idea behind a CR is the exploitation of existing spectrum holes, which are licensed frequency bands that are not used by the Primary User (PU) at a given time and location. These spectrum holes are

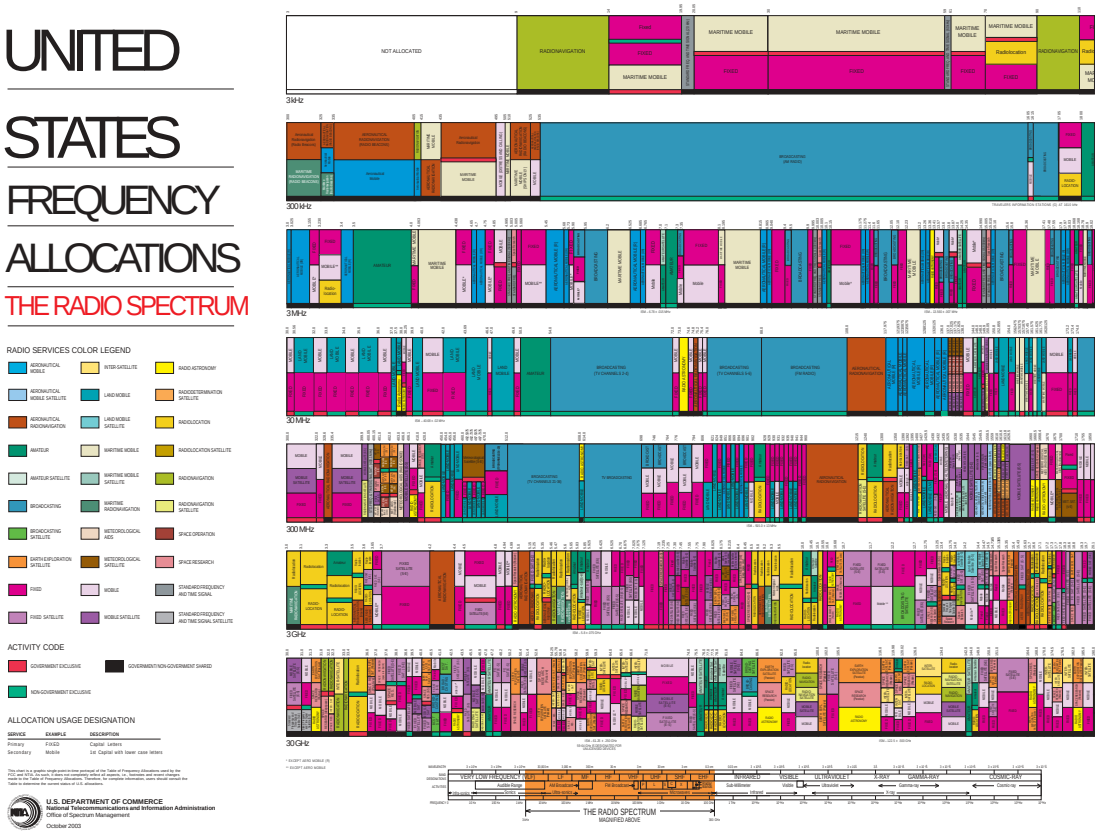

Figure 1.1: The NTIA's frequency allocation chart showing the fixed allocation of the radio spectrum.

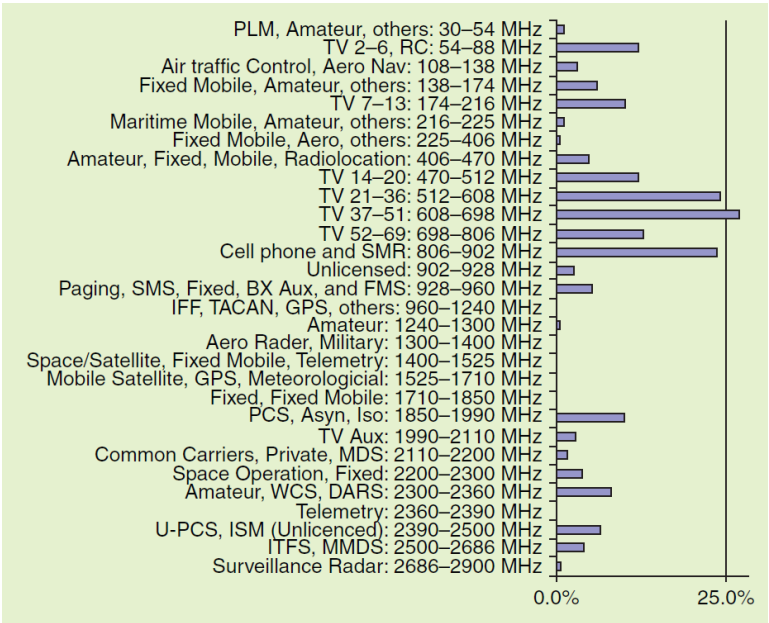

Figure 1.2: Average spectrum utilization taken over multiple locations [MTM06]

opportunities for a secondary user (SU), and can be exploited either temporally, spectrally, or spatially. Through CRs, the vision is to significantly improve the spectrum utilization and potentially eliminate the *false* scarcity problem caused by the static spectrum allocation.

1.1 Spectrum Sensing and Modulation Classification Overview

As CRs should avoid interfering with legacy users (PUs), detecting their presence before transmitting over any given channel. PU detection, which is also referred to as spectrum sensing, needs to be performed reliably in the low SNR regimes as a result of the near-far problem. With respect to different algorithmic techniques for spectrum sensing [YA09], energy detectors (ED) are the simplest to implement. In fact, ED [CMB04] estimate the energy in the subband of interest to determine whether the signal of interest (SOI) is present or not by comparing the estimated energy to a threshold. Although energy detectors require the least amount of information about the signal to be detected, they suffer from the noise uncertainty problem [TS08] when the noise floor cannot be estimated accurately. On the other hand, cyclostationary-based detectors (CD) [Gar88, DG94] rely on detection of hidden redundancies in the received signal. Cyclostationary detectors do not suffer from the noise uncertainty problem as they are able to asymptotically separate signal from noise by exploiting the noise stationarity, and are therefore more robust than energy detectors in this regard.

Modulation classification is an intermediate step between signal detection and demodulation, and helps in distinguishing PUs from other signals. Modulation classification algorithms can be split into two categories. Maximum likelihood (ML) algorithms [WM00b, PK90, HP95, BW98] require the distribution of the incoming samples, and are the optimal classifiers in the Bayesian sense as they minimize the probability of false classification given a finite number of

samples. However, the classification performance of ML algorithms degrades when uncertainties in the received signal arise. Further, ML classifiers require storing multi-dimensional probability distribution functions, and are therefore complex to implement in terms of storage. On the other hand, feature-based (FB) [SS00, NA98, YL98, SH92] algorithms use some statistical information about the incoming signal instead of relying on the complete probability distribution function. The algorithms of this class are less sensitive to uncertainties in the received signal model, are less complex to implement, but are sub-optimal classifiers. However, the loss in classification performance is usually offset by increasing the number of samples needed for classification.

Designing a FB algorithm relies on defining features that can be used to distinguish the modulations that are considered. In essence, FB classifiers form a higher dimensional space in which signals of different features can be separated by a hyperplane. One example of FB classifiers is the famous cumulants classifier such as the one presented in [SS00] where a hierarchical tree is presented to distinguish between one or more classes at each stage. Goodness of Fit (GoF) classifiers on the other hand use the probability distribution function of a given feature of the received samples as the feature used for classification. These kind of classifiers rely on knowing the distribution of the received signal under the different hypotheses, however they are more robust to modeling imperfections than ML classifiers. Other FB classifiers are cyclostationary-based classifiers which rely on the cyclic features of the signals for classification. The modulation type classifier proposed in this thesis falls in this category. We refer to the case when the symbol rate and carrier frequency of the signal to be classified are unknown as blind modulation classification. This problem is of particular significance especially with respect to the energy efficiency aspect of the modulation type classifier.

Blind modulation classifiers have numerous applications in current and future wireless networks. From an electronic surveillance point of view, military applications of blind modulation classifier include tracking the spectrum activ-

ity of specific users (often interferes or jammers) and learning their modulation classes. Blind modulation classification is therefore vital to electronic countermeasures in such hostile environments. Additionally, with the recent deployment of heterogeneous networks (HetNet) such as Long Term Evolution (LTE), modulation classification becomes part of interference management [LTY11, BLK12]. Multi-user detection is performed to support multiple overlapping transmissions in time and (or) frequency. Knowledge of the modulation type by means of modulation classification [DAB07] is necessary to demodulate the interfering signal [Mos96]. However, this application assumes that the transmitted signals are standard-compliant. In the future, as a result of spectrum under-utilization, Cognitive Radios (CRs) [Ram09] will adaptively change their transmission parameters and modulation schemes in order to opportunistically access the unused spectrum holes. In such future wireless applications, demodulation of these adaptively modulated signals would require *blind* modulation classification. For these highly adaptive radios, information about transmit parameters cannot be assumed. As a result, blind modulation classification approaches are of significant research interest.

1.2 Motivation and Challenges for Wideband Processing

Sensing wideband channels has many benefits when it comes to opportunistic spectrum allocation. First, wideband spectrum sensing would entail opportunistically occupying unused spectrum from multiple bands, i.e. ISM band, TV band, etc. Further, sensing over a wide range of frequencies increases the probability of finding unused spectrum, and therefore increases the CR throughput.

Wideband spectrum sensing can either be performed using a narrowband or wideband RF front-end. Narrowband RF front-ends allow the sensing radios to tune to a single subband at a time. In such an approach, sensing would require tuning of the local oscillator used for downconversion, and only a single channel

can be sensed at a time. On the other hand, wideband RF font-ends downconvert a wide range of frequencies to baseband, where the filtering is performed digitally. In such receivers, sensing multiple subbands would entail changing the filtering performed in DSP only while keeping the RF front-end fixed. For this reason, we focus in this thesis on the deployment of such wideband RF front-ends as sensing multiple subbands can be performed in a flexible manner through digital processing.

Although adopting a wideband front-end is appealing for both spectrum sensing and modulation classification, it unveils a whole new set of challenges that have not yet been considered. First, wideband processing is accompanied with wideband radio impairments such as frequency and sampling clock offsets and LNA nonlinearities, all of which need to be analyzed. Further, from the computational complexity point of view, an energy efficient method to detect and classify signals in a wideband spectrum needs to be addressed. Further, the energy consumption aspect is also problematic when it comes to the high-rate power hungry ADC needed to digitize the entire wideband spectrum. The following subsections will give a brief overview of each of these challenges that will be addressed in this thesis.

1.2.1 Wideband Spectrum Sensing Under Receiver Imperfections

Cyclostationary detectors require the knowledge of the signal's carrier frequency and symbol rate. The impact of radio imperfections such as IQ imbalance and phase noise on cyclostationary detection have been studied in [OD11, One09]. However, typical wideband radio receivers also suffer from frequency offsets which can occur as a result of local oscillator mismatch [DMR00], Doppler shifts, or when the exact carrier frequency of the band of interest is not perfectly known. These radio imperfections result in a frequency offset, often referred to as a Cyclic Frequency Offset (CFO). It has been shown that the detection performance

degrades with an increasing number of samples under a non-zero CFO [ZL10], which presents a challenge to cyclostationary detection in low SNR regimes where a large number of samples is needed to suppress the noise. However, none of the above mentioned works have proposed a solution to overcome the performance degradation due to these impairments.

In addition, Sampling Clock Offset (SCO) at the A/D sampling stage [FLP05] is another impairment that needs to be considered. The effects of the SCO have been shown to degrade the detection performance of cyclostationary detectors using the Spectral Correlation Function (SCF) as the test statistic [ZTD12, VRD10, TCB07]. In [ZTD10a], a solution to the SCO is proposed in a pilot based OFDM detection using the spectral correlation function as the test statistic, where the phase offset from one frame to the next is estimated and compensated for in the detection process. In [RC11a], a blind solution to the SCO problem has been proposed, where the symbol rate of the incoming signal is estimated, and the acquired samples are interpolated at the correct rate. The drawbacks of the resampling technique solution are twofold: interpolation is power costly, and the interpolation rate has to be modified for each signal of interest in the wideband channel, which becomes a computationally inefficient solution.

1.2.2 Energy-Efficient Processor for Blind Modulation Classification

A survey of commonly used modulation classifiers is given in [DAB05] and in the references within. The authors of [SS00] have proposed a hierarchical modulation classifier based on cumulants which are higher-order moments of the received information symbols. This algorithm requires perfect timing synchronization to extract information symbols, and is sensitive to the imperfect knowledge of the Signal to Noise Ratio (SNR). On the other hand, some modulation classification algorithms operate on over-sampled signals. Among such classifiers are cyclostationary-based modulation classifiers which classify signals based on the

cyclostationary features [Gar91]. For linearly modulated signals, these cyclostationary features are a function of the signal's symbol rate and carrier frequency. However, the main challenge of blind modulation classification is the absence of *a priori* information about the transmit parameters. As a result, the search for the features used for modulation-type classification[1] becomes very computationally demanding. One approach to efficiently solve blind classification is to first estimate signal parameters and then use cyclostationary based classifiers. As the signal parameters are estimated using a finite number of samples, an estimation error will be introduced. In order to minimize the total energy consumption of the modulation classifier, knowing the maximum tolerable estimation errors while meeting the required classification accuracy is necessary.

From the architectural point of view, although various *non-blind* classification algorithms have been studied and even implemented in Digital Signal Processing (DSP) [KKY03] and Software-Defined Radio (SDR) platforms [XSZ10], an efficient silicon realization that classifies multi-carrier, spread spectrum, and linearly modulated signals was never realized before. In addition, these classifiers require prior knowledge of the targeted signals, which make them unsuitable for real-time blind classifiers. In order to achieve high energy efficiency, realization of Application-Specific Integrated Circuits (ASICs) is desirable. However, due to diversity of modulation classes and algorithms for their classification, a heuristic ASIC design equipped with multiple dedicated modules − one for each signal class − would result in large area and suboptimal energy consumption due to the difficulty of hardware sharing.

[1]We use the term *modulation type* to refer to the modulation scheme of the signal (e.g. QAM, PSK), and the term *modulation level* to refer to its modulation order (e.g. 4-QAM, 16-QAM).

1.2.3 Wideband Spectrum Sensing under RF Nonlinearities

The effects of certain receiver front-end non-idealities such as phase noise [SVT09] and I/Q imbalance [VRK01] as well as sampling clock offset on the performance of signal detectors have been reported in a number of studies, e.g. [ZTD10b,VRD10]. These studies consider narrowband spectrum sensing, and their common assumption is that the receiver operates in its linear region. However, depending on the received power of the incoming signal, wideband sensing receivers might operate in a range where the RF front-end components such as Low Noise Amplifier (LNA) exhibit a non-linear behavior. Therefore, spurious frequencies in the form of harmonics, intermodulation (IM) and crossmodulation (XM) are generated [gha11, Raz10]. As a result, the presence of strong blockers, i.e. strong signals outside the subband of interest, in the wideband spectrum produces distortion terms that affect the detection performance in other subbands where weaker signals may reside [Raz10, MKH10, KH09]. Under such scenarios, the detection performance might be degraded, causing the CR network to either cause harmful interference to the PU, or to miss the opportunity to transmit in a vacant subband.

1.2.4 High-Rate High-Resolution ADC Design

Radios that operate over a channel bandwidth on the order of 500 MHz or more require high sampling rate A/D converters with large dynamic range due to in-band PU signals. However, high sampling rate A/D converters are hard to design and consume high power. In order to reduce sampling rate requirements, it is appealing to use a compressive sensing approach that samples wideband signals below the Nyquist rate, given that the received wideband signal is sparse in a given domain. Typical compressing sensing approaches such as the ones recently proposed compressive sensing analog front-end architectures such as the Analog to Information Converters (AIC) [LKD07], Modulated Wideband Converters

(MWC) [ME10, MC11, MCD11], and other parallel mixed-signal architectures such as [WP11, YH09, CZL09], all rely on the underutilization of the spectrum and exploit the signal sparsity in its spectral domain. However, as will be shown in this thesis, additional sparsity can be achieved in the cyclic domain. Further, compressive sampling requires signal reconstruction that is realized in DSP, and often involves solving complex optimizations such as Orthogonal Matching Pursuit (OMP) and the ESPRIT algorithm [FC11] which make them difficult to implement in VLSI.

1.3 Thesis Organization

In this thesis, we develop an analytical framework to characterize the performance and limitations of wideband spectrum sensing and modulation classification. In addition, we develop low-complexity DSP solutions that improve the performance of wideband spectrum sensing algorithms under the imperfections considered in this thesis. We discuss in Chapter 2 the design objectives of the sensing and classification algorithms, give an overview of the techniques used for spectrum sensing and modulation classification, and shed a light on the practical issues that have not yet been considered.

In Chapter 3, we theoretically analyze the impact of receiver imperfections such as carrier and sampling clock offset on the wideband cyclostationary-based detection performance. We propose a new multi-frame detection statistic based on the cyclic auto-correlation function. We study the optimum method for splitting of a given number of samples in order to yield the best average detection performance under both sampling clock and cyclic frequency offsets. The contributions of this work are three-fold. For the proposed detector, the optimum frame length and number of frames is formulated as a two-dimensional optimization problem and its performance is verified both theoretically and via numerical simulations. The developed optimization framework can be used to verify when

a gain in average detection performance can be obtained over the conventional detector for a given distribution of cyclic frequency and sampling clock offsets. Finally, the theoretical average probabilities of false alarm and detection of the proposed detector for any frame length and number of frames are derived for a given distribution of the cyclic frequency and sampling clock offsets.

In Chapter 4, we propose a blind modulation classification processor with high functional diversity and energy/area efficiency. This chapter presents a system level application to our findings in Chapter 3, and ties together the energy efficiency of blind modulation classification processors to the impact of cyclic frequency offsets on the classification accuracy. By jointly considering the algorithm and architecture layers, we first select computationally efficient parameter estimation and modulation classification algorithms. Then, we analyze the processing strategy of the processor by studying the inter-block dependencies in order to minimize the overall consumed energy.

The aim of Chapter 5 is to study the impact of receiver non-linearities on different spectrum sensing techniques. The contributions of this chapter are three-fold. We derive the theoretical false alarm and detection probabilities in closed-form for both energy and cyclostationary detection for nonlinear front-ends as a function of the sensing time, blocker and signal of interest power. We theoretically show the effect of different modulation classes of the blockers on the detection performance of both energy and cyclostationary detectors. Finally, we propose a novel digital IMD compensation scheme and show under what conditions detection performance gains can be achieved using the proposed method.

In Chapter 6, we consider a compressive sensing approach for wideband cyclostationary wideband spectrum sensing and study the tradeoffs between sampling rate reduction and increase in sensing time. The contributions of this chapter are twofold. We develop a closed-form low-complexity SCF reconstruction from sub-Nyquist samples which is applicable to any analog-front end compressive sensing modulator. The given algorithm reconstructs only useful spectral correlation

peaks used for detection, making it energy efficient and implementable in VLSI. Finally, we quantify the bounds on the minimum achievable compression ratio for a given spectral sparsity for both cyclostationary and energy detection, which guarantee the uniqueness of the reconstruction.

We dedicate Chapter 7 to analyzing the impact of fading on both spectrum sensing and modulation classification. In particular, we derive novel expressions for the performance of energy detectors in composite channel fading models that include both small-scale and large-scale fading. We also show the degradation in the classification probability due to multipath fading, and propose algorithmic solutions to improve the reliability of the proposed modulation classifier in the presence of multipath channels. Finally, the thesis is concluded in Chapter 8.

CHAPTER 2

System Model and Design Objectives

We consider a wideband channel consisting of multiple spectrally non-overlapping signals. In the context of CR spectrum sensing, we focus on the processing of a received wideband signal in a channel of bandwidth B centered at some carrier frequency. The approach and analysis considered here apply to any channel bandwidth. Given the time and energy constraints on the sensing stage, we consider a limited time window of length $T_{sense} = N_T T_s$ during which the sensing radio acquires a total number of N_T incoming samples, where T_s is the sampling period. Let $t \in [0, T_{sense}]$ denote the time variable, and assume that the wideband channel could be occupied by K PU signals $s_k(t)$ $\forall k \in [1, ..., K]$. Under hypothesis $\mathcal{H}_{k,0}, \mathcal{H}_{k,1}$, the k^{th} PU is defined as being absent or active, respectively. Therefore, the received wideband signal is given by

$$x(t) = \sum_{k=1}^{K} s_k(t) \ , \quad \text{where } 0 \leq t \leq T_{sense} \ \text{ and}$$

$$s_k(t) = \begin{cases} w_k(t) & \text{under } \mathcal{H}_{k,0} \\ \sum_{n=-\infty}^{\infty} \Re\{a_k(nT_k)p_k(t - nT_k)e^{j2\pi f_{c_k} t}\} + w_k(t), & \text{under } \mathcal{H}_{k,1}, \end{cases} \tag{2.1}$$

where $a_k(nT)$ and $p_k(t)$ are the transmitted information symbols and the pulse shaping filter of the k^{th} transmitted signal respectively, and $w_k(t)$ is the AWGN in the band occupied by the k^{th} transmitter. We assume transmitted information symbols with average power $\sigma^2_{a_k}$, a pulse shape filter $p_k(t)$ of unit energy, and we define the Signal to Noise Ratio by SNR $= \sigma^2_{a_k}/\sigma^2_{w_k}$ where $\sigma^2_{w_k}$ is the noise variance in the channel occupied by $s_k(t)$.

The objective is to design an energy efficient receiver that detects the presence of the signals in the wideband spectrum, and determines the modulation type of the signals present. Spectrum sensing takes as an input the digitized IQ samples of the wideband signal, and outputs a list of the signals occupying the wideband channel. Once detected, each signal can be classified using a modulation classification algorithm. As a result, modulation classification cannot be performed before detecting the presence of the signal to be classified.

2.1 Overview of Spectrum Sensing Techniques

We consider below a narrow-band signal $x[n]$ which can be thought of as the digitized samples of one of the subbands of the wideband channel.

Given a set of samples $x[n]$, energy detection is the simplest signal detector that can be implemented. The test statistic is computed by computing the average energy of the received signal $x[n]$, and by comparing it to a decision threshold γ_{ed}. Given a finite number of samples N, the test statistic is computed as follows

$$\mathcal{T}_{ed} = \frac{1}{N} \sum_{n=0}^{N-1} |x[n]|^2 . \tag{2.2}$$

When the samples $x[\cdot]$ are IQ samples of the entire wideband downconverted channel, then channelization is needed before energy detection can be performed. Channelization can be performed by passing the IQ samples through an FIR filter, or by means of an FFT which channelizes the wideband spectrum into non-overlapping frequency subbands. Once computed, the test statistic is compared to a threshold γ_{ed} which is a function of the noise power. When the noise power is perfectly known at the receiver in each of the subbands, the sensing time N and threshold γ_{ed} are set to meet the desired false alarm and detection probabilities

given by [QCP08]

$$N = \left(\frac{Q^{-1}(P_{fa}) - Q^{-1}(P_d)}{SNR} - Q^{-1}(P_{fa}) \right)^2, \tag{2.3}$$

$$\gamma_{ed} = \left(Q^{-1}(P_{fa}) \cdot \sqrt{N} + N \right) \cdot \sigma_w^2, \tag{2.4}$$

where σ_w^2 is the noise variance in the given band of interest, and $Q(\cdot)$ is the tail probability of a zero-mean unit-variance Gaussian random variable. However, energy detection becomes challenging at low SNR levels where the noise level is hard to quantify accurately. For this reason, energy detectors suffer from the so-called SNR wall problem [TS08] below which reliable signal detection is not possible.

Before defining how cyclostationary-based spectrum sensing is performed, we given an overview of what cyclostationarity stands for. A random process $r(t)$ is said to be second-order cyclostationary if its second order moments satisfy two conditions: its mean and autocorrelation are both periodic with the same period T. In the context of modulated signals, T is a function of the symbol period and the carrier frequency of the signal being processed. If we let $\mathbb{E}[r(t)] = \mu_r(t)$ and $\mathbb{E}[r(t)r(t+\tau)] = R_r(t,\tau)$, then $\mathbb{E}[r(t+T)] = \mu_r(t)$ and $R_r(t+T,\tau) = R_r(t,\tau)$ *iff* $r(t)$ is cyclostationary. Given a cyclostationary random process, its autocorrelation $R_r(t,\tau)$ can be expanded using the Fourier series as follows

$$R_r(t,\tau) = \sum_{\alpha} R_r^{\alpha}(\tau) e^{j2\pi\alpha t}, \tag{2.5}$$

where $\alpha = \ell/T$ for $\ell \in \mathbb{Z}$. In (2.5), $R_r^{\alpha}(\tau)$ is the projection of $R_r(t,\tau)$ onto the exponential basis function with frequency α, called the Cyclic Auto-Correlation (CAC) given by

$$R_r^{\alpha}(\tau) = \frac{1}{T} \int_{-\infty}^{\infty} R_r(t,\tau) e^{-j2\pi\alpha t} \, \mathrm{d}t. \tag{2.6}$$

The conjugate CAC $R_{r^*}^{\alpha}(\tau)$ is defined similarly to Eq. (2.6) with $R_r(t,\tau)$ replaced with $R_r^*(t,\tau) \triangleq E[r(t)r^*(t+\tau)]$, and is used for detecting cyclic features related

Table 2.1: Cyclic features for some modulation classes that occur for conjugate $(\cdot)^*$ and non-conjugate CAC.

Modulation	Peaks at (α,ν)
Class 1	$(\frac{1}{T}, 0)^*$
Class 2	$(\frac{1}{T}, 0)^*$, $(2f_c,0)$, $(2f_c \pm \frac{1}{T},0)$
Class 3	$(\frac{1}{T}, 0)^*$, $(2f_c \pm \frac{1}{2T},0)$

to the signals' symbol rates. In contrast, the non-conjugate CAC is used to detect cyclic frequencies at a function of the carrier frequency.

When the signal parameters such as the signal's symbol rate and carrier frequency are known, cyclostationary detection can be performed [DG94, ZTD10b]. This process involves finding the amount of correlation between the received signal and a frequency shifted version of itself. One method to detect the cyclic features of a received signal is by computing its Cyclic Auto-Correlation (CAC) function. Estimation of both conjugate and non-conjugate CAC at an integer lag ν using finite number of samples N results in non-asymptotic estimated CAC given by

$$\mathcal{T}^*_{cd} = R^{\alpha}_{x^*}(\nu) = \frac{1}{N}\sum_{n=0}^{N-1} x[n]x^*[n-\nu]e^{-j2\pi\alpha n T_s}, \tag{2.7}$$

$$\mathcal{T}_{cd} = R^{\alpha}_{x}(\nu) = \frac{1}{N}\sum_{n=0}^{N-1} x[n]x[n-\nu]e^{-j2\pi\alpha n T_s}, \tag{2.8}$$

where α is the cyclic frequency which is a function of the signal's symbol rate and carrier frequency, ν is the lag, and T_s is the sampling period. The resulting non-biased estimate of the CAC in (2.8) converges to the CAC defined in (2.6) as N tends to infinity.

Table 2.1 summarizes the cyclic features for the three targeted modulation classes [Gar91]. By using the present cyclic features, the modulation-type classifier can distinguish among three different classes of single-carrier modulation types: Class 1 = {M-PSK (M > 2), M-QAM}, Class 2 = {M-ASK}, and Class 3 = {GMSK}.

Similarly to energy detection, cyclostationary detection is followed by a threshold comparison to determine the presence or absence of the signal. However, unlike energy detection, cyclostationary detectors do not suffer from the SNR wall problem [TS08], and reliable signal detection can be guaranteed at low SNR with increased sensing time. Further, the present cyclic features of a signal can also be used to determine the modulation type of the received signal. This will be the basis of the modulation classifier proposed in our overall system design.

Another test statistic that can be used for cyclostationary detection and modulation classification is the Fourier transform of the CAC with respect to the lag variable ν, which is often referred to as the Spectral Correlation Function (SCF). This statistic is computed by cross-correlating the FFT of the received wideband signal with itself to form the following two-dimensional map

$$S_x(\alpha, f) = \frac{1}{N} \sum_{n=0}^{N-1} X_n(f - \frac{\alpha}{2}) X_n^*(f + \frac{\alpha}{2}), \tag{2.9}$$

where $X_n(\cdot)$ is the n^{th} FFT frame of the received signal $x[n]$, and N is the total number of frames over which the SCF is averaged. Unlike the CAC test statistic, the resolution of the cyclic frequency α in the SCF is determined by the FFT size. Once the SCF is estimated, the test statistic is computed at the cyclic frequency α_i and angular frequency f_i is computed as follows

$$\mathcal{T}_{cd} = |S_x(\alpha_i, f_i)|. \tag{2.10}$$

Another test statistic can be ontained by integrating the SCF over all angular frequencies, resulting in the following test statistic

$$\mathcal{T}_{cd} = \left| \int_{-f_s/2}^{f_s/2} S_x(\alpha_i, f) \, \mathrm{d}f \right|, \tag{2.11}$$

where f_s is the sampling rate. A table similar to Table 2.1 showing the location of the cyclic features in the SCF can be found in [RC11b]. As AWGN is a

widesense stationary process and exhibits no cyclic correlation, the SCF of noise asymptotically has no spectral features at $\alpha \neq 0$.

Let $\mathcal{T}$ be the computed test statistic used for signal detection, and γ be the decision threshold that $\mathcal{T}$ is compared against. We start by defining the following important metrics for signal detection:

$$\begin{aligned} P_{fa} &= \mathbb{P}\left(\mathcal{T} > \gamma \mid \mathcal{H}_0\right), \\ P_d &= \mathbb{P}\left(\mathcal{T} > \gamma \mid \mathcal{H}_1\right), \end{aligned} \tag{2.12}$$

where $\mathcal{H}_0$ and $\mathcal{H}_1$ are the hypotheses where the signal of interest is absent and present respectively. The aim of any signal detector is to meet the desired detection probability while maintaining the false alarm probability below a certain level.

Once the signal has been detected, the signal can then be classified. For linearly modulated signals, the present cyclic features can be utilized to determine the modulation type of the signal being processed as shown in Table 2.1. Other non-cyclic based features will be used to discriminate among OFDM, DSSS, and linearly modulated signals as will be shown in Chapter 4. The list of modulation types that the receiver needs to classify is listed below

M-QAM, M-PSK, M-ASK, GMSK, OFDM, DSSS,

where M refers to the modulation order of the single carrier signals.

2.2 Signal Detection and Classification with Known / Unknown Frequency Support

We consider two different architectural and algorithmic solutions to sensing and classfying depending on what is assumed to be known about the signal to be

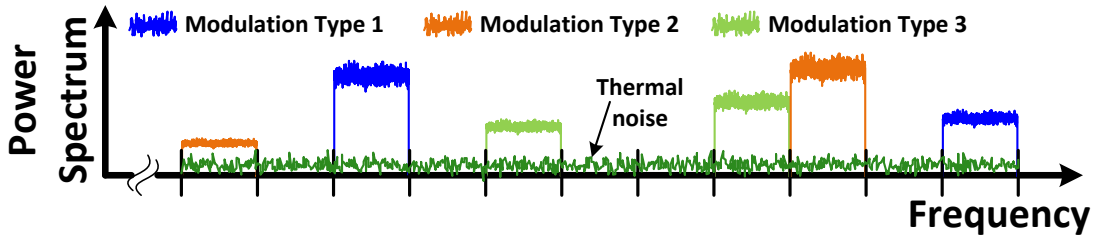

Figure 2.1: Example of a known frequency support spectrum sensing scenario with three different modulation types.

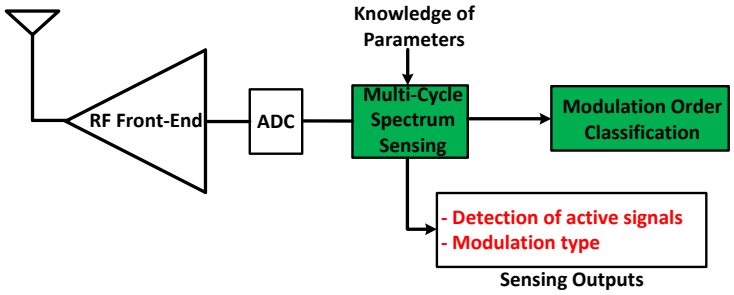

Figure 2.2: Signal detection and classification strategy with known frequency support.

detected and classified. When the the signal parameters are known, which can occur when the PUs follow a given IEEE communication standard, the receiver performs a multi-hypothesis cyclostationary detection to sense the presence of cyclic features to determine if the signal is present, and to determine its modulation type and order. This scenario is depicted in Fig. 2.1 where the frequency support is known to the sensing radio, i.e. there are a finite number of subbands to be sensed, each of which can be occupied by a user transmitting using a given modulation type to be classified. The process depicted in Fig. 2.2 consists of computing the test statistic (2.8) at all the cyclic frequencies given in Table 2.1, and by comparing them to a detection threshold. If any of the test statistics exceeds the decision threshold, a signal is said to be present. Then, depending on which of the cyclic features are present, the modulation type of the received signal can be estimated.

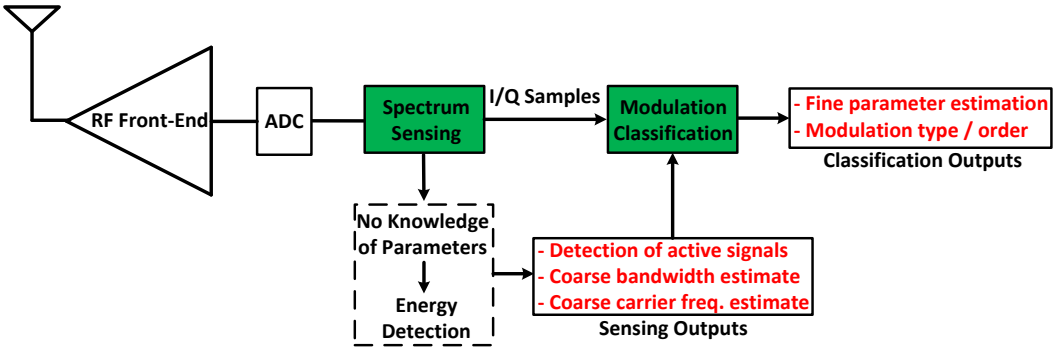

Figure 2.3: Signal detection and classification strategy with unkown frequency support.

Under certain scenarios, the signal parameters cannot be assumed to be known. This can occur in military settings, or in future heterogeneous wireless networks where users dynamically change their transmit paramters. Under such conditions, cyclic feature detection cannot be used directly for signal detection as the cyclic frequencies are function of a the signal's symbol rate and carrier frequency. Instead, the receiver has to rely on energy detection for signal detection, which will result in a coarse estimate of the symbol rate and carrier frequency of the present signals in the wideband channel. These parameters are later fed into a modulation classification engine which estimates the fine signal parameters, and then detects the present cyclic features of each of the signals to determine their modulation type and order. The algorithmic flow of such a receiver operating in blind mode is depicted in Fig. 2.3.

2.3 Practical Issues to Consider and Design Goal

Under the known frequency support scenario, the design strategy in Fig 2.2 assumes perfect knowledge of the transmit parameters, and therefore the cyclic detector can compute the CAC at the correct cyclic frequencies α. However, receiver impairments such as phase noise, phase jitter, frequency offsets, and Doppler shifts might result in a cyclic frequency offset (CFO). As a result, the

CAC will compute the test statistic at an offset from the true cyclic frequencies. Further, sampling clock offset that occurs at the ADC stage results in an computing the test statistic (2.8) using the wrong sampling period T_s. Further, these considerations are even worsened when the receiver is operating in its blind setting where the cyclic frequency offsets can even be larger due to inaccurate knowledge or coarse estimates of the transmit parameters. As a result, the performance of cyclostationary feature detectors and cyclic-based modulation classifiers will be affected under such circumstances. Furthermore, radios operating under both the known or unknown frequency support assumptions can suffer from nonlinearity issues as a direct result of utilizing a wideband receiver. In fact, strong blockers in the wideband blockers might create intermodulation terms that fall on top of weak signals that we wish to detect and classify, resulting in a loss in signal to noise and interference ratio. As a result, this behavior will degrade the detection performance and result in an increase in false alarm rate, and missing the opportunity of using vacant channels.

When the transmit parameters are unknown, the processor must detect and classify the received signal in real-time. As a result, the classification algorithms should have a low-complexity, and should output the results within a short sensing time. Therefore, a careful analysis of the tradeoffs between the different blocks of the modulation classifier is needed to find the absolute minimum sensing time required to meet the required classification accuracy. This design strategy will be utilized to design an energy-efficiency modulation classifier.

Finally, as wideband sensing requires high rate and high resolution ADCs which are hard to design and are power hungry devices, the total consumed energy of the proposed system will be high. In an effort to reduce the total sampling rate, a compressive sensing approach can be considered by exploiting the sparsity of the received signal in its cyclic domain. In order to exploit the sparsity in the cyclic domain, a theoretical framework needs to be laid out and analyzed in order to study the feasibility of such an approach, and to compare

it to the conventional compressive sensing solutions which rely on the sparsity of the wideband channel in the frequency domain.

The goal of this thesis is to design a robust and energy efficient spectrum sensing and modulation classification engine that meets the design objectives while being robust to the impairments of wideband receivers.

CHAPTER 3

Optimizing Wideband Cyclostationary Spectrum Sensing under Receiver Impairments

In this chapter, we investigate the impact of receiver nonidealities such as carrier frequency and sampling clock offsets on cyclostationary spectrum sensing. These two receiver impairments were not explicitely considered in our system model in Chapter 2. This chapter is organized as follows. In Section 3.1, we present our system model, and present the challenges to the conventional detector under frequency offsets. In Section 3.2, we present a novel multi-frame detector and study the effect of the considered impairments on the proposed detector. In Section 3.3, we derive the cyclic SNR under both considered impairments, which is the performance metric used to maximize the detection performance. In Section 3.4, the average theoretical cyclic SNR at the cyclic frequency of interest is optimized to solve for the best frame length and number of frames given the total number of acquired samples. Further, we derive the theoretical average detection performance of the proposed detector. We present the numerical results in Section 3.5 and compare the average detection performance of the proposed detector to the conventional detector. Finally, some concluding remarks are given in Section 3.6.

3.1 System Model and Problem Formulation

In this section, we develop our system model and pose the hypothesis testing problem for signal detection. We then give an overview of the conventional cyclostationary-based test statistic for spectrum sensing, and show the impact

of Cyclic Frequency Offsets (CFO) on the cyclic feature being detected.

3.1.1 System Model

We consider the signal model from Chapter 2 where the wideband signal could be occupied by K PU signals $x_k(t)$ $\forall k \in [1, ..., K]$ with residual carrier frequencies $f_{c_k} \neq 0$, symbol periods T_k, and known modulation classes, that we want to detect the presence of. Recall that each signal $x_k(t)$ has at least one modulation dependent cyclic frequency α_k that is used for signal detection. The received signal $r(t)$ is sampled with a nominal sampling period T_s, yielding the discrete time sequence

$$r[n] = \sum_{k=1}^{K} x_k[n], \text{where}$$

$$x_k[n] = \begin{cases} w_k[n] & \text{under } \mathcal{H}_{k,0}, \\ \sum_{\ell=-\infty}^{\infty} a_k(\ell T_k) p_\ell\big(nT_s(1+\delta_t) - \ell T_k\big) e^{j2\pi f_{c_k}(1+\delta_f)nT_s(1+\delta_t)} + w_k[n], & \text{under } \mathcal{H}_{k,1}, \end{cases} \tag{3.1}$$

where $a_k(\ell T_k)$ and $p_k(t)$ are the transmitted information symbols and the pulse shaping filter of the k^{th} PU respectively, and $w_k[n]$ is the complex AWGN in the band occupied by the k^{th} transmitter. We assume transmitted information symbols with unit average power, a pulse shape filter $p_k(t)$ of unit energy, and we define the Signal to Noise Ratio by $\text{SNR}_k = 1/\sigma_{w_k}^2$ where $\sigma_{w_k}^2$ is the noise variance in the channel occupied by $x_k(t)$. Further, δ_f is the frequency offset that arises from local oscillator drifts, Doppler shift, or imperfect knowledge of the carrier frequency. Finally, δ_t is defined as the the sampling clock offset (SCO) which arises from imperfect sampling rates at the A/D stage at the receiver. We denote $\tilde{T}_s = T_s(1 + \delta_t)$ the actual sampling period. Both impairments δ_f and δ_t are assumed to be fixed within the sensing interval, and vary from one sensing

interval to the next according to a given distribution. We note that fixing δ_t within the sensing interval is needed to yield a tractable theoretical analysis of the impairment.

Unlike narrowband detectors, the sampling rate at the A/D cannot be adapted to every signal being sensed in a wideband spectrum, and therefore the nominal sampling period T_s is kept the same for all K signals in the band of interest. We focus our attention on the detection of one of the K signals of interest with cyclic frequency α_k.

3.1.2 Impact of CFO on Conventional CAC and Problem Formulation

Given that cyclostationary detectors collect the energy of the received signal at a given cyclic frequency, the power of the cyclic feature determines the detection performance of the detector. In this section, we show the effect of CFO on the second moment of the non-asymptotic conventional CAC, which corresponds to the power of the cyclic feature. Given that signal and noise are assumed to be independent, the CAC of the signal and the noise will add up. Since noise is stationary process, we focus on studying the effect of CFO under noiseless conditions. Let α be the cyclic frequency at which the received signal exhibits a cyclic feature, and let $\hat{\alpha}$ be the cyclic frequency at which the sensing radio computes the CAC, where

$$\hat{\alpha} = (1 + \Delta_\alpha)\alpha. \tag{3.2}$$

The term Δ_α is referred to as the CFO. If the conjugate CAC is used for detecting cyclic features at the signal's symbol rate, then the CFO Δ_α can only arises from imperfect knowledge of the symbol rate as we are considering only impairments on the receiver side. If the non-conjugate CAC is used for detecting features at the signal's carrier such as at $\alpha = 2f_c$ (see Table 2.1), the CFO Δ_α is equal to δ_f and results from frequency offsets at the local oscillator, Doppler shifts,

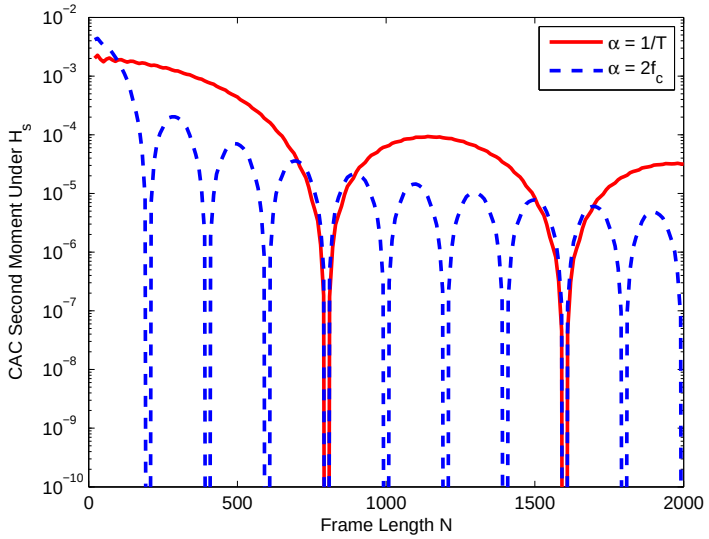

Figure 3.1: Effect of the cyclic frequency offset on the second order moment of the CAC under noiseless conditions for a BPSK signal for a CFO $\Delta_\alpha = 2 \times 10^{-2}$, with $f_c = 2.5$ MHz, $1/T = 1.25$ MHz, and $T_s = 1 \times 10^{-7}$s.

or from imperfect knowledge of the carrier frequency. Note that some signals exhibit a cyclic feature at a function of their symbol rate and carrier frequency. As a result, the CFO Δ_α will consist of both uncertainties in such a scenario. To illustrate the effect of CFO, we show the example of the effect of the cyclic frequency offset Δ_α on the cyclic features [ZL10] of a noiseless BPSK signal when the CFO $\Delta_\alpha = 1 \times 10^{-2}$ on cyclic frequencies $\alpha = 2f_c$ and $\alpha = 1/T$, where the carrier frequency is 2.5 MHz and the symbol rate is 1.25 MHz. Fig. 3.1 shows the degradation of the cyclic features as a function of number of samples N. As can be seen, the features get attenuated as N increases which would result in a degradation of the detection performance.

3.2 Proposed Multi-Frame CAC Test Statistic and Effect of SCO

We assume a total of N_T incoming samples acquired during a finite sensing time window of length $T_{sense} = N_T T_s$. Given that we are sensing a wideband channel,

the sampling period T_s is therefore not related to the signal bandwidth of interest, but rather to the bandwidth B of the channel being sensed.

As a solution to the CFO problem, we propose a novel frame-based CAC test statistic, where each frame is of length N samples, and where $M = \lfloor N_T/N \rfloor$ frames are used for statistical averaging. Thus, the spectrum sensing processor estimates the discrete non-asymptotic conjugate and non-conjugate multi-frame CAC based on MN samples as follows,

$$\tilde{R}^{\alpha}_{r^*}(\nu) = \frac{1}{MN}\sum_{m=1}^{M}\sum_{n=0}^{N-1} r_m[n]r_m^*[n-\nu]e^{-j2\pi\alpha n T_s},$$
$$\tilde{R}^{\alpha}_{r}(\nu) = \frac{1}{MN}\sum_{m=1}^{M}\sum_{n=0}^{N-1} r_m[n]r_m[n-\nu]e^{-j2\pi\alpha n T_s}, \tag{3.3}$$

where $r_m[\cdot]$ is the m^{th} frame of input samples, and M is the number of frames. Note that the conventional test statistic in (2.8) is a special case of (3.3), where N is replaced with N_T, and where $M = 1$. From a complexity point of view, the proposed detector has the same number of additions and multiplications as the conventional CAC, and therefore they both have the same computational complexity. Multiple frames are introduced in order to statistically average out the noise, and the frame length N is set in order to reduce the degradation of the cyclic feature due to the CFO. However, operating with $M > 1$ frames under (3.3) introduces a phase offset from one frame to the next when $N\alpha T_s$ is not an integer. In the next section, we derive the effect of the sampling clock offset on the proposed test statistic, and discuss the tradeoffs between the number of samples per frame N and the number of frames M.

3.2.1 Effect of Multi-Frame Processing and Sampling Clock Offset on Proposed Test Statistic

Due to its stationary property, noise will not be affected by the SCO, and therefore the noise CAC is independent of the SCO. For this reason, we focus on the effect

of the SCO in the noiseless case in the absence of CFO. From Eq. (3.3), in order to avoid non-coherent integration among multiple CAC frames, $N\alpha T_s$ should be an integer, which means that the CAC estimation is computed over an integer number of periods of the cyclic frequency α of interest within N samples. Let $\hat{T}_s$ be the sampling period such that $N\alpha\hat{T}_s$ is an integer. $\hat{T}_s$ is related to $\tilde{T}_s$ via

$$\tilde{T}_s = (1+e)\hat{T}_s, \tag{3.4}$$

where e denotes the residual offset. More formally, the residual offset e is defined as

$$e = \frac{N\alpha\tilde{T}_s}{\lfloor N\alpha\tilde{T}_s + 0.5 \rfloor} - 1. \tag{3.5}$$

Note that $\lfloor N\alpha\tilde{T}_s + 0.5 \rfloor$ is equivalent to rounding $N\alpha\tilde{T}_s$ to its nearest integer. We assume that $N\alpha\tilde{T}_s + 0.5 > 1$ for practical sensing times, and therefore e is always properly defined. If the sampling and detection is performed coherently, then $\tilde{T}_s = \hat{T}_s$, and therefore $e = 0$. Note that when $e = 0$, each frame of (3.3) can be represented as the DFT $Y_m[\alpha N\hat{T}_s]$ of the time sequence $y_m[n] = r_m[n]r_m^*[n-\nu]$,

$$Y_m[\alpha N\hat{T}_s] = \frac{1}{N}\sum_{n=0}^{N-1} y_m[n]e^{-\frac{j2\pi n(\alpha N\hat{T}_s)}{N}}. \tag{3.6}$$

Given that the SCO results in a drift in sampling times with respect to $y_m[n]$, the time-shift varies as n increases. Let $\tilde{y}_m[n]$ be a time-shifted version of $y_m[n]$, i.e, $\tilde{y}_m[n] = y_m[n-n_0]$. Their DFTs are related as follows:

$$\tilde{Y}_m[\eta] = Y_m[\eta]e^{-\frac{j\eta n_0}{N}}. \tag{3.7}$$

We use the time-shift property of the DFT to approximate the effect of the SCO on the multi-frame CAC. As an approximation, we consider the maximum time-shift mNe applied to all time samples $y_m[n]$ within one frame, where m varies

from 1 to M. Therefore, we obtain the following relationship

$$\begin{aligned}\tilde{Y}_m[\alpha N\tilde{T}_s] &= \left\{\frac{1}{N}\sum_{n=0}^{N-1} y_m[n]e^{-\frac{j2\pi n(\alpha N\tilde{T}_s)}{N}}\right\}e^{j2\pi\alpha\hat{T}_s Ne} \\ &= Y_m[\alpha N\hat{T}_s]e^{j2\pi\alpha\hat{T}_s Ne}. \end{aligned} \tag{3.8}$$

We let the multi-frame test statistic under non-zero SCO be denoted by $\hat{R}^{\alpha}_{r^*}(\nu)$, and obtain the following relationship

$$\begin{aligned}\hat{R}^{\alpha}_{r^*}(\nu) &= \frac{1}{MN}\sum_{m=1}^{M}\left\{\sum_{n=0}^{N-1} y_m[n]e^{-\frac{j2\pi\alpha nN\hat{T}_s}{N}}\right\}e^{-2\pi\alpha kN\hat{T}_s e} \\ &\simeq \tilde{R}^{\alpha}_{r^*}(\nu)\frac{\sin(\pi\alpha NMe\hat{T}_s)}{M\sin(\pi\alpha Ne\hat{T}_s)}e^{-j\pi e\alpha(M+1)} \\ &= \tilde{R}^{\alpha}_{r^*}(\nu)\frac{\sin(\pi\alpha NM\tilde{T}_s)}{M\sin(\pi\alpha N\tilde{T}_s)}e^{-j\pi e\alpha(M+1)} \\ &= \tilde{R}^{\alpha}_{r^*}(\nu)\frac{\sin\left(\pi\alpha NMT_s(1+\delta_t)\right)}{M\sin\left(\pi\alpha NT_s(1+\delta_t)\right)}e^{-j\pi e\alpha(M+1)} \end{aligned} \tag{3.9}$$

where the last equality is obtained by noting that $\tilde{T}_s = T_s(1+\delta_t)$ where δ_t is the SCO, and where we have used the fact that the test statistic converges to its true value within a single frame under noiseless conditions, and therefore $\sum_{n=0}^{N-1} y_m[n]e^{-\frac{j2\pi\alpha nN\hat{T}_s}{N}} \simeq \tilde{R}^{\alpha}_{r^*}(\nu)$, whereas the summation of M frames results in the decaying factor since $N\alpha T_s(1+\delta_t)$ is a non-integer. From (3.9), we can see that when $M = 1$ which coincides with the conventional detector, or when $M > 1$ and $\alpha N\tilde{T}_s$ is an integer, the SCO has no effect on the cyclic features. The same result obtained in (3.9) holds for the non-conjugate CAC as it holds for any $y_m[n]$. Note that even when $\delta_t = 0$, the multi-frame processing can cause degradation to the cyclic feature if $N\alpha T_s$ is not an integer.

In Fig. 3.2(a) we show the effect of the SCO δ_t on the cyclic features of a BPSK under noiseless conditions and $M = 3$ frames when $N\alpha T_s$ is an integer, where the vector composed of the cyclic features has been normalized to unit energy for illustration purposes. We note that the theoretical curves match the

ones obtained by simulation, which validates the approximation made in (3.9) for reasonable values of the SCO δ_t ranging from 0 to 5000 ppm.

After having studied the effect of the deterministic SCO on the test statistic under noiseless conditions, we focus now on its effect under the presence of noise. We numerically evaluate the detection probability of the single cycle detector which detects the cyclic feature at $\alpha = 2f_c$ in order to show the degradation in detection performance under non-zero SCO. Fig. 3.2(b) shows the effect of the SCO on the detection probability of a BPSK signal while maintaining a constant false alarm (CFAR) of 0.1 at a fixed SNR = 5 dB, when $N\alpha T_s$ is an integer. The detection probability drops to as low as 0.3 periodically, and the rate at which the dip occurs increases with increasing M.

We wish to emphasize that the effect of the SCO in the multi-frame detector on the cyclic features can be overcome by resampling every narrowband signal independently such that the resulting residual offset $e = 0$. However, due to the SCO δ_t which is unknown at the receiver, truly reducing e to zero would be impossible. In addition, since we are interested in sensing multiple signals simultaneously with different cyclic frequencies α, this solution would require either additional hardware complexity and power consumption, or additional sensing delay. In fact, multiple receiver chains can be deployed where each chain is responsible for resampling and sensing a given signal, therefore reducing it to the narrow-band approach for wideband sensing which is costly. The other alternative is to resample and sense sequentially, which increases the delay of the sensing, and therefore reduces the probability of finding unused spectrum.

Our objective is to compensate for the effects of SCO and CFO without filtering and resampling each signal in the wideband channel. In order to suppress the SCO effect, collecting the samples in a single frame achieves the best performance. However, increasing the number of samples per frame degrades the cyclic features under CFO. Therefore, there exists a tradeoff between the frame length and number of frames. In order to find the best split of samples under

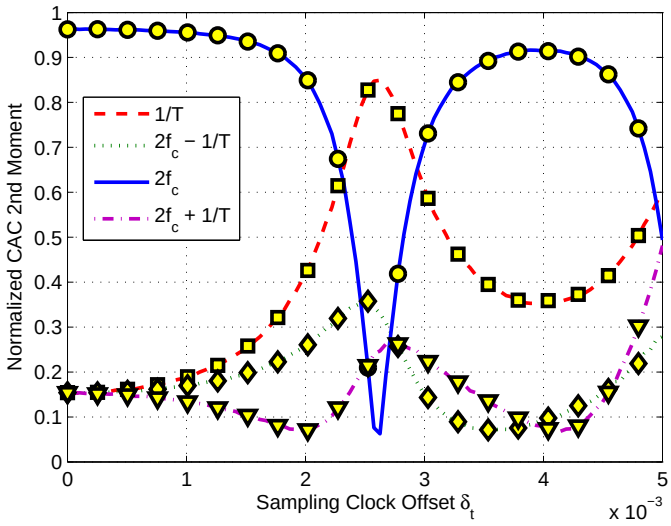

(a) Normalized feature vector of a BPSK signal in noiseless conditions with N = 256, M = 3. Solid lines represent simulation results, and markers represent the theoretical derivations.

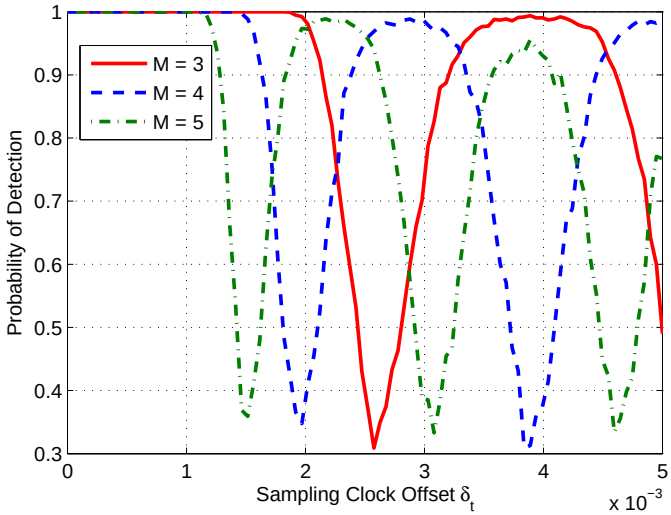

(b) Probability of detection of a BPSK signal under a CFAR = 0.1 with N = 256 samples, at SNR of 5 dB for varying averaging frames M.

Figure 3.2: Effect of sampling clock offset on the cyclic features of a BPSK signal, and the corresponding effect on the detection performance with $f_c = 2.5$ MHz, $1/T = 1.25$ MHz, and $T_s = 1 \times 10^{-7}$s.

the considered impairments, we start by deriving the cyclic SNR. The cyclic SNR is defined as the ratio of the test statistic power under the signal-only case at a given cyclic frequency, to that under $\mathcal{H}_0$ given a sampling clock offset δ_t and a

cyclic frequency offset Δ_α.

3.3 Theoretical Cyclic SNR of the Multi-Frame Statistic under Frequency and Sampling Clock Offsets

Since the detection performance is determined by the cyclic SNR, optimizing the sensing performance requires deriving the cyclic SNR under the considered impairments. Mathematically, we define the cyclic SNR at a cyclic frequency α_k using the conjugate statistic, without loss of generality, given a SCO δ_t and CFO Δ_α as

$$\mathrm{SNR}_{\alpha_k|\delta_t,\Delta_\alpha} = \frac{\mathbb{E}[|\hat{R}_{s^*}^{\alpha_k}(\nu)|^2]}{\mathbb{E}[|\hat{R}_{w^*}^{\alpha_k}(\nu)|^2]}, \tag{3.10}$$

where the noiseless signal of interest for a given signal index k under no impairment is denoted by $s[n]$ and given by

$$s[n] = \sum_{\ell=-\infty}^{\infty} a_k(\ell T_k) p_\ell\big(nT_s(1+\delta_t) - \ell T_k\big) e^{j2\pi f_{c_k}(1+\delta_f)nT_s(1+\delta_t)}. \tag{3.11}$$

The above definition can also be used for the non-conjugate multi-frame statistic. In order to analytically derive the cyclic SNR of the proposed test statistic, we start by finding the non-asymptotic second moments of the multi-frame test statistic under no impairments in Section 3.3.1 and 3.3.2. Then, we derive the theoretical moments under the considered impairments in Section 3.3.3, and theoretically find the cyclic SNR for a given realization of δ_t and Δ_α in Section 3.3.4.

3.3.1 Theoretical Moments of the CAC under $\mathcal{H}_0$

In this section, we find the theoretical second moment of the conjugate and non-conjugate multi-frame test statistic under $\mathcal{H}_0$, namely, $\mathbb{E}[|\hat{R}_{w^*}^{\alpha_k}(\nu)|^2]$ and

$\mathbb{E}[|\hat{R}_w^{\alpha_k}(\nu)|^2]$.

The derivation of the theoretical moments is given in Appendix A.1, and the results are summarized below for convenience. For the conjugate multi-frame CAC, the second moment for zero lag ν is given by

$$\mathbb{E}[|\hat{R}_{w^*}^{\alpha_k}(0)|^2] = \frac{\sigma_w^4}{MN} + \frac{\sigma_w^4 \sin^2(\pi\alpha_k NT_s)}{N^2 \sin^2(\pi\alpha_k T_s)}. \tag{3.12}$$

Similarly, for the non-conjugate multi-frame CAC, the second moment is given by

$$\mathbb{E}[|\hat{R}_w^{\alpha_k}(0)|^2] = \frac{2\sigma_w^4}{MN}. \tag{3.13}$$

It is worth noting that the second term in (3.12) can be omitted for the conjugate statistic since $\alpha_k \ll 1/T_s$, and therefore $\alpha_k T_s \ll 1$ in wideband channels. As a result, the moments of both conjugate and non-conjugate multi-frame statistics are a function of the product of M and N, which implies that the way the samples are split does not affect the second moment of the proposed statistic under $\mathcal{H}_0$. Under non-zero lag ν, the second moment of both conjugate and non-conjugate multi-frame CAC are given by

$$\mathbb{E}[|\hat{R}_w^{\alpha_k}(\nu)|^2] = \mathbb{E}[|\hat{R}_{w^*}^{\alpha_k}(\nu)|^2] = \frac{\sigma_w^4}{MN}, \forall \nu \neq 0. \tag{3.14}$$

3.3.2 Theoretical Moments of the Multi-Frame CAC under Noiseless Conditions and under No Impairments

Next, we find the theoretical second moment of the multi-frame test statistic under noiseless conditions. Given that we have derived in (3.9) the relationship between the multi-frame test statistic under SCO to the statistic without impairments, we focus here on deriving the theoretical moment of the tests statistic under no impairments. Therefore, we assume in this section that the CFO

$\Delta_\alpha = 0$, and $NT_s\alpha$ is an integer with $\delta_t = 0$.

Let $u_2 \triangleq \mathbb{E}[|a|^2]$ and $u_4 \triangleq \mathbb{E}[|a|^4]$. The theoretical second moment of the multi-frame statistic under noiseless conditions is derived in Appendix A.2, and the final expressions are given below for both conjugate and non-conjugate moments

$$\mathbb{E}[|\hat{R}_{s^*}^{\alpha_k}(\nu)|^2] = \frac{P_4}{MN^2}[u_4 - u_2^2] + \frac{|P_2|^2 u_2^2}{N^2}, \tag{3.15}$$

$$\mathbb{E}[|\hat{R}_{s}^{\alpha_k}(\nu)|^2] = \frac{P_4}{MN^2}[u_4 - u_2^2] + \frac{|P_2^{'}|^2 u_2^2}{N^2}, \tag{3.16}$$

where we have defined $\mathcal{L} = T/T_s$ as the oversampling ratio, and defined the following functions

$$\begin{aligned} g(n_1, n_2, \nu) = & p\left(\frac{n_1 T}{\mathcal{L}} - \left\lfloor \frac{n_1}{\mathcal{L}} \right\rfloor T\right) p\left(\frac{n_1 T}{\mathcal{L}} - \left\lfloor \frac{n_1}{\mathcal{L}} - \frac{\nu}{T} \right\rfloor T\right) \times \\ & p\left(\frac{n_2 T}{\mathcal{L}} - \left\lfloor \frac{n_2}{\mathcal{L}} \right\rfloor T\right) e^{-j2\pi\alpha_k(n_1 - n_2)T_s} \times \\ & p\left(\frac{n_2 T}{\mathcal{L}} - \left\lfloor \frac{n_2}{\mathcal{L}} - \frac{\nu}{T} \right\rfloor T\right), \end{aligned} \tag{3.17}$$

from which we obtain the following parameters

$$\begin{aligned} P_2 &= \sum_{n=0}^{N-1} p\left(\frac{nT}{\mathcal{L}} - \left\lfloor \frac{n}{\mathcal{L}} \right\rfloor T\right) p\left(\frac{nT}{\mathcal{L}} - \left\lfloor \frac{n}{\mathcal{L}} - \frac{\nu}{T} \right\rfloor T\right) e^{-j2\pi\alpha_k nT_s}, \\ P_4 &= \sum_{n=0}^{N-1} g(n, n, \nu), \end{aligned} \tag{3.18}$$

$$\begin{aligned} P_2^{'} = & \sum_{n=0}^{N-1} p\left(\frac{nT}{\mathcal{L}} - \left\lfloor \frac{n}{\mathcal{L}} \right\rfloor T\right) p\left(\frac{nT}{\mathcal{L}} - \left\lfloor \frac{n}{\mathcal{L}} - \frac{\nu}{T} \right\rfloor T\right) \times \\ & e^{-j2\pi(\alpha_k - 2f_{c_k})nT_s}. \end{aligned} \tag{3.19}$$

With the theoretical moments in the absence of the considered impairments, we now derive the moments under both CFO and SCO.

3.3.3 Theoretical Moments of the Multi-Frame CAC under Noiseless Conditions in the presence of CFO and SCO

Given a CFO $\Delta_\alpha \neq 0$ and a SCO $\delta_t = 0$, the multi-frame test statistic is computed at $\hat{\alpha} = \alpha(1 + \Delta_\alpha)$. It can be shown that P_2 defined in (3.18) can be written in a more general form under non-zero CFO as

$$\begin{aligned}\hat{P}_2 &= \sum_{n=0}^{N-1} p\left(\frac{nT}{\mathcal{L}} - \left\lfloor \frac{n}{\mathcal{L}} \right\rfloor T\right) p\left(\frac{nT}{\mathcal{L}} - \left\lfloor \frac{n}{\mathcal{L}} - \frac{\nu}{T} \right\rfloor T\right) e^{-j2\pi\hat{\alpha}_k nT_s} \\ &= P_2 \frac{\sin(\pi\alpha_k N\Delta_\alpha T_s)}{N\sin(\pi\alpha_k\Delta_\alpha T_s)}. \end{aligned} \tag{3.20}$$

Similarly, $P_2^{'}$ in (3.19) under a non-zero CFO can be expressed as

$$\hat{P}_2^{'} = P_2^{'} \frac{\sin(\pi\alpha_k N\Delta_\alpha T_s)}{N\sin(\pi\alpha_k\Delta_\alpha T_s)}. \tag{3.21}$$

Therefore, under a given realization of the CFO Δ_α, Eq. (3.15) and (3.16) can be generalized as

$$\begin{aligned}\mathbb{E}[|\hat{R}_{s^*}^{\alpha_k}(\nu)|^2 \mid \Delta_\alpha] &= \frac{P_4}{MN^2}[u_4 - u_2^2] + \frac{|P_2|^2 u_2^2 \sin(\pi\alpha_k N\Delta_\alpha T_s)^2}{N^4 \sin(\pi\alpha_k\Delta_\alpha T_s)^2} \\ \mathbb{E}[|\hat{R}_{s}^{\alpha_k}(\nu)|^2 \mid \Delta_\alpha] &= \frac{P_4}{MN^2}[u_4 - u_2^2] + \frac{|P_2^{'}|^2 u_2^2 \sin(\pi\alpha_k N\Delta_\alpha T_s)^2}{N^4 \sin(\pi\alpha_k\Delta_\alpha T_s)^2} \end{aligned} \tag{3.22}$$

Finally, from (3.9), under a given realization of the SCO δ_t, the theoretical second moment of the multi-frame CAC under non-zero CFO and SCO can be expanded as

$$\begin{aligned}\mathbb{E}[|\hat{R}_{s}^{\alpha_k}(\nu)|^2 \mid \delta_t, \Delta_\alpha] &= \left(\frac{P_4}{MN^2}[u_4 - u_2^2] + \right. \\ &\left. \frac{|P_2^{'}|^2 u_2^2 \sin(\pi\alpha_k N\Delta_\alpha T_s(1+\delta_t))^2}{N^4 \sin(\pi\alpha_k\Delta_\alpha T_s(1+\delta_t))^2}\right) \frac{\sin^2(\pi\alpha_k NMT_s(1+\delta_t))}{M^2\sin^2(\pi\alpha_k NT_s(1+\delta_t))}, \end{aligned} \tag{3.23}$$

$$\begin{aligned}\mathbb{E}[|\hat{R}_{s^*}^{\alpha_k}(\nu)|^2 \mid \delta_t, \Delta_\alpha] &= \left(\frac{P_4}{MN^2}[u_4 - u_2^2] + \right. \\ &\left. \frac{|P_2|^2 u_2^2 \sin(\pi\alpha_k N\Delta_\alpha T_s(1+\delta_t))^2}{N^4 \sin(\pi\alpha_k\Delta_\alpha T_s(1+\delta_t))^2}\right) \frac{\sin^2(\pi\alpha_k NMT_s(1+\delta_t))}{M^2\sin^2(\pi\alpha_k NT_s(1+\delta_t))}. \end{aligned} \tag{3.24}$$

With the theoretical seconds moments of the multi-frame test statistic under noise only and signal only, we now find the theoretical cyclic SNR under non-zero SCO δ_t and CFO Δ_α.

3.3.4 Theoretical Cyclic SNR under SCO and CFO

Although we have derived the second-order moments of the multi-frame proposed statistic under arbitrary ν, we devote the remainder of the theoretical results to deriving the theoretical average detection performance specifically at lag $\nu = 0$ as given in Table 2.1. A similar analysis can be performed for non-zero lag detection given the theoretical results derived in the appendices. Using the derived statistics in Eq. (3.12) and (3.24) and the definition of cyclic SNR in (3.10), the cyclic SNR at lag $\nu = 0$ for the conjugate multi-frame test statistic can be expressed as

$$\begin{aligned}\mathrm{SNR}_{\alpha_k|\delta_t,\Delta_\alpha} = &\frac{P_4[u_4 - u_2^2]\sin^2(\pi\alpha_k NMT_s(1+\delta_t))}{2NM^2\sigma_w^4\sin^2(\pi\alpha_k NT_s(1+\delta_t))} \quad + \\ &\frac{|P_2|^2u_2^2\sin^2(\pi\alpha_k N\Delta_\alpha T_s(1+\delta_t))\sin^2(\pi\alpha_k NMT_s(1+\delta_t))}{2N^3M\sigma_w^4\sin^2(\pi\alpha_k\Delta_\alpha T_s(1+\delta_t))\sin^2(\pi\alpha_k NT_s(1+\delta_t))}.\end{aligned} \tag{3.25}$$

In Fig. 3.3(a), we verify our intuition about the tradeoffs in splitting the acquired samples, and plot the theoretical cyclic SNR of a BPSK signal at cyclic frequency $\alpha = 2f_c$ under SNR = -5 dB, $N = 256$ samples, and $M = 10$ averages as a function of both SCO δ_t and CFO Δ_α, when $N\alpha T_s$ is an integer. In addition, the cyclic SNR is shown in Fig. 3.3(b) under the same CFO and SCO values using the same number of samples $N_T = 2560$, but using $N = N_T$ and $M = 1$. These two figures illustrate the tradeoffs between the conventional and the proposed multi-frame detector: the conventional test statistic is robust to SCO but degrades with CFO, and the multi-frame test statistic varies with both SCO and CFO. The aim of the next section is to find the best frame length that maximizes the average cyclic SNR given the distribution of the CFO and the SCO.

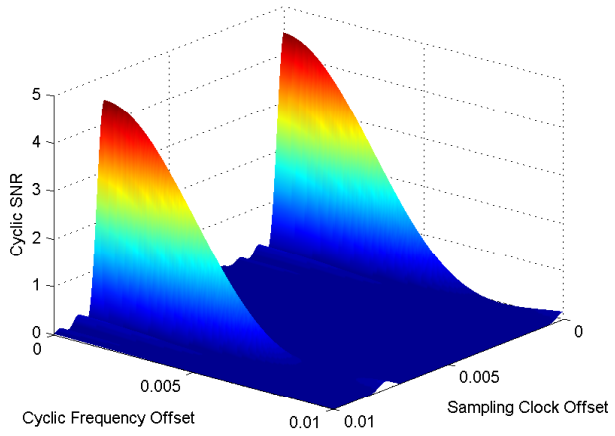

(a) Theoretical cyclic SNR at cyclic frequency $\alpha = 2f_c$ for a BPSK signal at SNR = -5 dB as a function of cyclic frequency offsets Δ_α and sampling clock offset δ_t, with N = 256, M = 10.

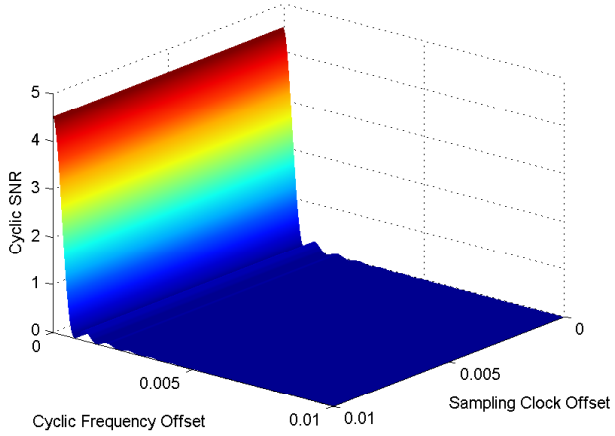

(b) Theoretical cyclic SNR at cyclic frequency $\alpha = 2f_c$ for a BPSK signal at SNR = -5 dB as a function of cyclic frequency offsets Δ_α and sampling clock offset δ_t, with N = 2560, M = 1.

Figure 3.3: Theoretical cyclic SNR at $\alpha_k = 2f_c$ versus sampling clock offset and cyclic frequency offset under the proposed and conventional test statistics with $f_c = 2.5$ MHz, $1/T = 1.25$ MHz, and $T_s = 1 \times 10^{-7}$s.

3.4 Optimizing the Detection Performance under both SCO and CFO

In this section, we find the optimum frame length and number of frames to be used for detection of cyclic features under both CFO and SCO in order to yield

the best average detection performance for signal $x_k[\cdot]$, given the distribution of the frequency and clock offsets. Note that the cyclic SNR is a function of the cyclic frequency α_k of interest. As a result, the best way to split the samples is dependent on α_k and has to be performed for each of the K signals in the wideband channel.

3.4.1 Optimum $(\hat{M}_{\alpha_k}, \hat{N}_{\alpha_k})$ Pair Selection

The cyclic SNR at a cyclic frequency α_k given a SCO δ_t and CFO Δ_α has been derived in (3.25). We let $P_\Delta(\cdot)$ and $P_\delta(\cdot)$ denote the pdf of the frequency offset and clock offset respectively. The average cyclic SNR at a given cyclic frequency α_k can therefore be computed as follows

$$\mathrm{SNR}_{\alpha_k} = \int_{-\infty}^{\infty}\int_{-\infty}^{\infty} \mathrm{SNR}_{\alpha_k|\delta_t,\Delta_\alpha} P_\Delta(\Delta_\alpha) P_\delta(\delta_t)\,\mathrm{d}\Delta_\alpha \mathrm{d}\delta_t. \tag{3.26}$$

Denoting $I_1(\alpha_k)$ and $I_2(\alpha_k)$ by

$$\begin{aligned} I_1(\alpha_k) &= \int_{-\infty}^{\infty} \frac{\sin^2\left(\pi\alpha_k N M T_s(1+\delta_t)\right)}{M^2\sin^2(\pi\alpha_k N T_s(1+\delta_t))} P_\delta(\delta_t)\,\mathrm{d}\delta_t \\ I_2(\alpha_k) &= \int_{-\infty}^{\infty}\int_{-\infty}^{\infty} \frac{\sin^2\left(\pi\alpha_k N \Delta_\alpha T_s(1+\delta_t)\right)}{N^2\sin^2\left(\pi\alpha_k \Delta_\alpha T_s(1+\delta_t)\right)} \times \\ &\quad \frac{\sin^2\left(\pi\alpha_k N M T_s(1+\delta_t)\right)}{M^2\sin^2\left(\pi\alpha_k N T_s(1+\delta_t)\right)} P_\Delta(\Delta_\alpha) P_\delta(\delta_t)\,\mathrm{d}\Delta_\alpha\mathrm{d}\delta_t, \end{aligned} \tag{3.27}$$

the average cyclic SNR at α_k can be written as

$$\mathrm{SNR}_{\alpha_k} = \frac{P_4[u_4 - u_2^2]}{2N\sigma_w^4} I_1(\alpha_k) + \frac{M|P_2|^2 u_2^2}{2N\sigma_w^4} I_2(\alpha_k). \tag{3.28}$$

In order to maximize the detection probability of the k^{th} signal subject to the sensing time constraint, we maximize SNR_{α_k}. Let the optimum frame length and the number of frames be denoted by $\hat{N}_{\alpha_k}$ and $\hat{M}_{\alpha_k}$ respectively, such that $\hat{N}_{\alpha_k}\hat{M}_{\alpha_k} \leq N_T$ which adds a constraint to the sensing time. Note that an addi-

tional constraint should be added with respect to the frame length $\hat{N}_{\alpha_k}$ since a minimum number of samples N_{min} is required to ensure that the test statistic covers a few information symbols within one frame. From (3.28), the maximization problem can be written as

$$(\hat{N}_{\alpha_k}, \hat{M}_{\alpha_k}) = \arg\max_{N,M} \frac{P_4[u_4 - u_2^2]}{2N\sigma_w^4} I_1(\alpha_k) + \frac{M|P_2|^2 u_2^2}{2N\sigma_w^4} I_2(\alpha_k)$$
$$\text{such that} \quad NM \leq N_T, \text{and } N \geq N_{min} \tag{3.29}$$

which shows that the best method of splitting the incoming samples is independent of the noise variance. As a result, this optimization can be performed offline given the distribution of the two considered impairments, and the optimum split of samples for cyclic frequency α_k will hold for all SNR levels as the best split is independent of the noise variance. The optimization problem has therefore been simplified to a two dimensional integer optimization problem which could be efficiently solved numerically as it only requires the knowledge of the statistical distribution of the considered impairments.

3.4.2 Theoretical Average Detection Performance for a Given Distribution of CFO and SCO

So far, we have used the cyclic SNR as a metric to optimize the detection performance. In this section, we quantify the average detection performance under a given average cyclic SNR and any (M, N) pair including the optimum $(\hat{M}_{\alpha_k}, \hat{N}_{\alpha_k})$ pair. We make use of the Central Limit Theorem (CLT) in order to approximate the distribution of $\hat{R}_r^{\alpha_k}(0)$ as a Gaussian distribution [DNL10]. Further, the analysis below is based on the non-conjugate multi-frame test statistic, assuming that the detection is based on the cyclic feature at $\alpha = 2f_c$. Given that the CAC has non-zero mean under $\mathcal{H}_0$, the test statistic $|\hat{R}_x^{\alpha_k}(0)|$ will be Ricean distributed.

The mean and variance of the test statistic can be obtained as

$$\mu_0 \triangleq \mathbb{E}[\hat{R}_w^{\alpha_k}(0)] = \frac{\sigma_w^2 \sin(\pi\alpha_k N T_s)}{N \sin(\pi\alpha_k T_s)},$$
$$\sigma_0^2 \triangleq \mathbb{E}[|\hat{R}_w^{\alpha_k}(0)|^2] - \mu_0^2 = \frac{2\sigma_w^4}{MN} - \frac{\sigma_w^4}{N^2}\frac{\sin^2(\pi\alpha_k N T_s)}{\sin^2(\pi\alpha_k T_s)}. \tag{3.30}$$

Therefore, the probability of false alarm $P_{fa}(\cdot)$ can be evaluated as

$$P_{fa}(\gamma) = Q_1\left(\frac{\mu_0}{\sqrt{\sigma_0^2/2}}, \frac{\gamma}{\sqrt{\sigma_0^2/2}}\right), \tag{3.31}$$

where γ is the threshold chosen to yield a constant false alarm rate (CFAR), and $Q_1(\cdot,\cdot)$ is the Marcum Q function. Further, since the mean of the cyclic feature is a function of both CFO and SCO, it can be easily shown in a similar fashion as Eq. (3.24) was derived that the average theoretical mean of the non-conjugate CAC under noiseless conditions is given as

$$\mu_s \triangleq \mathbb{E}[|\hat{R}_s^{\alpha_k}(0)|] = \frac{u_2 P_2^{'}}{N} U, \tag{3.32}$$

where $P_2^{'}$ is defined as in (3.19) and is computed for the cyclic frequency α_k of interest, and where

$$U = \int_{-\infty}^{\infty}\int_{-\infty}^{\infty} \frac{\sin(\pi\alpha_k N \Delta_\alpha T_s(1+\delta_t))}{N \sin\left(\pi\alpha_k \Delta_\alpha T_s(1+\delta_t)\right)} \times$$
$$\frac{\sin\left(\pi\alpha_k N M T_s(1+\delta_t)\right)}{M \sin\left(\pi\alpha_k N T_s(1+\delta_t)\right)} P_\delta(\delta_t) P_\Delta(\Delta_\alpha)\, \mathrm{d}\Delta_\alpha \mathrm{d}\delta_t. \tag{3.33}$$

The parameters of the Ricean distribution are given by

$$\mu_1 = \sqrt{\mu_s^2 + \mu_n^2} = \sqrt{\frac{\sigma_w^2 \sin^2(\pi\alpha_k N T_s)}{N^2 \sin^2(\pi\alpha_k T_s)} + \frac{u_2^2 P_2^{'2} U^2}{N^2}}, \tag{3.34}$$

$$\sigma_1^2 = 0.5\mathrm{Var}\left(|\hat{R}_s^{\alpha_k}(0)|\right) + 0.5\mathrm{Var}\left(|\hat{R}_w^{\alpha_k}(0)|\right)$$
$$= \frac{P_4(u_4 - u_2^2)}{2MN^2} I_1(\alpha_k) + \frac{|P_2^{'}|^2 u_2^2}{2N^2} I_2(\alpha_k) + \frac{\sigma_w^4}{MN} - \frac{\sigma_w^4}{2N^2}\frac{\sin^2(\pi\alpha_k N T_s)}{\sin^2(\pi\alpha_k T_s)}. \tag{3.35}$$

Finally, the detection probability can be expressed as

$$P_d(\gamma) = Q_1\left(\frac{\mu_1}{\sqrt{\sigma_1^2/2}}, \frac{\gamma}{\sqrt{\sigma_1^2/2}}\right), \tag{3.36}$$

where $Q_1(\cdot,\cdot)$ is again the Marcum Q function.

3.5 Numerical Results

This section is aimed at showing the performance gains achieved by the proposed multi-frame detector in the presence of the considered impairments. The spectrum being monitored is 10 MHz wide. In Section 3.5.1, the derived moments needed for the cyclic SNR expression are verified under a given realization of the CFO and the SCO. In section 3.5.2, the average cyclic SNR is optimized under a fixed sensing time, resulting in the optimum frame length and number of frames given a certain realization of the cyclic frequency and sampling clock offsets. Given the average cyclic SNR, the theoretical average probability of detection and false alarm are then compared against numerical simulations. Finally, we show in Section 3.5.3 the gains in cyclic SNR that can be achieved using the proposed multi-frame statistic.

3.5.1 Verification of Derived Statistics under a Given Realization of the Impairments

In the first section of the numerical results, we verify the derived statistics of the multi-frame CAC under receiver impairments for fixed CFO and SCO values. First, Fig. 3.4 verifies the derived statistics of the conjugate and non-conjugate CAC under $\mathcal{H}_0$ obtained in (3.12) and (3.13) for two different values of σ_w^2 at $N = 256$, for varying frames M. As expected, the second moment of the CAC under $\mathcal{H}_0$ decreases as the number of frames M increases, which helps in separating the cyclic feature of interest from the noise. Note that with respect to noise

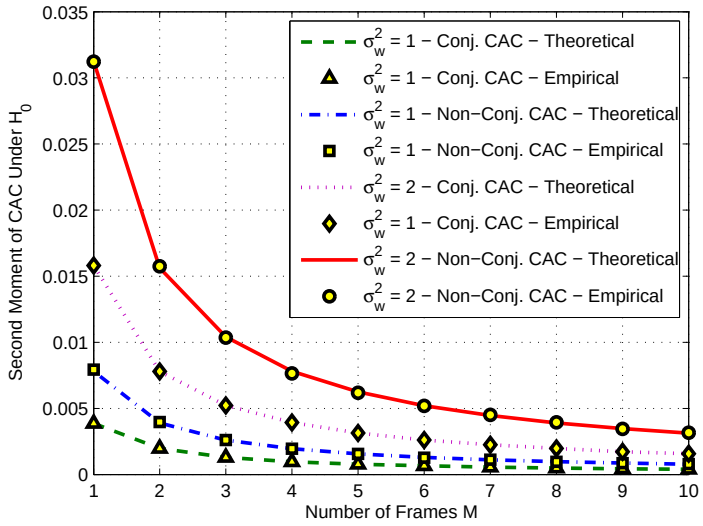

Figure 3.4: Verification of the theoretical derivation of the CAC second moment under $\mathcal{H}_0$ under $\sigma_w^2 = 1$ and $\sigma_w^2 = 2$.

suppression, different choices of M and N under a fixed sensing time result in the same test statistic second moment under $\mathcal{H}_0$, and therefore the CAC distribution under $\mathcal{H}_0$ is only a function of the sensing time, and does not depend on the split between N and M.

Similarly, Fig. 3.5 verifies the theoretical derivations obtained in (3.24) where both the CFO and SCO have been fixed to $\Delta_\alpha = \delta_t = 1 \times 10^{-4}$ for $M = 10$ and $M = 20$, where the number of samples per frame N has been varied for a fixed sampling period T_s. As expected, increasing the number of samples per frame results in the smearing of the cyclic feature of interest because of the compounded effects of non-zero SCO and non-zero CFO. Now that the theoretical derivations have been verified under a fixed realization of the frequency and clock offsets, the optimum $(\hat{M}_{\alpha_k}, \hat{N}_{\alpha_k})$ can be chosen to achieve the maximum achievable average cyclic SNR given in (3.28).

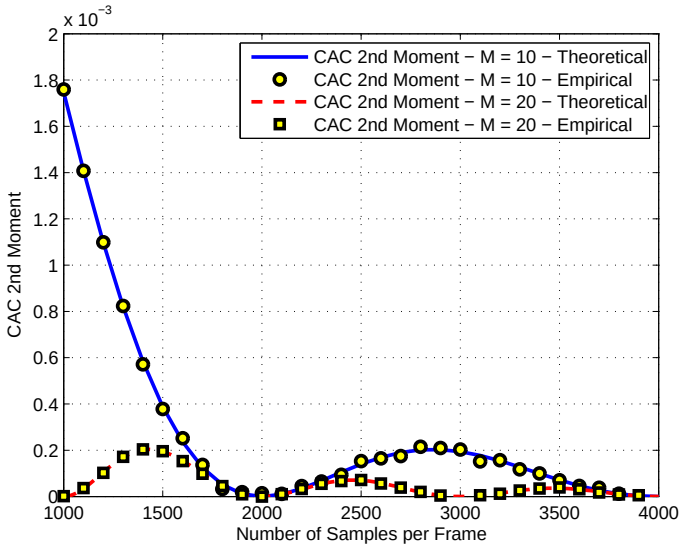

Figure 3.5: CAC second moment under noiseless conditions of a BPSK signal at $\alpha = 2f_c$ versus N, for $M = 10, 20$ for a fixed $\Delta_\alpha = \delta_t = 1 \times 10^{-4}$ and $f_c = 2.5$ MHz, $1/T = 1.25$ MHz, and $T_s = 1 \times 10^{-7}$s.

3.5.2 Optimum (M,N) Pair Selection

In the numerical results that follow, we have used zero-mean Gaussian distribution to model both the cyclic frequency and sampling clock offsets as assumed in [One09, LKS09, BCC07], with variances σ^2_{sco} and σ^2_{cfo} respectively. More formally,

$$P_\Delta(\Delta_\alpha) = \left(2\pi\sigma^2_{cfo}\right)^{-\frac{1}{2}} e^{-0.5\left(\frac{\Delta_\alpha}{\sigma_{cfo}}\right)^2}, \tag{3.37}$$

$$P_\delta(\delta_t) = \left(2\pi\sigma^2_{sco}\right)^{-\frac{1}{2}} e^{-0.5\left(\frac{\delta_t}{\sigma_{sco}}\right)^2}. \tag{3.38}$$

Note that a similar analysis can be conducted using any frequency and clock offset distributions.

In this section, we show the average CAC second moment of a BPSK signal at $\alpha = 2f_c$ with unit average energy symbols for a fixed sensing time, $NM = 5000$ samples. In this setup, the distributions of the frequency and clock offsets are such that $\sigma_{sco}/\sigma_{cfo} = 0.2$, where $\sigma_{cfo} = 1 \times 10^{-4}$. The average second moment of the non-conjugate multi-frame statistic under noiseless conditions is computed

at every combination (M, N), and its value is compared in Fig. 3.6(a) to the theoretically derived one, given by

$$\frac{P_4}{MN^2}[u_4 - u_2^2]I_1(\alpha_k) + \frac{|P_2'|^2 u_2^2}{N^2} I_2(\alpha_k). \tag{3.39}$$

obtained by averaging (3.24) over the distribution of the CFO Δ_α and the SCO δ_t. Note that theoretical results and simulations are matched, which validates our analysis. Interestingly, it can be observed that increasing the number of frames M does not result in a clear trend with respect to the average CAC second moment. In fact, $M = 8$ results in a much worse average CAC moment than $M = 7$. The reason for this behavior is because at $M = 6, 8, 9$, the resulting number of samples per frame are such that the degradation due to the multi-frame processing totally degrades the feature to be detected, therefore resulting in an average second-order moment of the signal's feature that is close to zero. The optimum method for splitting the acquired samples to achieve the best average detection performance is verified in Fig. 3.6(b) under the same frequency and clock offsets conditions as mentioned above, with $\sigma_w^2 = 1$. As expected, we can see that the way by which the samples are split is crucial to the detector's performance under the two considered impairments, and the best average detection performance is attained using $M = 12$. Note that this optimization can be performed offline since it only depends on the distribution of the receiver impairments, and therefore its computational complexity, although minimal, is not of a great importance.

Next, the theoretical average detection performance of the proposed detector under a fixed sensing time of $NM = 5000$ samples is compared against the empirically obtained detection performance for different SNR values, where $\sigma_{sco}/\sigma_{cfo} = 0.2$, and where $\sigma_{cfo} = 1 \times 10^{-4}$. The best splitting method is the same as the one determined in Fig. 3.6(a) which results in splitting the acquired samples into $M = 12$ frames. Fig. 3.7 verifies the average theoretical probability of false alarm and detection derived in (3.31) and (3.36) at different SNR val-

ues. Further, we show by numerical simulations the effect of varying the SCO δ_t on a per sample basis on the average detection performance. Interestingly, a time varying SCO within the sensing window has a minimal effect on the average detection performance.

3.5.3 Cyclic SNR Gain Achieved by the Proposed Method Compared to the Conventional Detector

In this section, we compare the average cyclic SNR of the proposed detector with the average cyclic SNR of the conventional detector ($M = 1$) in order to show the achievable gains in splitting the acquired samples into frames. The numerical results given in Fig. 3.8 depict the average cyclic SNR at $\alpha = 2f_c$ of a BPSK signal with average unit energy symbols, under a noise variance of $\sigma_w^2 = 1$ as a function of the sensing time. The optimization (3.29) is performed for each sensing time which corresponds to a fixed total number of samples, and the best splitting method which results in the maximum cyclic SNR is chosen according to (3.29). Note that the optimization and the results do not depend on the noise variance σ_w^2 as was pointed out earlier. Fig. 3.8 depicts the gains that one could achieve given the distribution of the receiver impairments at hand, where the distribution of the frequency offset has been kept constant, with $\sigma_{cfo} = 4 \times 10^{-4}$ which results from imperfect knowledge of the cyclic frequencies. Two extreme cases are compared in this figure. The average cyclic SNR using the conventional detector based on the single-frame CAC is given, and is compared to the optimum case using the multi-frame statistic when $e = 0$ which can only occur when no sampling clock offset δ_t is present at the receiver and resampling is performed such as $N\alpha T_s$ is an integer for every frame length considered. We consider the latter case to be the upper bound on the average detection performance since we can reduce the effects of CFO by reducing the frame size, without incurring any penalty due to the SCO as a result of the multi-frame statistic. The rest of the curves show the average cyclic SNR gains that could be achieved without resampling for various

clock offset distributions, starting with $\sigma_{sco} = \sigma_{cfo}$, for which no gain is achieved in splitting the incoming samples. As the ratio of $\sigma_{sco}/\sigma_{cfo}$ decreases, the gains of the proposed method become more pronounced, and tend to the upper bound without any SCO where the maximum achievable gain is reached. Intuitively, the clock and frequency offsets introduce similar decaying terms in the cyclic SNR expression. When the clock offset is less dominant than the frequency offset, i.e., $\sigma_{sco} < \sigma_{cfo}$, which is common case in practice, then splitting the samples using the proposed test statistic would result in performance gain in the average sense.

It is worth noting that the upper bound on the average detection performance is when the frame length is $N = N_{min}$ which minimizes the degradation due to the CFO Δ_α, and where resampling is performed so that $e = 0$. Such a detection is equivalent to performing the detection using the conventional CAC under no impairments. As a result, depending on the relationship between σ_{sco} and σ_{cfo}, the average detection performance of the proposed detector can meet that of conventional detectors under no impairments without the need for resampling and incurring any additional computational complexity.

3.6 Summary

In this chapter, we have shown that conventional cyclostationary detectors are not robust to receiver impairments, and signal detection in low SNR regimes becomes challenging under the resulting cyclic frequency offsets. We have proposed a new multi-frame cyclostationary detector, and have derived the average cyclic SNR that can be optimized to maximize the average detection performance under frequency and sampling clock offsets given their statistical distributions. We have developed an optimization tool to theoretically analyze and quantify the achievable gains that could be achieved using the proposed method. Further, we have derived the theoretical average detection and false alarm probabilities of the proposed detector under the two considered impairments. The main contributions

of this work lie in understanding the impact of frequency and clock offsets on cyclostationary detectors and in developing a tool to verify when detection can be improved by splitting the acquired samples into frames and using our proposed detector. Given the distribution of the frequency and clock offsets at the sensing radio, this optimization tool can be used as a design guideline for wideband spectrum sensing devices that are able to simultaneously sense multiple signals without the increased complexity due to resampling the received signal on a per-signal basis.

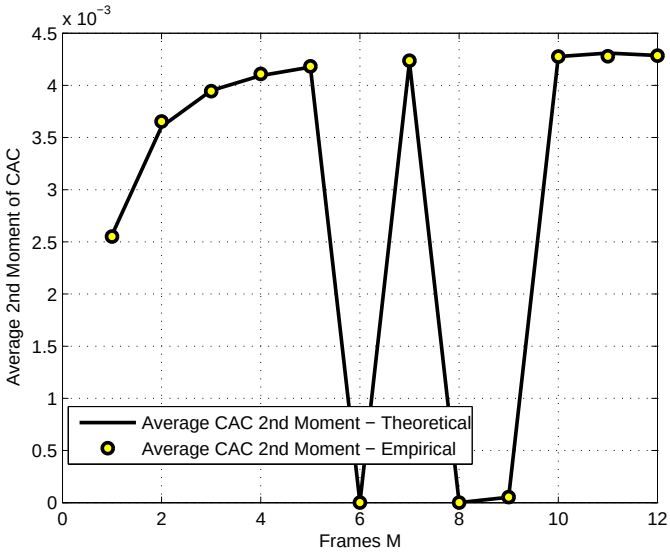

(a) Average test statistic second moment versus number of frames for a fixed sensing time under noiseless conditions.

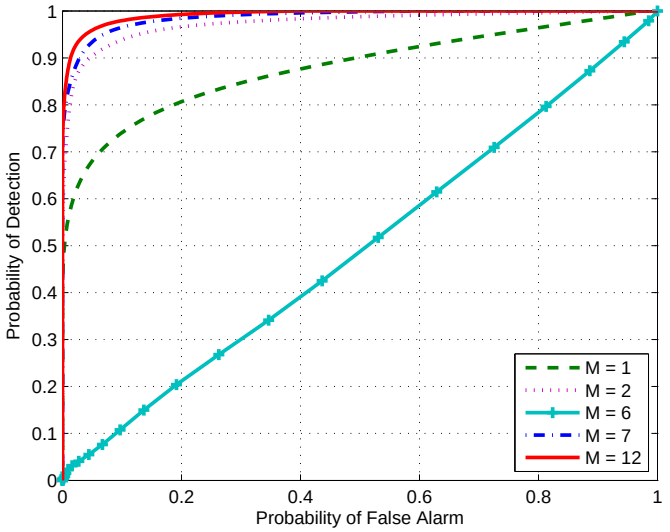

(b) Average detection performance for a fixed sensing time with varying number of frames at SNR of -5 dB.

Figure 3.6: Average cyclic SNR for BPSK signal using single cycle detector at $\alpha = 2f_c$ and its resulting empirical detection performance with varying number of frames M under a fixed sensing time with $NM = 5000$ samples, and $\sigma_{sco}/\sigma_{cfo} = 0.2$ with $\sigma_{cfo} = 2 \times 10^{-4}$, $f_c = 2.5$ MHz, $1/T = 1.25$ MHz, and $T_s = 1 \times 10^{-7}$s.

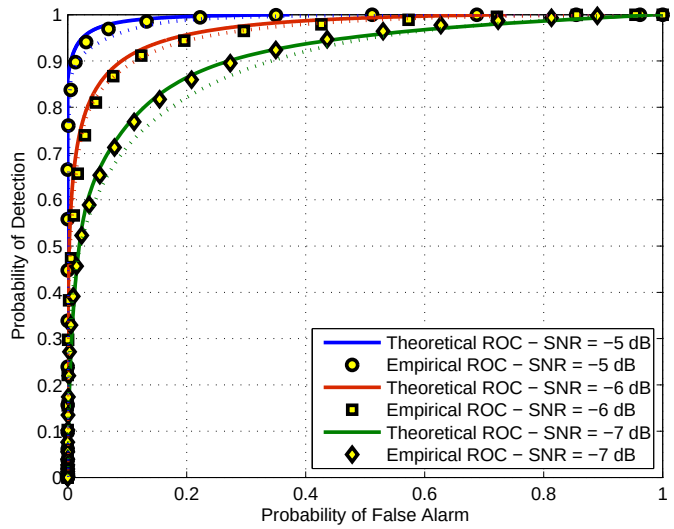

Figure 3.7: Theoretical and empirical average probability of detection vs. probability of false alarm for single cycle detector on BPSK signal with a total number of samples $NM = 5000$ samples, cyclic frequency $\alpha = 2f_c$ under random frequency and clock offset distributions with $\sigma_{sco}/\sigma_{cfo} = 0.2$ with $\sigma_{cfo} = 2 \times 10^{-4}$ using the optimum split $M = 12$ frames obtained from Fig. 6. Signal parameters are given by $f_c = 2.5$ MHz, $1/T = 1.25$ MHz, and $T_s = 1 \times 10^{-7}$s. Simulated ROC curves with varying SCO δ_t on a per sample basis are shown in dashed lines.

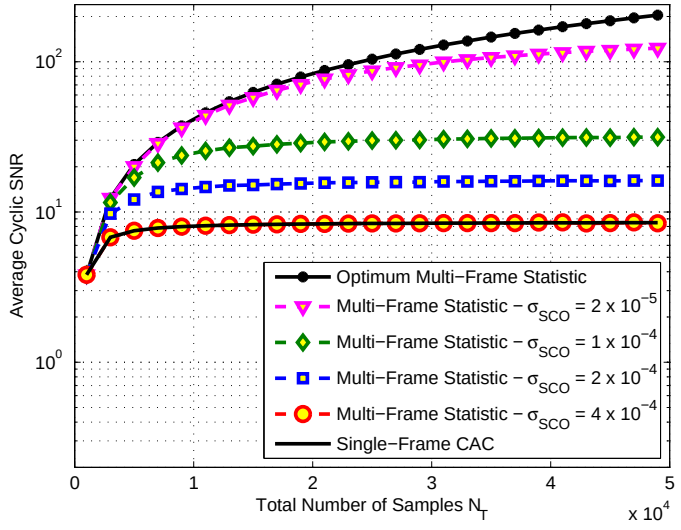

Figure 3.8: Average cyclic SNR of a BPSK at cyclic frequency $\alpha = 2f_c$, under $\sigma_{cfo} = 4 \times 10^{-4}$ as a function of the total number of samples for various σ_{sco} values, with $f_c = 2.5$ MHz, $1/T = 1.25$ MHz, and $T_s = 1 \times 10^{-7}$s.

CHAPTER 4

Energy-Efficient Processor for Blind Signal Classification in Cognitive Radio Networks

Blind modulation classification is particularly challenging from the energy consumption point of view. In fact, as cycostationary-based classification requires detecting the present cyclic features of the received signal, estimating both the symbol rate and carrier frequency is therefore necessary. We present a reconfigurable processor architecture that can blindly classify any linearly modulated signal (M-QAM, M-PSK, M-ASK, and GMSK) in addition to multi-carrier signals and spread spectrum signals. The main contribution of this work is to analyze the complexity tradeoffs among different dependent signal processing kernels in order to minimize the total processing time and energy.

In this chapter, we propose an implementation with high functional diversity and energy/area efficiency. By jointly considering the algorithm and architecture layers, we first select computationally efficient parameter estimation and modulation classification algorithms. We then exploit the functional similarities between algorithms to build a processing architecture that maximizes hardware utilization. In addition, we carefully analyze the processing strategy of the processor in order to minimize the overall consumed energy.

This chapter is organized as follows. We present in Section 4.1 our design objectives for the blind modulation classifier. Section 4.2 presents the overall receiver architecture and the design challenges in blind classification. Section 4.3 describes the low-complexity signal processing modules implemented in the pro-

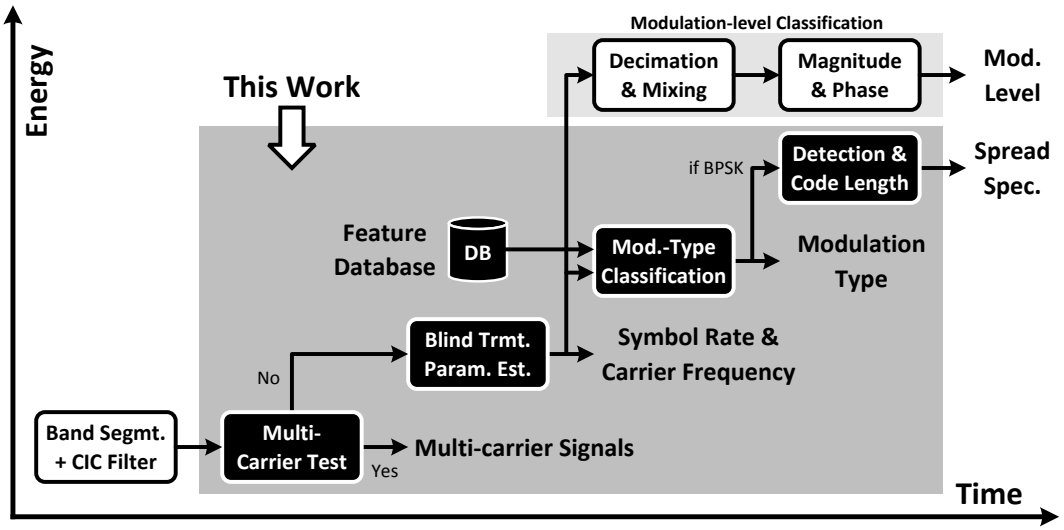

Figure 4.1: Top-level block diagram with energy-time breakdown of the processing kernels of the proposed blind modulation classifier.

cessor. In Section 4.4, we present the proposed energy optimization methodology, in which we analyze the tradeoffs among dependent blocks of the architecture. Some numerical results are presented in Section 4.5. Finally, Section 4.6 summarizes the chapter.

4.1 Design Objectives

The design specifications of the proposed classifier are summarized in Table 4.1. We consider a minimum SNR of 10 dB, which is reasonable for classification of interferers in multi-user detection and blind signal demodulation applications. We note that we do not estimate the received SNR in the proposed processor. Instead, we guarantee that when the SNR exceeds 10 dB, the proposed processor will correctly classify the received signal with a minimum probability of 95%. The frequency resolution is set to 12.5 KHz in order to allow a fine spectral resolution to detect narrowband interferers. The classifier should identify multi-carrier, spread spectrum and linearly modulated signals correctly with a probability of 95%. Within the linearly modulated signals, the classifier should also distinguish

Table 4.1: Design Specifications of the Proposed Modulation Classifier.

Variables	Specifications
Modulation Types	M-QAM, M-PSK, M-ASK, GMSK, OFDM, DSSS
Probability of Correct Classification	≥ 0.95
Energy Budget	15 μJ
Proc. Time Budget	2 ms
Channel Bandwidth	500 MHz
Frequency Resolution	12.5 KHz
Signal Bandwidth	$\leq$ 500 MHz
Minimum SNR	10 dB

the modulation types given in Table 4.1. The proposed processor needs to meet an energy constraint of 15 μJ and a processing time of 2 ms.

4.2 Design Considerations

This section describes the overall receiver architecture and shows how the proposed modulation classification processor fits as part of a wideband receiver chain. We then describe the challenges in blind modulation classification and give an intuitive explanation behind the tradeoffs among different blocks of the proposed processor.

4.2.1 System Model

We illustrate in Fig. 4.1 the top-level block diagram of the blind signal classifier. Before classification, the processing flow follows the flow presented in Fig. 2.3. At the beginning, the RF front-end filters and downconverts a 500 MHz spectrum to baseband. The signal is then sampled and digitized for baseband processing. The digital baseband part starts with a sensing engine, referred to as the band segmentation, that detects the presence of one or more signals in the wideband channel in the presence of Additive White Gaussian Noise (AWGN) [YSR11]. The detection is based on energy detection which estimates the spectrum of the

received signal. The sensing time and threshold for detection are adjusted to meet the desired probability of detection and false alarm. The supported signals that can be classified could be of any modulation type given in Table 4.1 with bandwidth greater than 12.5 KHz, and could be located at any carrier frequency. Since this chapter deals with the design of the signal classification processor, we assume that the signal has already been detected. Identifying the presence of a signal during band segmentation inherently results in coarse estimates of the signal's carrier frequency and symbol rate. Using the coarse transmit parameters, the detected signal is down-converted and filtered using a reconfigurable Cascade-Integrator-Comb (CIC) filter [Hog81]. The output of the CIC filter is fed to the modulation classifier to identify the modulation type of the signal. In the event of detecting multiple signals in the wideband channel, each signal is downconverted and processed by the CIC filter sequentially.

This work focuses on the design of an energy-efficient modulation classifier, which detects the types of signals using the optimized tree-based approach shown in Fig. 4.2. The proposed modulation type classifier is based on second-order cyclostationary properties of the received signal and therefore does not distinguish among different levels of a given modulation type. However, once the modulation type is found, the signal can then be fed to a modulation-level classifier. In our earlier work, we developed a low-complexity modulation-level classifier [URP11] based on the distribution distance test that chooses the modulation level whose cumulative distribution function (CDF) is closest the received symbols CDFs. The performance of the proposed modulation-level classifier has been compared in hardware experiments [URC11] against the well-known cumulants classifier [SS00]. Although the modulation-level classifier can be implemented as part of the proposed processor, it is not considered in this work due to its very low computational complexity and consumed energy.

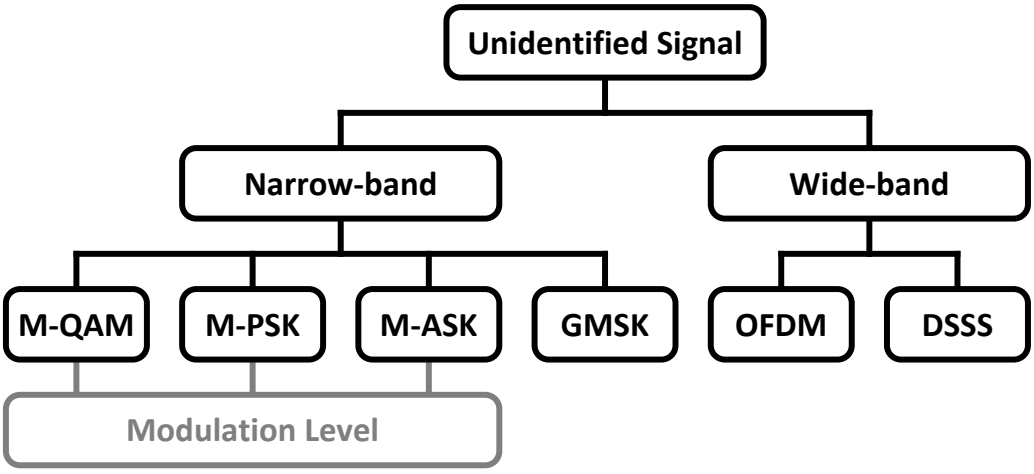

Figure 4.2: Signal classification tree showing the possible modulation classes recognized by the proposed processor.

4.2.2 Design Challenges

The objective of the proposed classifier is to minimize its consumed energy while achieving the required probability of correct classification. The energy minimization is achieved by 1) selecting and developing computationally efficient algorithms, and 2) by minimizing the total classification time while meeting the classification accuracy of 95%. Although existing maximum-likelihood-based algorithms [WM00a, SK11] can meet the classification requirement, their computational complexity results in power and/or delay requirements that cannot be tolerated in real-time operating radios. In addition, blind modulation classifiers require the estimation of the signal's transmit parameters, adding to the overall complexity of the receiver. Therefore, our objectives in meeting the specifications are twofold: 1) developing low-complexity algorithms that meet the classification probability, 2) minimize the processing times of all the blocks in order to satisfy the energy budget.

As a result of the 12.5 KHz resolution of the band segmentation, the coarse estimates of the symbol rate and carrier frequency obtained from the band segmentation have estimation errors on the orders of thousands of parts per million.

For instance, as a result of the transmit filter roll-off, the coarse symbol rate estimate of a 3 MHz signal can vary between 3 and 3.5 MHz, yielding an estimation error of 1.6×10^5 ppms. As was shown in Chapter 3, the features used for modulation-type classification degrade under large estimation errors of the cyclic frequencies. As a result, classification probability cannot be met under such large offsets. Therefore, coarse estimates cannot be used directly for detection of cyclic features, and hence fine estimates of the transmit parameters are needed. To address this issue, our architecture includes symbol rate and carrier frequency estimation blocks referred to as the *pre-processors*. We show that there exists an inherent tradeoff between estimation accuracies of the transmit parameters and the classification accuracy that can be achieved, which will be analyzed in Section 4.4.

4.3 Low-Complexity Blind Classification Algorithms

In this section, we present the proposed algorithmic hierarchical classification tree. The design hierarchy is based on both the level of *a priori* information that a block requires and its computational complexity. In particular, the blocks that do not require *a priori* information about the signal being classified are processed first. For instance, the multi-carrier classifier employs a totally blind low-complexity algorithm, and therefore can be performed first. This design methodology dictates the order in which the classification algorithms are performed as shown in Fig. 4.1. In the remainder of this section, we describe each of the blocks of our processor, and specify what design variables need to be optimized in order to meet the given accuracy and energy requirements.

Multi-Carrier (MC) OFDM (Orthogonal Frequency Division Multiplexing) and Single Carrier (SC) signal classification can be performed using a Gaussianity test using the fourth-order cumulant C_{42} [SLB08]. The property of C_{42} is that, it tends to zero if the input samples are approaching Gaussian distribution.

The C_{42} statistic of an OFDM signal, as a result, is close to zero since the OFDM is a mixture of a large number of sub-carrier waveforms. With respect to spread spectrum classification, one can distinguish between BPSK and direct sequence spread spectrum (DSSS) signals based on the variance of the signal's autocorrelation at a given lag τ [BBB01]. The focus of this chapter is on the modulation type estimation. More information about MC/SC and DSSS classification can be found in [RYU13].

4.3.1 Center Frequency and Symbol Rate Preprocessor

When the signal is classified as an SC signal, its transmit parameters need to be estimated first. Both the *pre-processors* and the modulation-type classifier for SC signals rely on the Cyclic Auto-Correlation (CAC) function to detect their cyclostationary features. Under a finite number of samples N, the conjugate and the non-conjugate CACs can be computed respectively as follows:

$$\tilde{R}^{\alpha}_{x^*}(\nu) = \frac{1}{N}\sum_{n=0}^{N-1} x[n]x^*[n-\nu]e^{-j2\pi\alpha n T_s}, \tag{4.1}$$

$$\tilde{R}^{\alpha}_{x}(\nu) = \frac{1}{N}\sum_{n=0}^{N-1} x[n]x[n-\nu]e^{-j2\pi\alpha n T_s}, \tag{4.2}$$

where ν is the lag variable, T_s is the sampling period, and α is the cyclic frequency to be detected. Note that the conjugate CAC is used to detect cyclic frequencies close to baseband, whereas the non-conjugate CAC is used to detect the cyclostationary features at cyclic frequency α related to the carrier frequency. Different modulation classes can be differentiated via the cyclostationarity test because their CACs possess cyclic peaks at different locations of cyclic frequencies α, which is a function of the symbol rate $(1/T)$ and the carrier frequency (f_c).

However, in blind classification scenarios, the estimated cyclic frequencies might not be equal to true cyclic frequencies. It was shown in 3 that computing

the CAC at $\hat{\alpha} = (1 + \Delta_\alpha)\alpha$, where α is the true cyclic frequency and Δ_α is the cyclic frequency offset (CFO), results in performance degradation in terms of the classification accuracy. Therefore, under a non-zero CFO Δ_α, increasing the number of samples (N) does not improve the detection accuracy but instead degrades the cyclostationary feature. This in turn motivates the need for accurate estimates of the transmit parameters in order to minimize the CFO Δ_α and improve the performance of the modulation-type classification.

With respect to the symbol rate estimation, we note that all SC modulation classes considered in this work exhibit a cyclostationary feature at cyclic frequency $\alpha = 1/T$. Therefore, detecting the presence of this cyclostationary feature would inherently estimate the symbol rate of the signal. The coarse estimate of the symbol rate from the band segmentation can be used to set the search window $\mathcal{W}_T$, within which the cyclic peak at the symbol rate will be located. The detection of the cyclostationary feature at $1/T$ is therefore obtained by solving the following optimization problem:

$$\max_{\alpha_i \in \mathcal{W}_T} \left| \sum_{n=0}^{N_T-1} |x[n]|^2 e^{-j2\pi\alpha_i n T_s} \right|, \tag{4.3}$$

where N_T is the number of samples per CAC computation used to estimate the signal's symbol rate.

Given that not all classes have the cyclostationary feature related to their carrier frequency, the CACs given in (4.2) cannot be directly used to estimate the signal's carrier frequency. Estimation of the carrier frequency of the incoming signal can be performed by detecting the cyclic feature at $\alpha = 4f_c$ after squaring the incoming samples [MM98,CS04]. We denote the search window by $\mathcal{W}_f$ within which the cyclic peak at $4f_c$ occurs. The estimation is therefore obtained by

solving the following optimization problem:

$$\max_{\alpha_i \in \mathcal{W}_f} \left| \sum_{n=0}^{N_f-1} x[n]^4 e^{-j2\pi\alpha_i n T_s} \right|, \tag{4.4}$$

where N_f is the total number of samples per CAC computation used to estimate the signal's carrier frequency. Note that by increasing the number of samples over which the CAC is computed, the noise is suppressed and the features of interest become prominent. As a result, both N_T and N_f are a function of the SNR of the received signal.

Solving the optimizations given in (4.3) and (4.4) requires infinite computational complexity. As a result, the search space for the maximum cyclic feature has to be discretized. We denote by Δ_{α_T} and Δ_{α_f} the resolutions for the symbol rate and carrier frequency estimators. As a result, there are two degrees of freedom in the design of each of the algorithms: 1) the step size Δ_{α_T} and Δ_{α_f} within the window $\mathcal{W}_T$ and $\mathcal{W}_f$ respectively, and 2) the number of samples N_T and N_f required for the computation of every CAC at the cyclic frequency α_i of interest. The symbol rate and the carrier frequency estimation algorithms cannot yield estimation accuracies smaller than their respective step size Δ_{α_T} and Δ_{α_f}.

Also, the number of CAC computations required in (4.3) and (4.4) is equal to the cardinality of the discretized search windows $S_T = \lceil \mathcal{W}_T/\Delta_{\alpha_T} \rceil$ and $S_f = \lceil \mathcal{W}_f/\Delta_{\alpha_f} \rceil$ respectively. Given that both estimators use the CAC signal processing kernel, their consumed energy per sample is therefore the same, with the exception of the energy consumed for squaring the samples which is negligible compared to the CAC energy consumption. As a result, the total consumed energy of the *pre-processors* is proportional to $(S_T N_T + S_f N_f)T_s$. The choice of the design parameters (Δ_{α_T}, Δ_{α_f}, N_T, N_f) and their relationship to the required classification accuracy is explained in Section 4.4.

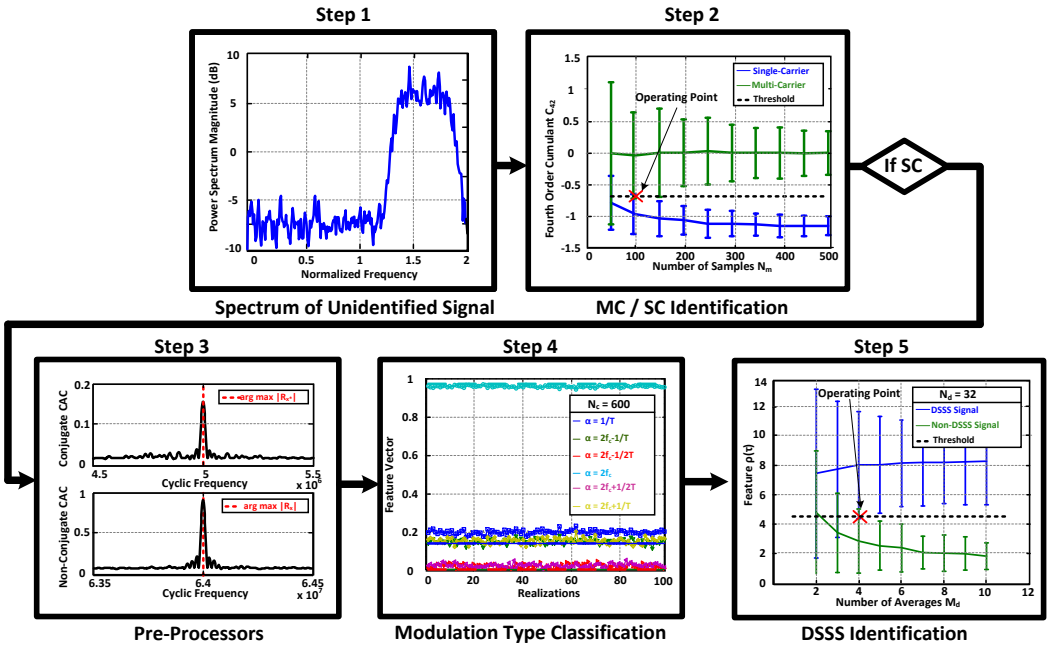

Figure 4.3: Classification example of a 5 MHz DSSS signal with underlying BPSK modulation scheme.

4.3.2 Modulation-Type Classifier

After estimating the signal parameters, the proposed modulation-type classifier computes the CAC at cyclic frequencies within the union of possible cyclostationary features in Table 2.1, resulting in a a six-dimensional feature vector [RC11b] given by

$$\mathbf{F} = \Big[|\tilde{R}_{x^*}^{1/T}(0)|, |\tilde{R}_x^{2f_c-1/T}(0)|, |\tilde{R}_x^{2f_c-1/2T}(0)|, \\ |\tilde{R}_x^{2f_c}(0)|, |\tilde{R}_x^{2f_c+1/2T}(0)|, |\tilde{R}_x^{2f_c+1/T}(0)| \Big] . \tag{4.5}$$

Because each element in the feature vector $\mathbf{F}$ is proportional to the received signal power, we normalize the feature vector to unit power, and compare this normalized feature vector $\bar{\mathbf{F}}$ to asymptotic normalized feature vectors $\bar{\mathbf{V}}_i$, $i \in [1, 2, 3]$, for each of the classes considered. For instance, the normalized asymptotic feature vector for signals belonging to Class 1 is $\bar{\mathbf{V}}_1 = [1, 0, 0, 0, 0, 0]$ as only one

cyclic feature is present at the signal's symbol rate.

The resulting normalized feature vector is compared to each feature vector $\bar{\mathbf{V}}_i$, and the classifier picks the modulation class $\hat{C}$ whose feature vector is closest to one of the received signal in the least square sense [RC11b], namely

$$\hat{C} = \arg \min_{i \in [1,2,3]} ||\bar{\mathbf{F}} - \bar{\mathbf{V}}_i||^2. \tag{4.6}$$

In contrast to the *pre-processors*, the only degree of freedom in the design of the modulation type classifier is the number of samples N_c required to compute each of the six CACs that form the feature vector. Given SNR of the received signal and the estimation accuracies of the *pre-processors*, N_c is chosen accordingly to meet the desired classification probability. As a result of the six CACs required for classification, the processing time for modulation-type estimation is equal to $6N_cT_s$. The six CACs are computed sequentially to enable high degree of hardware reuse without violating the processing time budget and compromising the total energy consumption.

We would like to note that although the cyclic features that the considered modulation types exhibit are known and can be used for parameter estimation, an energy efficient method to estimate the symbol rate and carrier frequency has not been proposed before. Further, the authors are not aware of any work that ties the symbol rate and carrier frequency accuracies to the modulation classification probability. As will be shown in Section 4.5, the *pre-processors* consume most of the processor's energy, and therefore a careful selection of the step sizes for $\mathcal{W}_T$ and $\mathcal{W}_f$ is necessary to achieve an energy efficient solution.

4.3.3 Example of Classification Flow

We consider the classification of a DSSS signal with an underlying BPSK modulation scheme that is spread with a code of length 8. The DSSS signal has a symbol

rate of 5 MHz, and is centered at 125 MHz at SNR of 10 dB. After detecting the presence of the signal in the band segmentation, the CIC filter downconverts the signal to a center frequency of 16 MHz and decimates it resulting in 4 samples per symbol. Fig. 4.3 shows the output of each of the algorithms discussed in this section. In the first block of the classification tree, the C_{42} cumulant is computed and compared against a threshold. We show that setting $N_m = 90$ samples is sufficient to separate SC and MC classes with a probability of 95%. In this case, the DSSS signal being a SC signal will be classified as SC, and its transmit parameters will be computed next using (4.3) and (4.4). Using $N_T = N_f = 400$ samples, the *pre-processors* estimate the symbol rate and carrier frequency of the DSSS signal. Using these estimates, the modulation type classifier computes the normalized feature vector $\bar{\mathbf{F}}$ which is compared to the theoretical normalized feature vector of BPSK signals plotted in solid lines in Step 4 of Fig. 4.3 for different realizations of the feature vector [1]. Finally, after being classified as a BPSK signal, the DSSS classification is performed as given in [RYU13]. Note that the design variables in this example are selected so that the estimation accuracies of the *pre-processors* are on the order of 100 ppm. However, such small estimation accuracies might not be required to meet the desired classification accuracy. The aim of the next section is to analyze the maximum tolerable estimation accuracies in order to minimize the total consumed energy and processing time.

4.4 Energy Minimization Methodology

In this section, we proceed with the optimization of the design parameters in order to minimize the total consumed energy while meeting the desired classification probability.

In order to minimize the consumed energy, we split the signal processing

[1] We only require one realization of the feature vector to perform modulation-type classification, but the average detection performance is computed using multiple realizations of the feature vector

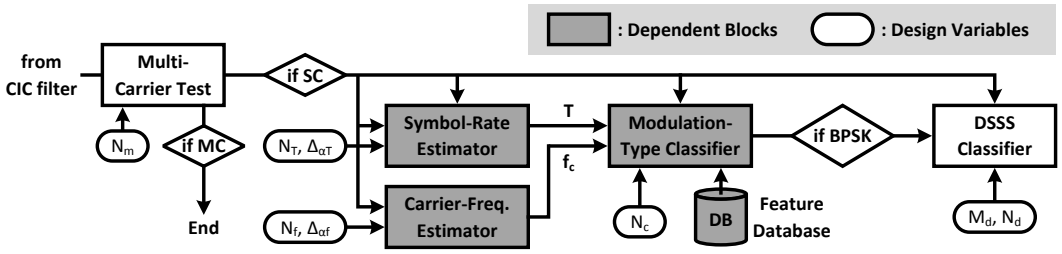

Figure 4.4: Proposed processor showing dependent blocks in gray and their design variables to be optimized.

blocks into *dependent* blocks, whose design variables are a function of the output of previous signal processing stages, and *independent* blocks, whose design variables can be set independently of the output of other blocks. For instance, the design variables of both the multi-carrier and DSSS classifiers do not depend on the output of any other stage in the classification, and are therefore labeled as *independent* blocks. On the other hand, the modulation type classifier block relies on the outputs of the *pre-processors*, and the choice of the number of samples spent for modulation type classification N_c is tightly related to the estimation accuracies of the transmit parameters. These blocks are therefore labeled as *dependent*. It is clear that the *independent* blocks consume a fixed amount of energy regardless of the other blocks, and therefore are not jointly optimized with the rest of the blocks. On the other hand, a joint optimization of the total consumed energy of the *dependent* blocks is possible. A summary of the dependent and independent blocks and their respective design variables are depicted in Fig. 4.4.

4.4.1 Energy Optimization of Dependent Blocks

In order to optimize the energy consumption of the proposed *pre-processor* and classifier, we note that all three blocks make use of the CAC statistic in (4.2). Thus, minimizing the total number of samples spent for classification is equivalent to minimizing the total consumed energy. Note that minimizing the total number of samples is also equivalent to minimizing the processing time given by $(6N_c +$

$S_T N_T + S_f N_f)T_s$, where $S_T = \lceil \mathcal{W}_T/\Delta_{\alpha_T} \rceil$ and $S_f = \lceil \mathcal{W}_f/\Delta_{\alpha_f} \rceil$. The search windows $\mathcal{W}_T$ and $\mathcal{W}_f$ are obtained from the band segmentation and are SNR dependent, and are therefore not optimized. Similarly, the number of samples per CAC computation N_T and N_f are also SNR dependent since they are the minimum required number of samples to push the noise level below the feature to be detected. At SNR of 10 dB, $N_T = N_f = 320$ samples are required to correctly estimate the symbol rate and carrier frequency. Therefore, the only variables to optimize over are N_c, S_T, and S_f, which in turn is equivalent to optimizing over N_c, Δ_{α_T}, and Δ_{α_f}.

The objective function that minimizes the total consumed energy can therefore be formulated as follows

$$\begin{aligned} &\min_{N_c, S_T, S_f} \quad 6N_c + S_T N_T + S_f N_f \\ &\text{such that } \mathcal{P}(\hat{C} = i \mid \Delta_{\alpha_f}, \Delta_{\alpha_T}, N_c, C = i) \geq 0.95 \\ &\qquad \forall i \in [1, 2, 3]. \end{aligned} \tag{4.7}$$

It is important to note that the result of the optimization problem (4.7) is a function of the coarse estimate windows $\mathcal{W}_T$ and $\mathcal{W}_f$. In fact, the wider the windows are, the larger the number of CAC computations S_T and S_f are required for a given step size Δ_{α_T} and Δ_{α_f}, respectively. Therefore, the optimum choice of the design variables is inherently tied to the coarse estimation accuracy from the band segmentation. Next, we study the tradeoffs between the symbol rate and carrier frequency estimation errors under a given probability of classification constraint. We show that there exists a region of *pre-processor* $(\Delta_{\alpha_T}, \Delta_{\alpha_f})$ pairs that satisfy the classification probability requirement.

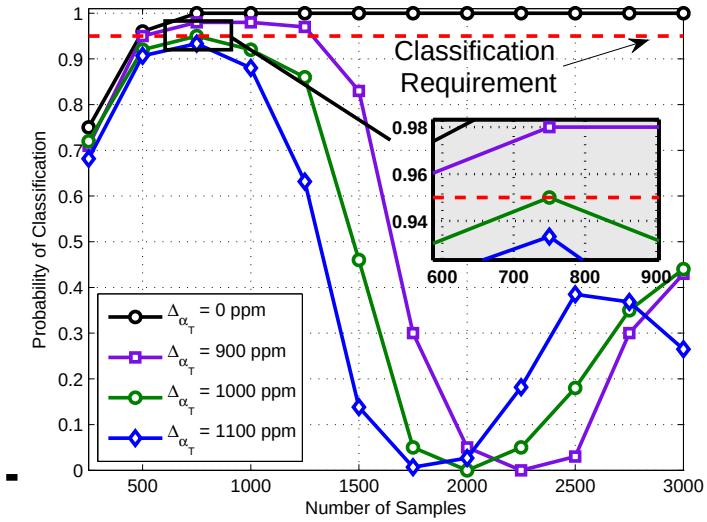

Figure 4.5: Probability of correct classification of M-QAM signals as a function of number of samples for different cyclic frequency offsets at SNR of 10 dB.

4.4.2 Tradeoffs Between Pre-Processor Accuracies

Given that signals belonging to Class 1 only exhibit a cyclostationary feature at their symbol rates, the requirement for the maximum tolerable Δ_{α_T} is determined by signals belonging to this class. The classification accuracy for Class 1 signals is shown in Fig. 4.5 as a function of the number of samples used for classification under different Δ_{α_T} values. It can be seen that the classification accuracy of QAM signals is below the desired probability of 0.95 under CFO Δ_{α_T} greater than 1000 ppm at SNR of 10 dB even when the number of samples is increased. We refer to the SNR-dependent maximum tolerable cyclic frequency offset as $\Delta_{\max \alpha_T}$. At SNR of 10 dB, $\Delta_{\max \alpha_T}$ =1000 ppm. Therefore, as long as the symbol rate estimator guarantees an accuracy less than 1000 ppm, signals belonging to Class 1 can meet the required classification accuracy. Further, since the cyclostationary feature at the symbol rate is the weakest among all cyclostationary features [Gar88], it requires the most number of samples to be detected. Therefore, the number of samples spent during classification N_c is determined by signals of Class 1 for every $\Delta_{\alpha_T} \leq \Delta_{\max \alpha_T}$.

The accuracy of the carrier frequency estimation error Δ_{α_f} is determined by the modulations that exhibit a cyclostationary feature at the carrier frequency, namely signals belonging to Class 2 and 3. However, unlike the accuracy requirement for the symbol-rate estimate which is governed by signals belonging to Class 1, Δ_{α_f} has to be jointly determined for every $\Delta_{\alpha_T} \leq \Delta_{\max \alpha_T}$. As a result, for every $\Delta_{\alpha_T} \leq \Delta_{\max \alpha_T}$ that guarantees proper classification of Class 1 signals, there exists a maximum estimation error $\Delta_{\max \alpha_f}$ that can be tolerated by Class 2 and 3 signals. Therefore, in order to understand the tradeoffs between the accuracies of both *pre-processors*, we obtain the feasible region in the $(\Delta_{\alpha_T}, \Delta_{\alpha_f})$ coordinate system under which the classification accuracy for all classes is met.

For every $\Delta_{\alpha_T} \leq \Delta_{\max \alpha_T}$ and N_c that meet the classification accuracy of Class 1 signals, the maximum tolerable CFO $\Delta_{\max \alpha_f}$ is the result of the following optimization:

$$\begin{aligned} &(\Delta_{\max \alpha_f} \mid N_c, \Delta_{\alpha_T}) = \max \quad \Delta_{\alpha_f} \\ &\text{such that} \quad \mathcal{P}(\hat{C} = i \mid \Delta_{\alpha_f}, \Delta_{\alpha_T}, N_c, C = i) \geq 0.95, \end{aligned} \tag{4.8}$$

where C is the correct class to which the received signal belongs to, and $i \in [2, 3]$. Therefore, for every $\Delta_{\alpha_T} \leq \Delta_{\max \alpha_T}$, there exists a maximum $\Delta_{\max \alpha_f}$ under which classification requirement of 95% is met.

This tradeoff among different set of triplets is illustrated in Fig. 4.6 for SNR of 10 dB. We note the tradeoff between accuracies of the two *pre-processors*, and their respective impact on N_c. It turns out that setting a stricter requirement on the symbol-rate estimator relaxes the required accuracy of the carrier frequency estimator. As expected, changing Δ_{α_T} results in different number of samples required for classification as discussed earlier. It is important to note that the tradeoff saturates after a certain point. In fact, spending more energy in the symbol rate estimator to push Δ_{α_T} below 700 ppm does not result in a relaxation of the carrier frequency estimator requirement. As a result, the cyclostationary

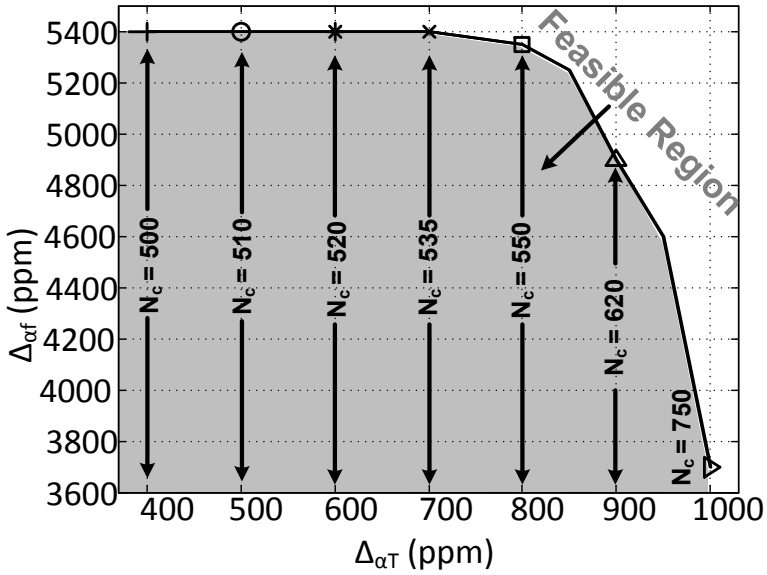

Figure 4.6: Tradeoff between the symbol rate estimator and carrier frequency estimator accuracies at SNR of 10 dB in order to meet a classification probability of 0.95 for all classes with the corresponding number of samples.

features at a function of the carrier frequency cannot be detected reliably with an offset larger than 5400 ppm at SNR of 10 dB. In addition, the maximum tolerable estimation accuracy for the carrier frequency Δ_{α_f} given the accuracy of the symbol rate estimation Δ_{α_T} is denoted in Fig. 4.6 by markers. From an energy point of view, for a given Δ_{α_T} and the corresponding N_c samples spent in the modulation classification, setting $\Delta_{\alpha_f} = \Delta_{\max \alpha_f}$ minimizes the total consumed energy of the *pre-processor*. Therefore, although there exists an infinite number of $(\Delta_{\alpha_T}, \Delta_{\alpha_f}, N_c)$ triplets that meet the required classification probability, the most energy-efficient triplets lie on the boundary of the feasible region shown in Fig. 4.6.

4.5 Design Verification

This section discusses the Simulink-based functional verification of the proposed processor. We then use the power estimates from synthesized RTL code to compute the total consumed energy of the processor at a SNR of 10 dB.

4.5.1 Simulink Design Environment

We have developed a Simulink-level experiment to run Monte-Carlo simulations in order to verify the functionality of the proposed processor, the hierarchy of which is similar to the one shown in Fig. 4.1. This processor is connected to the emulated RF front-end and band segmentation, which digitizes and senses the 500 MHz wide spectrum respectively. Each of the signal processing kernels has been implemented using Simulink embedded functions which effectively proves the low algorithmic complexity of our implementation. The Simulink design environment was used to test different signal types under different scenarios. Further, the Simulink environment is used to generate test vectors for testing the RTL code as well as demonstrate the functionality of the different algorithms that compose the processor.

4.5.2 Total Processing Time and Consumed Energy

The proposed processor was implemented in a 40-nm CMOS technology [RYU13], and consumes 10 mW at 500 MHz from a supply voltage of 0.9 V, which is equivalent to 20 pJ/sample. Substituting this number into the proposed tradeoff analysis framework, the energy consumed by the *pre-processor* and the modulation-type classifier is computed as

$$E_T(N_c, \Delta_{\alpha_T}, \Delta_{\alpha_f}) = 20(6N_c + S_T N_T + S_f N_f) \text{ pJ}.$$

In order to solve the optimization (4.7) and obtain the consumed energy of the *pre-processor* and modulation-type classifier, we use values of $\mathcal{W}_T$ and $\mathcal{W}_f$ that correspond to the band segmentation processor [YSR11]. We implemented the band segmentation in [YSR11] and obtained coarse estimate windows for both the symbol rate and carrier frequency at SNR of 10 dB, given by $\mathcal{W}_T =$ 150 KHz, and $\mathcal{W}_f = 260$ KHz respectively. To illustrate the benefits of energy

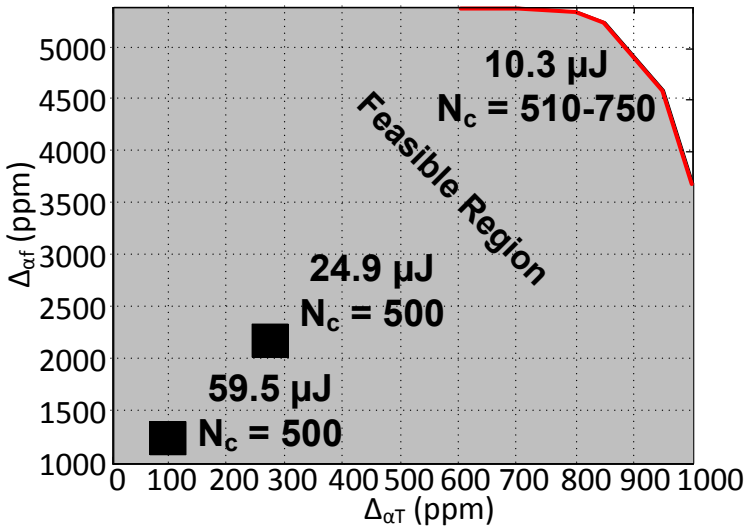

Figure 4.7: Combined energy consumed by the *pre-processor* and modulation type classifier at different $(N_c, \Delta_{\alpha_T}, \Delta_{\alpha_f})$ in the feasible region with a consumed energy of 20 pJ per sample.

minimization across the design space composed of the triplets $(N_c, \Delta_{\alpha_T}, \Delta_{\alpha_f})$, we compute the total energy for some of the triplets in the feasible region. Given the energy of 20 pJ per sample consumed by the proposed processor, we compute the energy spent by the *pre-processor* and the modulation-type classifier for a range of $(N_c, \Delta_{\alpha_T}, \Delta_{\alpha_f})$ triplet. We show in Fig. 4.7 the combined consumed energy of the *pre-processor* and modulation type classifier at SNR of 10 dB. It can be seen that the triplets that lie on the boundary of the feasible region consume the minimum amount of energy of 10.3 μJ, as compared to 24.9 μJ and 59.5 μJ for example if more processing time is spent on either of the two *pre-processors*. It is worth noting that the reason why there doesn't exist a unique optimum point for the optimization is because the $6N_c$ term in (4.7) is negligible compared to the other two terms, and therefore, there exists a range of N_c values for which the objective function is minimized.

At a clock rate of 500 MHz, the proposed processor can meet the classification requirement of 95% while consuming a total of 10.37 μJ, and a processing time of around 1 ms, meeting both energy and processing time requirements given in Table 4.1. Further, it is worth noting that the energy consumed by the *pre-*

processor and modulation type classifier constitute 99.33% of the total consumed energy which validates our reasoning behind optimizing the *dependent* blocks. Note that the proposed classifier can also perform non-blind signal classification, if the transmit parameters are known and stored in the signal database. In such an application, the total consumed energy and processing times drop dramatically to around 71 nJ and 8 μs, respectively.

4.6 Summary

A low-complexity blind modulation classification processor that operates without the knowledge of any of the parameters of the signal being processed is presented. The processor is composed of low-complexity hierarchical signal processing kernels that can classify single-carrier and multi-carrier signals. With respect to single-carrier signals, increasing the processing time during the modulation type classification does not necessarily increase the classification probability under large parameter estimation errors. As a part of the design strategies, the trade-offs between the *pre-processor* and modulation type classifier are analyzed, and an optimization framework is formulated to minimize the total consumed energy and processing time.

CHAPTER 5

Spectrum Sensing under RF Non-Linearities: Performance Analysis and DSP-Enhanced Receivers

Intermodulation products arise as a result of low noise amplifier (LNA) and mixer non-linearities in wideband receivers. In the presence of strong blockers, the intermodulation distortion can deteriorate the spectrum sensing performance by causing false alarms and degrading the detection probability. We theoretically analyze the impact of third-order non-linearities on the detection and false alarm probabilities for both energy detectors and cyclostationary detectors under front-end LNA non-linearities. We show that degradation of the detection performance due to nonlinearities of both energy and cyclostationary detection is strongly dependent on the modulation type of the blockers. We then propose two DSP-enhanced receiver architectures to compensate for the impact of nonlinearities. The first approach is a post-processing technique which compensates for nonlinearities effect on the test statistic by adapting the sensing time and detection threshold. The second approach is a pre-processing method that compensates by correcting received samples prior to computing the test statistic. This approach is based on adaptively estimating the intermodulation distortion, weighting it by a scalar constant and subtracting it from the subband of interest. We propose a method to adaptively compute the optimal weighting coefficient and show that it depends on the power and modulation of the blockers. Our results show that the pre-processing sample-based compensation method is more effective, and that

clear dynamic range extension can be obtained by using intermodulation compensation without resorting to increasing the sensing time. We also study the impact of uncertainties about the knowledge or estimates for nonlinearity parameters.

We describe in Section 5.1 the system model and formulate the wideband sensing problem in the presence of nonlinearities. In Section 5.2, we derive their theoretical probabilities of false alarm and detection under a finite number of samples for a given blocker power, SNR, and modulation types. We present in Section 5.3 the RF-aware spectrum sensing architecture and algorithm. Section 5.4 describes the adaptive method for computing the optimal cancellation coefficient for the pre-processing compensation method.

5.1 System Model

In the presence of strong inband signals, wideband sensing receivers might operate in a regime where the RF front-end components such as the LNA might saturate thus exhibiting a non-linear behavior. As a result, spurious frequencies in the form of harmonics, intermodulation (IM) and crossmodulation (XM) are generated [gha11, Raz10]. In this chapter, we consider third-order LNA non-linearities since even-order non-linearities result in IM distortion (IMD) terms outside the frequency support of wideband channel being sensed, and therefore can be efficiently filtered. Furthermore, third-order distortion typically dominates over fifth-order distortion. As a result of the third-order non-linearities, the presence of strong signals in the wideband spectrum could produce IMD terms that affect the detection performance in other subbands where weaker signals may reside [Raz10]. Under such scenarios, the detection performance might be degraded, causing the CR network to either cause harmful interference to the PU, or to miss the opportunity to transmit in a vacant subband.

We consider the problem of receiver front-end non-linearity in the sensing of a wideband spectrum which is downconverted to baseband and digitized. Then,

digital filtering is performed for the subband of interest, located in the general case at complex intermediate frequency (IF), and the resulting I/Q samples are fed to the detector to perform spectrum sensing. The non-linearity in the sensing front-end results in the generation of intermodulation terms. The odd-order non-linear terms are only considered for the modeling of the RF front-end non-linearity as the spurious frequency components that are generated by the even-order terms, i.e harmonics and inter/cross-modulation terms, are assumed to be outside of the overall digitized wideband spectrum [gha11]. Moreover, the non-linearity in the front-end is assumed to be mild and therefore is modeled with a cubic term. As a result, the baseband equivalent of the wideband signal $y_{wb}[n]$ at the output of the non-linear front-end can be described as [ZMS09]

$$y_{wb}[n] = \beta_1 x_{wb}[n] + \beta_3 x_{wb}[n]|x_{wb}[n]|^2 + w_{wb}[n], \tag{5.1}$$

where β_1, β_3 are characteristics of the sensing Rx front-end, $x_{wb}[n]$ is the received baseband equivalent wideband signal using a linear front-end, and $w_{wb}[n]$ is the additive white Gaussian noise. The values for β_1, β_3 are related to the amplitude A_{IP3} of the signal at third-order intercept point through the following expression [ZMS09]

$$A_{IP3} = \sqrt{\frac{4|\beta_1|}{3|\beta_3|}}. \tag{5.2}$$

The power of the input signal in dBm at the third-order intercept point (IIP3) is related to A_{IP3} as follows [ZMS09]

$$P_{IP3} = 20 \log_{10} A_{IP3} + 10[\text{ dBm}].$$

The IIP3 of a given receiver is defined as the input power for which the output power of the linear term equals that of the cubic term due the the third-order non-linearity. Under an example IIP3 of -10 dBm, and a linear gain of 35 dB [Raz98],

the coefficients β_1 and β_3 are given as follows

$$\beta_1 = 10^{35/20} \simeq 56.23, \beta_3 = -\frac{4\beta_1}{3A_{IP3}^2} = -7497.33. \tag{5.3}$$

As a result of the third-order non-linearity, the third-order intermodulation term of any two relatively strong signals also known as *blockers* in this context, located at f_{b1} and f_{b2} will fall in the subband of interest centered at f_c if $2f_{b1} \pm f_{b2} = f_c$ or $2f_{b2} \pm f_{b1} = f_c$. We let the SOI have a bandwidth of B Hz, and consider a receiver with an example noise figure of 4 dB. As a result, the thermal noise floor within the SOI bandwidth, referenced to the receiver input, it is given by

$$-174 \text{ dBm/Hz} + 10\log_{10}(B) + 4 \text{ dB [dBm]}. \tag{5.4}$$

In the remainder of this chapter, we consider a total receiver bandwidth of $B_{wb} =$ 500 MHz [RYU13], and a signal bandwidth of $B = 10$ MHz, resulting in a thermal noise floor in the subband of interest of -100 dBm as can be calculated using (5.4).

Then, we focus on the baseband representations of such a scenario in a given subband of interest after downconversion to an intermediate frequency f_{IF} and digital filtering. After downconversion, the blockers are located at f_1 and f_2 such that $2f_2 - f_1 = f_{IF}$. In the example of single pair of blockers, it was shown in [ZMS09] that the signal in the subband of interest is given by

$$y[n] \approx \left(\beta_1 z_0[n] + \frac{3\beta_3}{2} z_1^*[n] z_2^2[n] \right) e^{j2\pi f_{IF} n T_s} + w_z[n], \tag{5.5}$$

where T_s is the sampling period, $z_0[n]$ is the baseband version of signal of interest (SOI), $z_1[n]$ and $z_2[n]$ are the baseband representations of the blockers whose third-order IMD term falls in the subband of interest at center frequency $f_{IF} = 2f_2 - f_1$. The center frequency of the subband of interest after RF

I/Q downconversion is denoted by f_{IF} and T_s is the sampling period. Finally, $w_z[n]$ is the complex bandpass Gaussian additive noise in the subband of interest. It should be noted that in this model the assumption is that the blockers are orders of magnitude stronger than SOI, i.e. $\mathbb{E}[|z_0[n]|^2] \ll \mathbb{E}[|z_2[n]|^2]$ and $\mathbb{E}[|z_0[n]|^2] \ll \mathbb{E}[|z_1[n]|^2]$. Therefore, the additional IMD terms around f_{IF} generated by the SOI and one blocker in the form of $z_0[n]|z_1[n]|^2$ as well as the self-interference IMD term generated by the SOI in the form of $z_0[n]|z_0[n]|^2$ are negligible compared to the IMD terms of the blocker pairs. We next define the Signal to Noise Ratio (SNR) after the LNA with respect to the SOI as

$$\text{SNR} = 10\log_{10}\left(\frac{\mathbb{E}[\beta_1^2|z_0[n]|^2]}{\mathbb{E}[|w_z[n]|^2]}\right)\text{[dB]}, \tag{5.6}$$

where $\mathbb{E}[\cdot]$ is the statistical expectation operation. Further, we assume for simplicity that both blockers have the same power, i.e. $\mathbb{E}[|z_1[n]|^2] = \mathbb{E}[|z_2[n]|^2]$, and define the Signal to Blocker Ratio (SBR) as

$$\text{SBR} = 10\log_{10}\left(\frac{\mathbb{E}[|z_0[n]|^2]}{\mathbb{E}[|z_1[n]|^2]}\right)\text{[dB]}. \tag{5.7}$$

In addition, as a result of the LNA non-linearity, the blockers incur self-interference. This will be discussed in more details in Section 5.4. One illustrative example of the power spectrum density (PSD) of a two blocker case for a Rx front-end with finite IIP3 is depicted in Fig. 5.1.

The goal of the CR is to detect the presence of the weak SOI $z_0[n]$ in the presence of noise and strong blockers when $2f_2 - f_1 = f_{IF}$. The filtered signal at complex IF under both hypotheses is then given as follows

$$y[n] = \begin{cases} \frac{3\beta_3}{2} z_1^*[n] z_2^2[n] e^{j2\pi f_{IF} n T_s} + w_z[n], & \text{under } \mathcal{H}_0 \\ \\ \left(\beta_1 z_0[n] + \frac{3\beta_3}{2} z_1^*[n] z_2^2[n]\right) e^{j2\pi f_{IF} n T_s} + w_z[n], & \text{under } \mathcal{H}_1. \end{cases} \tag{5.8}$$

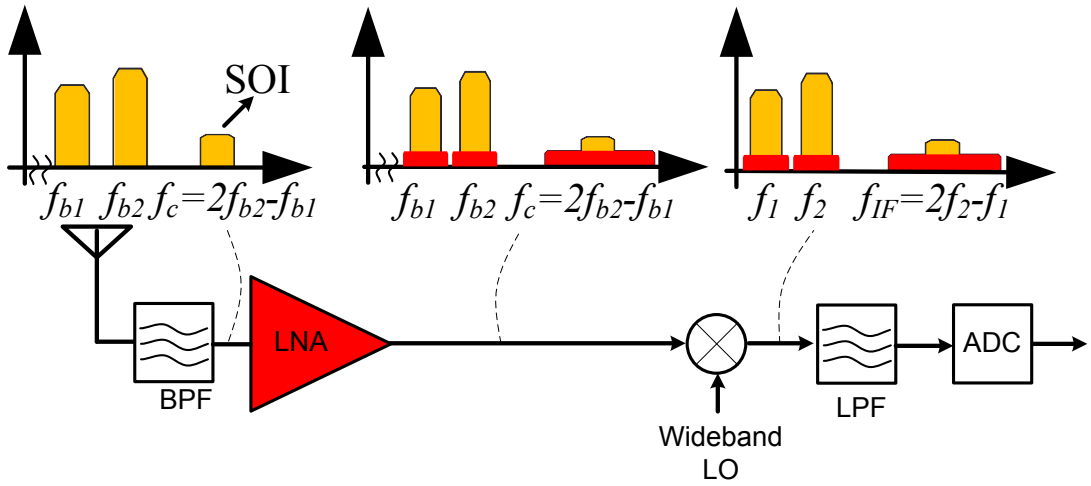

Figure 5.1: Wideband spectrum at the input and output of the non-linear front end showing the blockers self-interference, and the interference on the SOI caused by the IMD components (marked in red) that are generated by two blockers as the result of third-order non-linearity in the receiver front-end. In this example RF blockers are around frequencies f_{b1} and f_{b2}. The SOI is around frequency $f_c = 2f_{b2} - f_{b1}$.

Assuming the previous effective receiver input noise floor of -100 dBm including the receiver noise figure, and the target SNR of 5 dB for instance, the SOI power level at receiver input is -95 dBm. Then if the blockers are e.g. 60 dB more powerful (i.e. SBR $= -60$ dB), they appear at -35 dBm at receiver input. With the assumed -10 dBm receiver IIP3 figure, the third-order intermodulation is then $2 \times 25(\text{dB}) = 50$ dB below the blocker's power at the LNA output [Raz10]. But since the SOI is 60 dB below the blocker levels, the third-order IMD due to blockers at the SOI subband is actually 10dB stronger than the SOI itself. This example shows the challenging nature of the non-linear distortion with wideband receivers, and is quantified in detail in the following analysis in terms of probability of detection and false alarm.

5.2 Deriving the False Alarm and Detection Probabilities under Non-Linear Front-Ends

In this section, we derive the false alarm and detection probabilities of both ED and CD in closed form while taking into account the nonlinear behavior of the front-end. As was mentioned earlier, [RSV13] was the first paper to show the performance of ED and CD under nonlinear front-ends by simulations. However, deriving the analytical expression for P_d and P_{fa} are necessary to understand the impact of the different system parameters including the blockers' modulation type on the detection performance.

Note that since the test statistic under energy detection is a special case of the CAC, we will derive the second-order moments for both conjugate and non-conjugate CACs, which covers all possible detectors considered in this work. Given that signal, IMD term, and noise are all mutually statistically independent, the CAC of the received signal $y[n]$ is equivalent to the sum of the CAC of each of the components. As a result, we first derive the second-order statistics of the CAC under noise only, signal only, and IMD term only scenarios, respectively, and add their moments to obtain the distribution of the test statistic.

5.2.1 Noise-Only Case

We let the complex bandpass filter applied to $y_{wb}[n]$ for subband selection be denoted by $h[n]$ and composed of L_{taps} taps with unit power, i.e. $\sum_{\ell=1}^{L_{taps}} |h[\ell]|^2 = 1$. We define the following variables $\sigma_{nc}^2 \triangleq \mathbb{E}[w_{wb}^2]$, $\sigma_c^2 \triangleq \mathbb{E}[|w_{wb}|^2]$.

When the lag $\nu \geq L_{taps}$, $\mathbb{E}\big[w_z[n]w_z[n-\nu]\big] = \mathbb{E}\big[w_z[n]\big]\mathbb{E}\big[w_z[n-\nu]\big] = 0$. As a result, the mean of both conjugate and non-conjugate CAC under a lag $\nu \geq L_{taps}$

is equal to zero. By letting $\mathcal{I}(x) = 1$ if $x \geq 1$ and zero otherwise, we obtain then

$$\begin{cases} \mu_n^\alpha(N,\nu) = \mathbb{E}[R_{w_z}^\alpha(\nu)] = \frac{\sigma_{nc}^2 \sin(N\pi\alpha T_s)}{N\sin(\pi\alpha T_s)} \times \mathcal{I}(L_{taps}-\nu) \sum_{\ell=1}^{L_{taps}-\nu} h[\ell]h[\nu+\ell], \\ \mu_{n^*}^\alpha(N,\nu) = \mathbb{E}[R_{w_z^*}^\alpha(\nu)] = \frac{\sigma_{c}^2 \sin(N\pi\alpha T_s)}{N\sin(\pi\alpha T_s)} \times \mathcal{I}(L_{taps}-\nu) \sum_{\ell=1}^{L_{taps}-\nu} h^*[\ell]h[\nu+\ell]. \end{cases}$$

If the noise samples before filtering are proper complex Gaussian distributed, then $\sigma_{nc}^2 = 0$. We define $\kappa_n^\alpha(N,\nu) = \mathbb{E}[|R_{w_z}^\alpha(\nu)|^2]$ and $\kappa_{n^*}^\alpha(N,\nu) = \mathbb{E}[|R_{w_z{}^*}^\alpha(\nu)|^2]$. The power of the non-conjugate CAC can then be found as follows

$$\begin{aligned} |R_w^\alpha(\nu)|^2 =& \frac{1}{N^2} \sum_{n_1=0}^{N-1} \sum_{n_2=0}^{N-1} \sum_{\substack{l_1=1,\\ t_1=1}}^{L_{taps}} \sum_{\substack{l_2=1,\\ t_2=1}}^{L_{taps}} h[l_1]h[t_1]h^*[l_2]h^*[t_2] w_{wb}[n_1-l_1] w_{wb}[n_1-\nu-t_1] \times \\ & w_{wb}^*[n_2-l_2] w_{wb}^*[n_2-\nu-t_2] e^{j2\pi\alpha(n_1-n_2)T_s}, \end{aligned} \tag{5.9}$$

where we refer to a summation with two indices as a double summation. The second moment $\kappa_n^\alpha(N,\nu)$ is obtained by taking the expectation of the above expression, where we note that $\mathbb{E}\big[w_{wb}[n_1-l_1]w_{wb}[n_1-\nu-t_1]w_{wb}^*[n_2-l_2]w_{wb}^*[n_2-\nu-t_2]\big]$ can take three distinct values, given as follows

$$\mathbb{E}\big[w_{wb}[\ell_1]u[\ell_2]w_{wb}^*[\ell_3]w_{wb}^*[\ell_4]\big] = \begin{cases} \mathbb{E}[|w_{wb}|^4] = 2\sigma_c^4 & \text{if } \ell_1=\ell_2=\ell_3=\ell_4 \\ \mathbb{E}[|w_{wb}|^2]^2 = \sigma_c^4 & \text{if } \ell_1=\ell_2, \ell_3=\ell_4 \neq \ell_1 \\ \big|\mathbb{E}[w_{wb}^2]\big|^2 = |\sigma_{nc}|^4 & \text{if } \ell_1=\ell_3, \ell_2=\ell_4 \neq \ell_1 \end{cases} \tag{5.10}$$

Similar steps can be taken to derive $\kappa_{n^*}^\alpha(N,\nu)$, where the same three distinct expectations arise.

5.2.2 Signal-Only Case

Let a_k denote the modulating symbols of the signal of interest, and let L denote the oversampling ratio T/T_s, where T is the symbol period. Further, let's denote

by $p[\cdot]$ the sampled pulse shaping filter. The SOI is therefore given by $\beta_1 z_0[n] = \beta_1 \sum_{k=-\infty}^{\infty} a_k p[n-kL]$. As a result, the CAC under the signal-only case is given by

$$R_{z_0}^{\alpha}(\nu) = \frac{\beta_1^2}{N} \sum_{n=0}^{N-1} \sum_{\substack{k_1=-\infty \\ k2=-\infty}}^{\infty} a_{k_1} a_{k_2} p[n-k_1 L] p[n-\nu-k_2 L] \times e^{j2\pi(2f_{IF}-\alpha)nT_s} e^{-j2\pi\nu f_{IF} T_s}. \tag{5.11}$$

For notation convenience, we denote

$$p_k^{\nu}(n) \triangleq p[n-\nu-kL]. \tag{5.12}$$

Given that consecutive information symbols are independent, the mean of the non-conjugate CAC is therefore given by

$$\mu_s^{\alpha}(N,\nu) = \mathbb{E}[R_{z_0}^{\alpha}(\nu)] = \frac{\beta_1^2}{N} \sum_{n=0}^{N-1} \sum_{k=-\infty}^{\infty} \mathcal{A}_{(2,0)} p_k^0(n) p_k^{\nu}(n) e^{j2\pi(2f_{IF}-\alpha)nT_s} e^{-j2\pi\nu f_{IF} T_s}, \tag{5.13}$$

where $\mathcal{A}_{(i,j)} \triangleq \mathbb{E}[a_k^i (a_k^*)^j]$. Similarly, the mean of the conjugate CAC is given by

$$\mu_{s^*}^{\alpha}(N,\nu) = \mathbb{E}[R_{z_0^*}^{\alpha}(\nu)] = \frac{\beta_1^2}{N} \sum_{n=0}^{N-1} \sum_{k=-\infty}^{\infty} \mathcal{A}_{(1,1)} p_k^0(n) p_k^{\nu}(n) e^{-j2\pi\alpha nT_s} e^{j2\pi\nu f_{IF} T_s}, \tag{5.14}$$

By expanding $|R_{z_0}^{\alpha}(\nu)|^2$, the term consisting of the information symbols is formed of $a_k^2 a_l^{*2}$. When $k \neq l$, $\mathbb{E}\left[a_k^2 a_l^{*2}\right] = \mathcal{A}_{20}\mathcal{A}_{20}^*$ as different information symbols are statistically independent. Similarly, when $k = l$, $\mathbb{E}\left[a_k^2 a_l^{*2}\right] = \mathcal{A}_{22}$. As a result,

the second-order moment of the non-conjugate CAC can be expanded as

$$\kappa_s^{\alpha}(N,\nu) = \mathbb{E}[|R_{z_0}^{\alpha}(\nu)|^2] = \frac{\beta_1^4}{N^2}\sum_{\substack{n_1=0\\n_2=0}}^{N-1}\Bigg[\sum_{\substack{k=-\infty\\l\neq k}}^{\infty}|\mathcal{A}_{(2,0)}|^2 p_k^0(n_1)p_{k_1}^{\nu}(n_1)p_l^0(n_2)p_l^{\nu}(n_2)+$$
$$\sum_{k=-\infty}^{\infty}\mathcal{A}_{(2,2)}p_k^0(n_1)p_k^{\nu}(n_1)p_k^0(n_2)p_k^{\nu}(n_2)\Bigg]e^{j2\pi(2f_{IF}-\alpha)(n_1-n_2)T_s}, \tag{5.15}$$

Similarly, the same result can be derived for the conjugate CAC, and is given by

$$\kappa_{s^*}^{\alpha}(N,\nu) = \mathbb{E}[|R_{z_0^*}^{\alpha}(\nu)|^2] = \frac{\beta_1^4}{N^2}\sum_{\substack{n_1=0\\n_2=0}}^{N-1}\Bigg[\sum_{\substack{k=-\infty\\l\neq k}}^{\infty}|\mathcal{A}_{(1,1)}|^2 p_k^0(n_1)p_{k_1}^{\nu}(n_1)p_l^0(n_2)p_l^{\nu}(n_2)+$$
$$\sum_{k=-\infty}^{\infty}\mathcal{A}_{(2,2)}p_k^0(n_1)p_k^{\nu}(n_1)p_k^0(n_2)p_k^{\nu}(n_2)\Bigg]e^{-j2\pi\alpha(n_1-n_2)T_s}. \tag{5.16}$$

5.2.3 IMD Term-Only Case

Let b_k and c_k denote the modulating symbols of $z_1[\cdot]$ and $z_2[\cdot]$ respectively. We define $\bar{\beta}_3 \triangleq \frac{3}{2}\beta_3$. For simplicity, we assume that the blockers and SOI use the same transmit pulse shaping filter $p[n]$. However, the theoretical analysis holds for any pulse shaping filter. The noiseless representation of the blocker-only signal is given by

$$\begin{aligned} z_{imd}[n] \triangleq& \bar{\beta}_3 z_1^*[n]z_2^2[n]e^{j2\pi f_{IF}nT_s} \\ =& \bar{\beta}_3\sum_{k=-\infty}^{\infty}b_k^* p[n-kL]\times\left(\sum_{l=-\infty}^{\infty}c_l p[n-lT]\right)^2 e^{j2\pi f_{IF}nT_s} \end{aligned} \tag{5.17}$$

It can now be shown that the mean of the conjugate and non-conjugate CAC of the $z_{imd}[\cdot]$ are given by

$$\mu_b^{\alpha}(N,\nu) = \mathbb{E}[R_{z_{imd}}^{\alpha}(\nu)] = \frac{\bar{\beta}_3^2}{N}\sum_{n=0}^{N-1}\sum_{k=-\infty}^{\infty}\mathcal{B}_{(2,0)}^{*}p_k^0(n)p_k^{\nu}(n)\times$$
$$\left[\sum_{\substack{u_1=-\infty\\u_2\neq u_1}}^{\infty}\mathcal{C}_{(2,0)}^2 p_{u_1}^0(n)^2 p_{u_2}^{\nu}(n)^2 + \sum_{l=-\infty}^{\infty}\mathcal{C}_{(4,0)}p_l^0(n)^2 p_l^{\nu}(n)^2\right]\times e^{j2\pi(2f_{IF}-\alpha)nT_s}e^{-j2\pi\nu f_{IF}T_s}, \tag{5.18}$$

$$\mu_{b^*}^{\alpha}(N,\nu) = \mathbb{E}[R_z^{\alpha}(\nu)] = \frac{\bar{\beta}_3^2}{N}\sum_{n=0}^{N-1}\sum_{k=-\infty}^{\infty}\mathcal{B}_{(1,1)}p_k^0(n)p_k^{\nu}(n)\times$$
$$\left[\sum_{\substack{u_1=-\infty\\u_2\neq u_1}}^{\infty}\mathcal{C}_{(1,1)}^2 p_{u_1}^0(n)^2 p_{u_2}^{\nu}(n)^2 + \sum_{l=-\infty}^{\infty}\mathcal{C}_{(2,2)}p_l^0(n)^2 p_l^{\nu}(n)^2\right]\times e^{-j2\pi\alpha nT_s}e^{j2\pi\nu f_{IF}T_s}, \tag{5.19}$$

where $\mathcal{B}_{(i,j)} \triangleq \mathbb{E}[b_k^i(b_k^*)^j]$, and $\mathcal{C}_{(i,j)} \triangleq \mathbb{E}[c_l^i(c_l^*)^j]$. The second-order moment of the CAC can then be obtained as follows

$$\kappa_b^{\alpha}(N,\nu) = \mathbb{E}[|R_{z_{imd}}^{\alpha}(\nu)|^2] = \frac{\bar{\beta}_3^4}{N^2}\sum_{n_1=0}^{N-1}\sum_{n_2=0}^{N-1}\left[\sum_{k=-\infty}^{\infty}\sum_{l=-\infty}^{\infty}\mathbb{E}[b_k^2 b_l^{*2}]p_k^0(n_1)p_k^{\nu}(n_1)\times\right.$$
$$\left.p_l^0(n_2)p_l^{\nu}(n_2)\right]\times\left[\sum_{u_1=-\infty}^{\infty}\sum_{u_2=-\infty}^{\infty}\sum_{q_1=-\infty}^{\infty}\sum_{q_2=-\infty}^{\infty}\mathbb{E}[c_{u_1}^2 c_{u_2}^2 c_{q_1}^{*2}c_{q_2}^{*2}]\times\right.$$
$$\left.p_{u_1}^0(n_1)^2 p_{u_2}^{\nu}(n_1)^2 p_{q_1}^0(n_2)^2 p_{q_2}^{\nu}(n_2)^2\right]\times$$
$$e^{j2\pi(2f_{IF}-\alpha)(n_1-n_2)T_s}, \tag{5.20}$$

where

$$\mathbb{E}[b_k^2 b_l^{*2}] = \begin{cases} \mathcal{B}_{(2,2)} & \text{if } k = l, \\ |\mathcal{B}_{(2,0)}|^2 & \text{if } k \neq l, \end{cases} \tag{5.21}$$

$$\mathbb{E}[c_{u_1}^2 c_{u_2}^2 c_{q_1}^{*2} c_{q_2}^{*2}] = \begin{cases} \mathcal{C}_{(4,4)} & \text{if } u_1 = u_2 = q_1 = q_2, \\ |\mathcal{C}_{(4,0)}|^2 & \text{if } u_1 = u_2, q_1 = q_2, \\ \mathcal{C}_{(4,0)}\mathcal{C}_{(0,2)}^2 & \text{if } u_1 = u_2 \neq q_1, q_1 \neq q_2, \\ \mathcal{C}_{(4,0)}^*\mathcal{C}_{(0,2)}^{*2} & \text{if } q_1 = q_2 \neq u_1, u_1 \neq u_2, \\ \mathcal{C}_{(2,2)}^2 & \text{if } u_1 = q_1, u_2 = q_2, \text{or } u_1 = q_2, u_2 = q_1, \\ \mathcal{C}_{(2,0)}\mathcal{C}_{(2,4)} & \text{if } u_1 \neq q_1, q_1 = u_2 = q_2, \text{or } u_2 \neq u_1, u_1 = q_1 = q_2, \\ \mathcal{C}_{(2,0)}^*\mathcal{C}_{(2,4)}^* & \text{if } q_1 \neq u_1, u_1 = u_2 = q_2, \text{or } q_2 \neq u_1, u_1 = u_2 = q_1, \\ \mathcal{C}_{(2,2)}|\mathcal{C}_{(2,0)}|^2 & \text{if } u_1 = q_2 \neq q_1, q_1 \neq u_2, \text{or } u_1 = q_1 \neq q_2, q_2 \neq u_2, \\ & \text{or } u_2 = q_2 \neq q_1, q_1 \neq u_1, \text{or } u_2 = q_1 \neq q_2, q_2 \neq u_1, \\ |\mathcal{C}_{(2,0)}|^4 & \text{if } u_1 \neq u_2 \neq q_1 \neq q_2, \\ 0 & \text{otherwise} \end{cases} \tag{5.22}$$

Similarly, the second order moment of the conjugate CAC is given by

$$\kappa_{b^*}^{\alpha}(N,\nu) = \mathbb{E}[|R_{z_{imd}{}^*}^{\alpha}(\nu)|^2] = \frac{\bar{\beta}_3^4}{N^2} \sum_{n_1=0}^{N-1} \sum_{n_2=0}^{N-1} \Bigg[\sum_{k=-\infty}^{\infty} \sum_{l=-\infty}^{\infty} \mathbb{E}[|b_k|^2 |b_l|^2] p_k^0(n_1) p_k^{\nu}(n_1) \times$$
$$p_l^0(n_2) p_l^{\nu}(n_2) \Bigg] \times \Bigg[\sum_{u_1=-\infty}^{\infty} \sum_{u_2=-\infty}^{\infty} \sum_{q_1=-\infty}^{\infty} \sum_{q_2=-\infty}^{\infty} \mathbb{E}[c_{u_1}^2 c_{u_2}^{*2} c_{q_1}^2 c_{q_2}^{*2}] \times$$
$$p_{u_1}^0(n_1)^2 p_{u_2}^{\nu}(n_1)^2 p_{q_1}^0(n_2)^2 p_{q_2}^{\nu}(n_2)^2 \Bigg] \times e^{-j2\pi\alpha(n_1-n_2)T_s}, \tag{5.23}$$

where

$$\mathbb{E}[|b_k|^2|b_l|^2] = \begin{cases} \mathcal{B}_{(2,2)} & \text{if } k = l, \\ \mathcal{B}^2_{(1,1)} & \text{if } k \neq l, \end{cases} \tag{5.24}$$

and where $\mathbb{E}[c^2_{u_1} c^{*2}_{u_2} c^2_{q_1} c^{*2}_{q_2}]$ can be found using the same conditions as in (5.22).

5.2.4 Theoretical Distribution of Conjugate and Non-Conjugate CAC

To our best knowledge, no analytical expressions for predicting the false alarm and detection probabilities under nonlinear front-ends have been published yet. Given the above theoretical second-order moments of the signal of interest, noise, and IMD term, we now find the analytical distribution of the actual test statistics used in energy and cyclostationary detectors under both $\mathcal{H}_0$ and $\mathcal{H}_1$. As the noise, signal of interest, and IMD term are mutually independent, their means and variances will add up, resulting in the following results for C-CAC and NC-CAC detectors under $\mathcal{H}_0$, where y refers to the received signal in (5.8)

$$\text{NC-CAC} \begin{cases} \mu^\alpha_y(N,\nu,\mathcal{H}_0) = & \mathbb{E}[R^\alpha_y(\nu)|\mathcal{H}_0] = \mu^\alpha_b(N,\nu) + \mu^\alpha_n(N,\nu) \\ \kappa^\alpha_y(N,\nu,\mathcal{H}_0) = & \text{Var}(R^\alpha_y(\nu)|\mathcal{H}_0) = \kappa^\alpha_b(N,\nu) \\ & -|\mu^\alpha_b(N,\nu)|^2 + \kappa^\alpha_n(N,\nu) - |\mu^\alpha_n(N,\nu)|^2. \end{cases}$$

$$\text{C-CAC} \begin{cases} \mu^\alpha_{y^*}(N,\nu,\mathcal{H}_0) = & \mathbb{E}[R_{y^*}\alpha(\nu)|\mathcal{H}_0] = \mu^\alpha_{b^*}(N,\nu) + \mu^\alpha_{n^*}(N,\nu) \\ \kappa^\alpha_{y^*}(N,\nu,\mathcal{H}_0) = & \text{Var}(R^\alpha_{y^*}(\nu)|\mathcal{H}_0) = \kappa^\alpha_{b^*}(N,\nu) \\ & -|\mu^\alpha_{b^*}(N,\nu)|^2 + \kappa^\alpha_{n^*}(N,\nu) - |\mu^\alpha_{n^*}(N,\nu)|^2. \end{cases}$$

Similarly, the second-order moments of the NC-CAC and C-CAC under $\mathcal{H}_1$

are given by

$$\text{NC-CAC}\begin{cases}\mu_y^\alpha(N,\nu,\mathcal{H}_1) = & \mathbb{E}[R_y^\alpha(\nu)|\mathcal{H}_0] = \mu_s^\alpha(N,\nu)+\mu_b^\alpha(N,\nu)+\mu_n^\alpha(N,\nu)\\ \kappa_y^\alpha(N,\nu,\mathcal{H}_1) = & \text{Var}(R_y^\alpha(\nu)|\mathcal{H}_0) = \kappa_s^\alpha(N,\nu)-|\mu_s^\alpha(N,\nu)|^2+\kappa_b^\alpha(N,\nu)\\ & -|\mu_b^\alpha(N,\nu)|^2+\kappa_n^\alpha(N,\nu)-|\mu_n^\alpha(N,\nu)|^2.\end{cases}$$

$$\text{C-CAC}\begin{cases}\mu_{y^*}^\alpha(N,\nu,\mathcal{H}_1) = & \mathbb{E}[R_{y^*}\alpha(\nu)|\mathcal{H}_0] = \mu_{s^*}^\alpha(N,\nu)+\mu_{b^*}^\alpha(N,\nu)+\mu_{n^*}^\alpha(N,\nu)\\ \kappa_{y^*}^\alpha(N,\nu,\mathcal{H}_1) = & \text{Var}(R_{y^*}^\alpha(\nu)|\mathcal{H}_0) = \kappa_{s^*}^\alpha(N,\nu)-|\mu_{s^*}^\alpha(N,\nu)|^2+\kappa_{b^*}^\alpha(N,\nu)\\ & -|\mu_{b^*}^\alpha(N,\nu)|^2+\kappa_{n^*}^\alpha(N,\nu)-|\mu_{n^*}^\alpha(N,\nu)|^2.\end{cases}$$

Further, using the central limit theorem for sufficiently large N, the distribution of the test statistics $R_y^\alpha(\nu)$ and $R_{y^*}^\alpha(\nu)$ tend to Gaussian distributions asymptotically with increasing number of samples N. As a result, given that the test statistics are both non-zero mean, $|R_y^\alpha(\nu)|$ and $|R_{y^*}^\alpha(\nu)|$ will be both Ricean distributed. Letting $\psi_y^i(N,\nu) = \sqrt{|\mu_y^\alpha(N,\nu,\mathcal{H}_i)|^2}$, and $\psi_{y^*}^i(N,\nu) = \sqrt{|\mu_{y^*}^\alpha(N,\nu,\mathcal{H}_i)|^2}$ for $i \in [0,1]$, the probability of detection and false alarm are given by

$$\text{NC-CAC}\begin{cases} P_{fa}^{nc}(\gamma_{nc}) = Q_1(\frac{\psi_y^0(N,\nu)}{\sqrt{0.5\kappa_y^\alpha(N,\nu,\mathcal{H}_0)}}, \frac{\gamma_{nc}}{\sqrt{0.5\kappa_y^\alpha(N,\nu,\mathcal{H}_0)}}),\\ P_d^{nc}(\gamma_{cd}) = Q_1(\frac{\psi_y^1(N,\nu)}{\sqrt{0.5\kappa_y^\alpha(N,\nu,\mathcal{H}_1)}}, \frac{\gamma_{nc}}{\sqrt{0.5\kappa_y^\alpha(N,\nu,\mathcal{H}_1)}}),\end{cases} \tag{5.25}$$

$$\text{C-CAC}\begin{cases} P_{fa}^{c}(\gamma_{c}) = Q_1(\frac{\psi_{y^*}^0(N,\nu)}{\sqrt{0.5\kappa_{y^*}^\alpha(N,\nu,\mathcal{H}_0)}}, \frac{\gamma_{c}}{\sqrt{0.5\kappa_{y^*}^\alpha(N,\nu,\mathcal{H}_0)}}),\\ P_d^{c}(\gamma_{c}) = Q_1(\frac{\psi_{y^*}^1(N,\nu)}{\sqrt{0.5\kappa_{y^*}^\alpha(N,\nu,\mathcal{H}_1)}}, \frac{\gamma_{c}}{\sqrt{0.5\kappa_{y^*}^\alpha(N,\nu,\mathcal{H}_1)}}),\end{cases} \tag{5.26}$$

where $Q_1(\cdot,\cdot)$ is the first-order Marcum Q function, and where the superscripts nc and c stand for non-conjugate and conjugate respectively. Further, Eq. (5.25) and (5.26) can be used to theoretically find the detection thresholds γ_{nc} and γ_{nc} to operate at a given desired false alarm rate for any given sensing time N.

Resulting from the dependency of the second-order moments of the statistic of the IMD term on high order statistics of the blockers as shown in (5.22), the false

alarm and detection probabilities of both energy and cyclostationary detectors, are dependent on the blockers' modulation types as will be shown in Section 5.5. In the following section, we show how the derived false alarm and detection probabilities are utilized to design our proposed RF-aware detector which takes into account the presence of blockers in the wideband spectrum to adapt the detection threshold and sensing time.

5.3 Nonlinearity Compensation Based on Sensing Time Adaptation and Threshold Setting

Spectrum sensing is performed by computing the C-CAC or NC-CAC, and by comparing it to a detection threshold. Setting the detection threshold is vital to selecting the operating point on the receiver operating characteristic (ROC) curve, and is therefore of great importance. As shown in Section 5.2, the mean and variance of the CAC of the IMD term $z_{imd}[n]$ are dependent on the β_3 parameter, and on higher order moments of the blockers' symbols. Estimating the blockers' higher order moments can be achieved by 1) estimating the blockers' power, and 2) the blockers' modulation type. Given the blockers' modulation types, the blockers' high order moments can be found by just knowing the blockers' strength. Unlike the case of adjacent channel interference (ACI) where the threshold setting to perform at a given false alarm rate is only a function of the blocker strength [YSR11], the proposed RF-aware detector shown in Fig. 5.2 also requires the knowledge of the blockers' modulation types.

When the blockers' modulation types are unknown, blind modulation classification can be performed under high SNR of the blocker [SS00, DAB05, RYU13]. As RF-aware detectors only require classifying very strong blockers with very large SNR levels, estimating both the blockers' powers and modulation types can be performed within a short sensing time.

Stemming from the earlier model (5.5), the wideband discrete time sequence

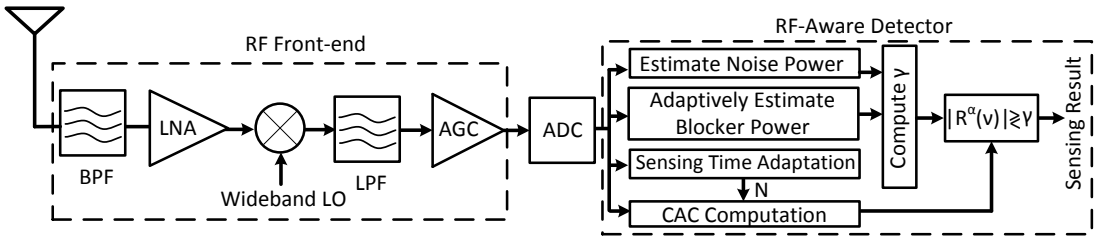

Figure 5.2: Receiver architecture of RF-aware detectors which estimates the blockers and noise power, and calculates the detection threshold γ and sensing time N that meet the desired false alarm and detection probability.

after the A/D stage is given by

$$y_{wb}[n] = \tilde{z}_1[n]e^{j2\pi f_1 nT_s} + \tilde{z}_2[n]e^{j2\pi f_2 nT_s} + \Bigg(\beta_1 z_0[n] + \frac{3\beta_3}{2} z_1^*[n] z_2^2[n]\Bigg) e^{j2\pi f_{IF} nT_s} + w_{wb}[n] \tag{5.27}$$

where $2f_2 - f_1 = f_{IF}$, $w_{wb}[n]$ is the wideband AWGN, and where $\tilde{z}_1[n]$ and $\tilde{z}_2[n]$ are composed of $z_1[n]$ and $z_2[n]$, respectively, in addition to their self-interference. The exact expression of $\tilde{z}_1[n]$ is given by

$$\tilde{z}_1[n] = \beta_1 z_1[n] + \frac{3\beta_3}{2} z_1[n]\big|z_1[n]\big|^2 + 3\beta_3 z_1[n]\big|z_2[n]\big|^2, \tag{5.28}$$

and a similar expression can be written for $\tilde{z}_2[n]$. We define $\varphi_1[n] = \tilde{z}_1[n] - \beta_1 z_1[n]$ as the blocker self-interference term. As we are considering blockers of equal strength, $\varphi_1[n] = \varphi_2[n] \triangleq \varphi[n]$, and we will therefore denote them both by $\varphi[n]$.

From (5.28), estimating the blockers strengths as seen by the LNA input cannot be performed by a time average $< |\tilde{z}_1[n]|^2 >$, as the receiver only has access to the blocker with its self-interference. As a result, we propose a new blocker power estimation algorithm that locally generates complex baseband signals $z_1^{norm}[n], z_2^{norm}[n]$ of unit energy which follow the modulation type of $z_1[n]$ and $z_2[n]$. We focus below on estimating the actual power of $z_1[n]$. In practice, estimation of both blockers' powers is needed when the two blockers are of un-

equal powers. We propose an adaptive method to estimate the true blocker power $\mathbb{E}[|z_1[n]|^2]$ [1]from the time average power estimator $\eta \triangleq < |\tilde{z}_1[n]|^2 >$, where $< \cdot >$ denotes the time averaging operation. The cost function is given by

$$\min_{\mathcal{P}} \mathbb{E}[\big(|\bar{z}_1[n]|^2 - \eta\big)^2], \text{where} \tag{5.29}$$

$$\begin{aligned}\bar{z}_1[n] &= \mathcal{P} \times \beta_1 z_1^{norm}[n] + \mathcal{P}^3(1.5\beta_3 z_1^{norm}[n]|z_1^{norm}[n]|^2 + \\ &\quad 3\beta_3 z_1^{norm}[n]|z_2^{norm}[n]|^2) \\ &\triangleq \mathcal{P}F_1 + \mathcal{P}^3 F_2\end{aligned} \tag{5.30}$$

where $\mathcal{P}$ is the scaling factor that corresponds to the correct amplitude (voltage) of the blockers. This optimization problem can be solved via, e.g., the LMS algorithm. Taking the gradient of the cost function with respect to the scaling factor $\mathcal{P}$, we get the following update equation

$$\begin{aligned}&\mathcal{P}[n+1] = \mathcal{P}[n] - \mu\Big\langle 4\mathcal{P}[n-1]^3|F_1|^4 + 12\mathcal{P}[n-1]^{11}|F_2|^4 \\ &+ 16\mathcal{P}[n-1]^7|F_1|^2|F_2|^2 + 32\mathcal{P}[n-1]^7\Re\{F_1F_2^*\}^2 + 24\times \\ &\mathcal{P}[n-1]^5\Re\{F_1F_2^*\}|F_1|^2 + 40\mathcal{P}[n-1]^9\Re\{F_1F_2^*\}|F_2|^2 - \\ &4\eta\mathcal{P}[n-1]|F_1|^2 - 12\eta\mathcal{P}[n-1]^5|F_2|^2 - 16\eta\mathcal{P}[n-1]^3\Re\{F_1F_2^*\}\Big\rangle.\end{aligned} \tag{5.31}$$

Once the blockers' powers have been estimated, the high-order moments (5.21) and (5.22) can therefore be computed. Then, the RF-aware detector utilizes the receiver β_3 parameter assumed to be known[2] and the estimated blockers' strengths to choose the sensing time N and set the detection threshold in order to meet the

[1]Note that we do not consider the linear gain of the receiver chain after the LNA in our analysis. However, the linear gain can be factored out as it is a common factor to all terms in $y[n]$.

[2]When unknown, the receiver IIP3 (and equivalently β_3) can be estimated, e.g., by means of a training sequence consisting of two strong blockers that is fed into the receiver input, followed by an adaptive algorithm [RSV13] that minimizes the power in the subband where the IMD term falls.

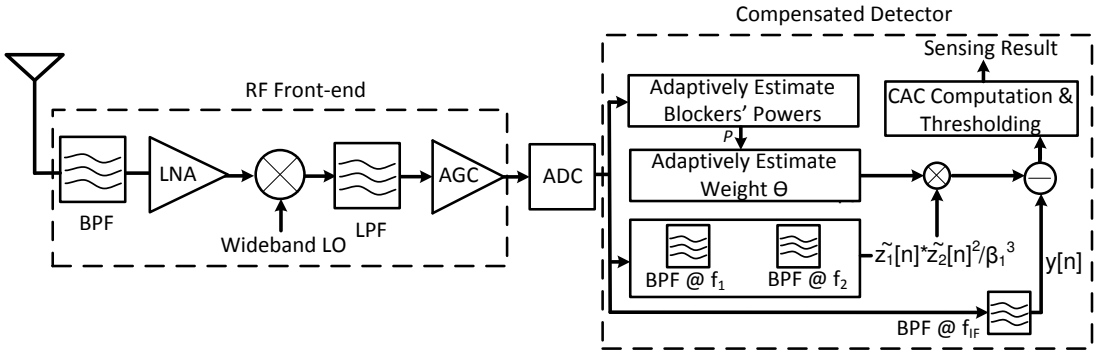

Figure 5.3: Receiver architecture of compensated detectors which adaptively estimates the blockers' strengths, and optimum weight θ in order to minimize the power of the residual term $e[n]$ in the subband of interest.

desired false alarm and detection probabilities according to (5.25) and (5.26).

5.4 Nonlinearity Compensation Through Sample-Based Intermodulation Cancellation

The proposed RF-aware spectrum sensing receiver takes into account the presence of strong blockers in the wideband channel to set the sensing time and detection threshold. Typically, the receiver resorts to increasing the sensing time as compared to AWGN scenarios in order to combat the loss in effective signal to blocker and noise ratio (SBNR), defined as the ratio of the power of SOI to that of the blocker and noise. As an alternative approach, we propose in this section a novel compensation algorithm that first estimates the IMD term, and then subtracts it from $y[n]$ in order to improve the detection performance of both cyclostationary and energy detectors without incurring any additional sensing time increase as compared to the RF-aware detector.

The signal processing kernels used in the proposed compensation scheme are shown in Fig 5.3. While filtering $y_{wb}[n]$ to get (5.5), we extract the complex IF blockers by additional appropriate bandpass filtering stages applied to $y_{wb}[n]$, and use them to estimate the intermodulation term that falls in the subband of

interest given by (up to a scaling factor β_3)

$$\hat{z}[n] = \frac{1}{\beta_1^3}\tilde{z}_1^*[n]\tilde{z}_2^2[n]. \tag{5.32}$$

Our previous compensation method presented in [RSV13] is performed by subtracting the IMD estimate in the subband of interest as follows

$$\tilde{y}[n] = y[n] - \frac{3}{2}\theta\hat{z}[n] = y[n] - \frac{3\theta}{2\beta_1^3}\tilde{z}_1^*[n]\tilde{z}_2^2[n], \tag{5.33}$$

where θ is the scaling factor of $\hat{z}[n]$. Although setting $\theta = \beta_3$ might seem as the intuitive scaling factor to suppress the IMD term, we show in this section that the optimal θ is a function of the blockers' strengths and their modulation types. Intuitively, even in the absence of noise in the subbands where the blockers reside, the filtered signals $\tilde{z}_1[n]$ and $\tilde{z}_2[n]$ will never be equal to $\beta_1 z_1[n]$ and $\beta_1 z_2[n]$ as a result of the self interference of the two blockers as shown in (5.28). As a result, as the power of the blocker self-interference $\varphi[n]$ increases when the blockers are very strong, complete suppression of the IMD term is not possible. We denote by $e[n]$ the residual term in the subband of interest after subtracting $\frac{3}{2}\theta\hat{z}[n]$ from $z_{imd}[n]$ defined in (5.17).

For the strong blockers, we neglect the impact of noise on $e[n]$ as the Blocker to Noise Ratio BNR $\gg 1$. Keeping only up to the 5^{th} order terms, the residual term $e[n]$ is given by

$$\begin{aligned} e[n] \simeq & \frac{3}{2}\beta_3 z_1^*[n]z_2^2[n]^2 - \frac{3}{2}\theta z_1^*[n]z_2^2[n] - \frac{45\theta\beta_3}{4\beta_1}z_1^*[n]z_2^2[n]|z_1[n]|^2 \\ & - \frac{9\theta\beta_3}{\beta_1}z_1^*[n]z_2^2[n]|z_2[n]|^2. \end{aligned} \tag{5.34}$$

As a result, even when $\theta = \beta_3$ the residual term $e[n]$ will be non-zero and will be composed of the last two terms in (5.34). It is not always true that setting $\theta = \beta_3$ will minimize $\mathbb{E}[|e[n]|^2]$. In fact, the weight θ should be chosen to minimize the

following cost function

$$\hat{\theta} = \arg\min \mathbb{E}[|e[n]|^2], \tag{5.35}$$

which would maximize the performance of the proposed compensation for a given sensing time constraint. Note that computing the power of the residual term $e[n]$ analytically is not straightforward as its terms are not independent, and therefore solving for the optimum weight θ is performed here numerically via an adaptive filter. We propose the LMS algorithm to solve for the optimum weighting factor θ. For notation, we let $e[n]$ be expressed as $e[n] = v[n] - \theta u[n]$, where

$$\begin{aligned} v[n] &\triangleq \frac{3}{2}\beta_3 z_1^*[n] z_2^2[n]^2 \\ u[n] &\triangleq \frac{3}{2} z_1^*[n] z_2^2[n] - \frac{45\beta_3}{4\beta_1} z_1^*[n] z_2^2[n] |z_1[n]|^2 - \\ &\quad \frac{9\beta_3}{\beta_1} z_1^*[n] z_2^2[n] |z_2[n]|^2. \end{aligned} \tag{5.36}$$

Let $\theta[n]$ denote the weight applied to $\hat{z}[n]$ at iteration n, the update equation is therefore given by

$$\begin{aligned} \theta[n+1] &= \theta[n] - \mu \left\langle 2\theta[n]|u[n]|^2 - u[n]v^*[n] - u^*[n]v[n] \right\rangle \\ &= \theta[n] - 2\mu \left\langle \theta[n]|u[n]|^2 - \Re\{u[n]v^*[n]\} \right\rangle \end{aligned} \tag{5.37}$$

where μ is the step size, $\Re\{\cdot\}$ extracts the real part of the argument, and where $< \cdot >$ denotes the time averaging which replaces the statistical expectation operator $\mathbb{E}[\cdot]$. Since the receiver does not have access to the interference-free signals $z_1[n]$ and $z_2[n]$ which $u[n]$ and $v[n]$ are a function of, the receiver locally generates complex baseband signals $z_1^{norm}[n], z_2^{norm}[n]$ of unit norm that follow the modulation type of the blockers $z_1[n], z_2[n]$. Once generated, the powers of $z_1^{norm}[n]$ and $z_2^{norm}[n]$ are adjusted by the scaling factor $\mathcal{P}$ based to the estimated blocker power through (5.31). Then, the time-series $u[n]$ and $v[n]$ are computed and used

to estimate the optimum weight θ via (5.37).

The proposed algorithm steps are summarized in Algorithm 1. As the optimum weight θ is dependent on the SBR and modulation type of the blockers, the optimum θ should be adapted for every pair of blockers. In fact, when multiple IMD terms fall in the subband of interest, the power of the overall IMD term is equal to the sum of the power of individual IMD terms as the blockers are independent. As a result, minimizing the residual IMD term per blocker pair will minimize the overall power in the subband of interest. Therefore, a parallel architecture can be adopted in the case of multiple IMD terms that fall in the subband of interest, where the optimum weight θ is computed for every pair of blockers.

Algorithm 1 Adaptive Intermodulation Term Cancellation

1: Estimate blocker powers via $\min \mathbb{E}[(|\bar{z}_1[n]|^2 - \eta)^2]$ using (5.31)
2: Find the optimum weight θ via $\min \mathbb{E}[|e[n]|^2]$ using (5.37).
3: Apply compensation algorithm (5.33) using optimum weight θ.

5.5 Numerical Results and Analysis

In this section, we verify our analysis and show the impact of the RF nonlinearities on the detection performance of both energy and cyclostationary detectors for various modulation types and modulation orders. Given that the RF-aware detector estimates the blockers' strengths and utilizes the knowledge of the receiver IIP3 to set the detection threshold, we quantify the impact of IIP3 and blockers' strength uncertainties on the false alarm probability of RF-aware detectors. Then, we show the performance gains using the proposed intermodulation term cancellation in Algorithm 1 that can be achieved for various SBR levels. The simulation settings are summarized in Table 5.1. Note that although the SBR levels considered in this work are small and go down to -85 dB, these levels are only deployed in these simulations to push the total input close to the

Table 5.1: Simulation Settings

Rx IIP3	Noise Floor in 10 MHz	Rx NF	SBR range	SNR
-10 dBm	-100 dBm	4 dB	$[-85,-60]$ dB	3 or 10 dB

IIP3. The same effects can be achieved with less severe SBR levels when multiple blocker pairs are present in the wideband channel which generate multiple IMD terms in the subband of interest.

5.5.1 Effect of Different Modulation Types and Orders on Detection Performance

In order to show the impact of the blockers' modulations on the detection performance, we focus in this subsection on different scenarios where the modulation type and/or order of the blockers are varied.

We consider first the case of non-circular blocker constellations [Pic94], i.e. $\mathbb{E}[b^2] \neq 0, \mathbb{E}[c^2] \neq 0$, where the blockers and the signal of interest are M-PAM modulated, and where b, c are the modulation symbols of $z_1[n], z_2[n]$ as shown in (5.17). In particular to the cyclostationary detection, we show the detection performance when the feature used for detection is that at twice the IF, i.e. $\alpha = 2f_{IF}$, with a lag $\nu = 0$. As the cyclic frequency α is related to the signal carrier frequency, the NC-CAC is therefore used for detection. The SBR and SNR levels are set to -67 dB and 10 dB respectively, and the sensing time is set to $N = 500$ samples. First, we note that the theoretically derived probabilities of detection and false alarm match the simulations in Fig. 5.4. As the power of the IMD term is greater than that of the noise, we are therefore operating in the interference limited scenario. It can be seen that the detection performance of both CD and ED are identical, and therefore energy detectors lose their advantage over cyclostationary detectors in the case of non-circular blockers constellation. In fact, under non-circular constellations, $\kappa_{b^*}^0(N,0) = \kappa_b^{2f_{IF}}(N,0)$, and $\mu_{b^*}^0(N,0) = \mu_b^{2f_{IF}}(N,0)$, and as a result, the impact of the IMD term on both detection

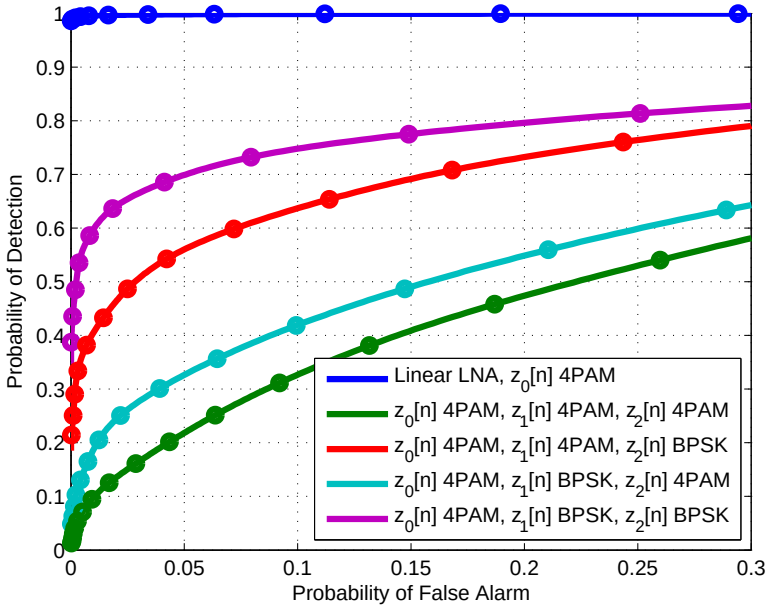

Figure 5.4: Detection performance of both cyclostationary and energy detectors (ROC curves completely overlap) under a SBR $= -67$ dB, SNR $= 10$ dB, $N = 500$ samples, for different modulation orders and the same modulation type using non-circular constellations. Solid lines represent theoretical ROC curves, and markers represent ROC curves obtained via simulations.

methods is the same.

Further, we note that changing the modulation type/order of the blocker between 4PAM and BPSK modulations impacts the detection performance of both detectors. Since both $\kappa^0_{b^*}(N,0)$ and $\mu^0_{b^*}(N,0)$ are dependent on higher order statistics of the blockers information symbols, the detection performance will therefore depend on the blockers modulation type. Since $z_2[\cdot]$ is the term that is squared as $z_{imd}[n] = \frac{3\beta_3}{2} z_1^*[n] z_2^2[n]$, the moments are therefore dominated by $z_2[\cdot]$. In fact, when the blockers have the same modulation as the SOI, the higher order moments of 4PAM modulating symbols yield a higher variance $\kappa^0_{b^*}(N,0)$, which results in a worse detection performance.

Next, we show the impact of varying the modulation type of blockers between circular and non-circular modulation schemes, while keeping the 4-PAM modulation scheme of the SOI and detecting the signal feature at $\alpha = 2f_{IF}$ and $\nu = 0$.

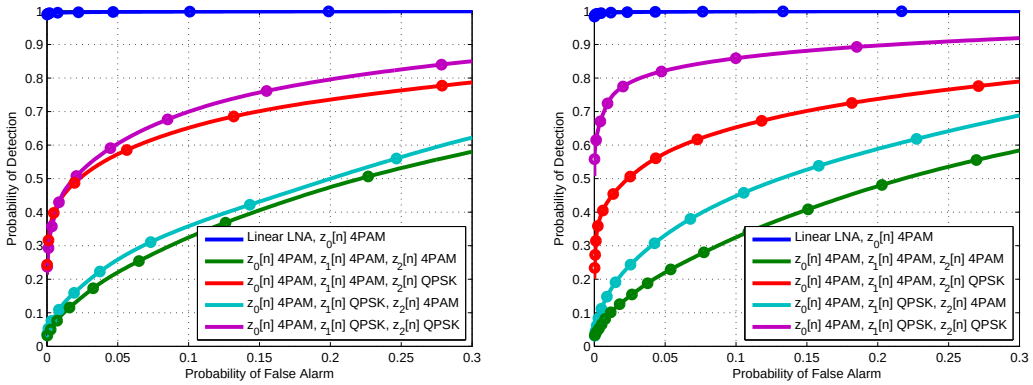

(a) Cyclostionary Detection

(b) Energy Detection

Figure 5.5: Detection performance of both cyclostationary and energy detectors under a SBR $= -67$ dB, SNR $= 10$ dB, $N = 500$ samples, for different modulation types and the same modulation order. Solid lines represent theoretical ROC curves, and markers represent ROC curves obtained via simulations.

Note that signals with circular modulation schemes such as M-PSK ($M > 2$) do not exhibit any feature at their carrier frequency. As a result, when $z_2[\cdot]$ is QPSK modulated, the detection performance is expected to be better than when it is 4PAM modulated. This is shown in Fig. 5.5(a) where we verify analytically this claim. Further, we show in Fig. 5.5(b) that in the case of circular blocker constellations, the performance of energy and cyclostationary detectors are not identical. In fact, energy detection outperforms cyclostationary detection for all considered modulation types, as is the case for linear receivers. Further, as CD is detecting the feature at $\alpha = 2f_{IF}$, the detection performance of CD is the worst among all considered modulations when the blockers are also 4PAM modulated since the SOI as well as the blockers exhibit a feature at the same cyclic frequency of interest. In contrast, the detection performance is the best when both blockers are QPSK modulated and exhibit no cyclic feature at $\alpha = 2f_{IF}$.

5.5.2 Adaptive Estimation of Blockers' Powers

Knowledge of the blockers' powers is needed for both the sensing time adaptation and threshold setting in the RF-aware detector, and for selecting the optimum

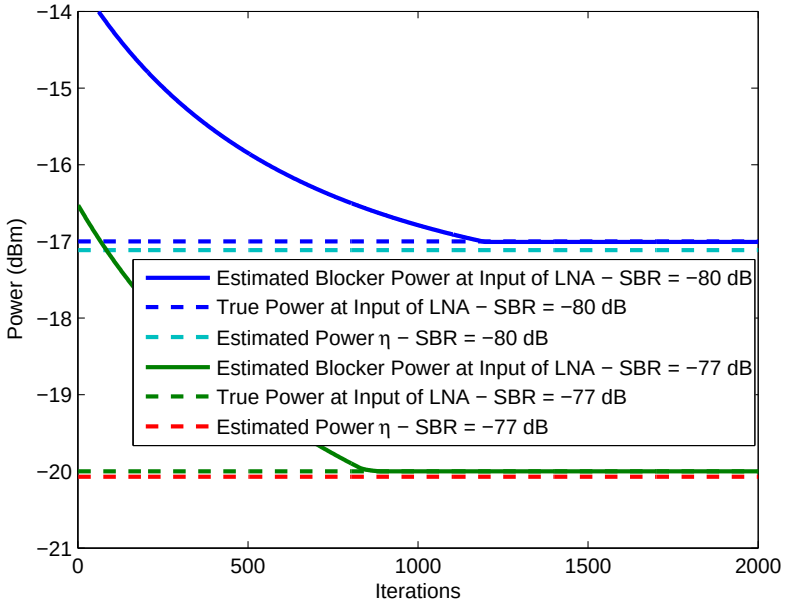

Figure 5.6: Convergence of adaptive filter (5.31) used to estimate the blocker power as seen by the LNA input under SBRs of -80 and -77 dB.

weight θ in the sample-based intermodulation cancellation receiver. However, estimating the blockers' powers directly from $\tilde{z}_1[n]$ and $\tilde{z}_2[n]$ does not result in an accurate estimate of the blocker powers as seen at the LNA input. We show in this section the convergence of the adaptive filter proposed in (5.31), whose reference signal is the estimated power of the blockers $\eta =< |\tilde{z}_1[n]|^2 >$. As shown in Fig. 5.6 under SBRs of -80 and -77 dB, the scaling factor $\mathcal{P}$ is adapted according to (5.31) such that the power of $\bar{z}_1[n]$ matches that of $\tilde{z}_1[n]$, when blockers are $QPSK$ modulated. We can see that the estimated power of $z_1[n]$ converges to the true blocker power, while η obtained from $\tilde{z}_1[n]$ is understimated. It is important to note that the gap between the true blocker power as seen by the LNA and the estimated power η decreases with increasing SBR, and is a result of the blocker self-interference $\varphi[n]$ becoming smaller with weaker total input powers[3].

[3]The impact of blocker power uncertainty on the threshold setting and therefore the false alarm probability will be addressed in Section 5.5.4

5.5.3 Detection Performance of RF-aware Detectors

As was shown in Section 5.5.1, the detection performance gets degraded in the presence of strong blockers. RF-aware detectors adapt the sensing time and detection threshold in order to operate at the desired point on the ROC curve. We show in this section the achievable performance of RF-aware detectors through the increase of sensing time. We consider the scenario with an SBR level of -70 dB, and an SNR of 3 dB. The thresholds γ_c and γ_{nc} are computed to yield a false alarm rate of 0.1 for each of the sensing times considered. Note that the receiver IIP3 is assumed to be ideally known in this case, and therefore accurate threshold setting is possible. The results are shown in Fig. 5.7 where it is shown that the detection probability of both energy and cyclostationary detectors essentially reaches 1 for linear front-ends at a sensing time of $N = 1200$ samples. However under a nonlinear front-end, RF-aware detectors achieve a detection probability of 0.8 and 0.6 for ED and CD respectively. By increasing the sensing time by five-folds ($N = 6000$), the detection probability of both ED and CD is at 0.97 and 0.92. In fact, increasing the sensing time results in an increase in the effective SINR, which improves the detection performance of both ED and CD. It is important to note that receivers operating under higher input powers will experience a more severe non-linearity behavior, and the behavior in Fig. 5.7 will be further exacerbated, resulting in a large sensing time increase to achieve the desired detection probability.

5.5.4 Impact of Parameters Uncertainty on False Alarm Probability of RF-aware Detectors

As was shown in Section 5.5.1, the derived expression can accurately estimate the false alarm probability for any given threshold γ_{nc} or γ_c in (5.25)-(5.26). As a result, RF-aware detectors utilize the knowledge of the modulation type of the blockers, β_3, and the blockers' powers to compute the threshold in order to

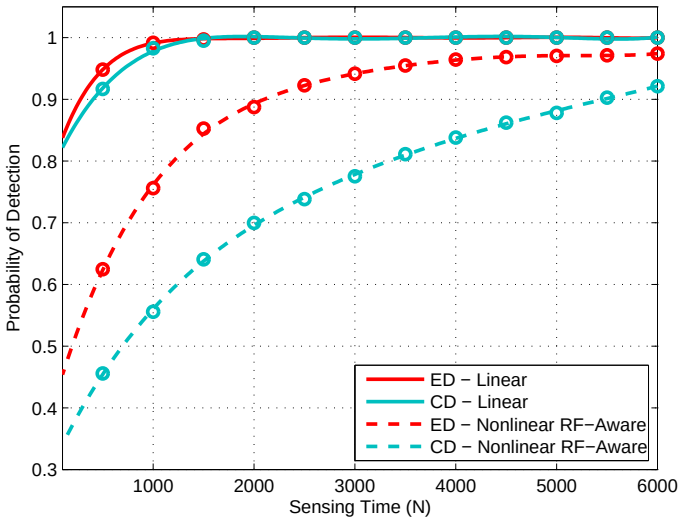

Figure 5.7: Effect of varying sensing time on the detection performance of RF-aware receivers for both energy and cyclostationary detectors at a SNR of 3 dB and SBR of -70 dB. The caption 'Nonlinear LNA' refers to the non-compensated receiver. Solid lines correspond to theoretical curves and the markers correspond to simulation results.

operate at the target false alarm rate for the desired sensing time N. However, the blockers' strength is estimated as shown in Fig. 5.2, and also the receiver parameter β_3 might not be exactly known. As a result, these parameters might not be exact and therefore the actual false alarm probability will not be equal to the target rate. We study in this section the robustness of the RF-aware detector to uncertainties in both β_3 and blocker powers.

We next show the impact of the IIP3 uncertainty on the resulting false alarm rate, where cyclostationary detection is performed on the cyclic feature $\alpha = 2f_{IF}$ and lag $\nu = 0$ using $N = 500$ samples. The detection threshold is set based on the assumption that the receiver IIP3 is at -10 dBm, with perfect knowledge of the blockers' strengths in order to achieve a target false alarm rate of 0.1. Using this fixed threshold, we sweep the receiver IIP3 uncertainty in the interval $[-1, 1]$ dB in steps of 0.2 dB. In effect, this experiment shows the resulting false alarm rate of CD and ED when the receiver sets the threshold based on an IIP3 of -10 dBm, whereas the true IIP3 is varying between -11 dBm and -9 dBm.

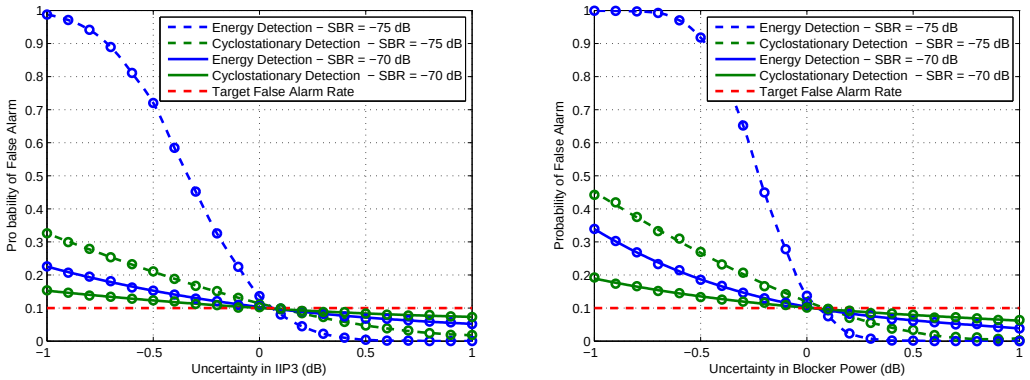

(a) Varying the IIP3 uncertainty.

(b) Varying blockers' power uncertainty.

Figure 5.8: Impact of uncertainties of IIP3 and blockers' strength on the resulting false alarm rate compared to the target false alarm rate of 0.1 using $N = 500$ samples. Solid lines correspond to theoretical results, and markers correspond to simulation results.

Fig. 5.8(a) shows the actual false alarm rate when operating using the fixed threshold computed using an IIP3 of -10 dBm. The first observation to make is that cyclostationary detectors are more robust than energy detectors with respect to IIP3 uncertainties. Second, the impact of the uncertainty on the false alarm rate is more pronounced in low SBR regimes. This is intuitive as the IMD term will have a bigger impact on the distribution of the statistic under $\mathcal{H}_0$ in lower SBR regimes, i.e. the strong blocker case. As the blocker strengths decrease, the impact of IIP3 uncertainty vanishes as the receiver operates closer to its linear region. Very similar conclusions can be made with respect to the impact of the blockers' strength uncertainty on the actual false alarm rate as shown in Fig. 5.8(b). In summary, we have shown that one other advantage of cyclostationary detectors over energy detectors is their robustness to parameter estimation errors. We note that in both Fig. 5.8(a) and Fig. 5.8(b), the uncertainty behavior is very accurately predicted using the closed form expressions (5.26) and (5.25). The theoretical curves were obtained by first computing $\nu_y^0(N,0), \nu_{y^*}^0(N,0)$ and $\kappa_y(N,0,\mathcal{H}_0), \kappa_{y^*}(N,0,\mathcal{H}_0)$ using the varying IIP3 level, and by using the selection threshold that would yield a CFAR of 0.1 under an IIP3 of -10 dBm.

5.5.5 Selecting the Optimum Weight θ for the Sample-Based Compensation Algorithm

As was pointed out in Section 5.4, the power of the residual term (5.34) is not always minimized by setting $\theta = \beta_3$. We show in this section the power of the residual term, i.e. $\mathbb{E}[|e[n]|^2]$, as a function of the θ-equivalent IIP3, defined as

$$\theta_{iip3}(\text{dBm}) = 20\log_{10}\sqrt{\frac{4|\beta_1|}{3|\theta|}} + 10[\text{ dBm}]. \tag{5.38}$$

When $\theta = \beta_3$, the θ-equivalent IIP3 will be equal to the receiver IIP3.

We show in Fig. 5.9 the power of the residual term $e[n]$ for varying θ-equivalent IIP3 values under different SBR values, a fixed SNR of 3 dB, when the blockers are 4PAM modulated. The solid lines represent the power of the residual term obtained via simulations, and the markers correspond to the power of $e[n]$ after the approximation as given in (5.34). First, we note that the power of $e[n]$ is not always minimized when $\theta = \beta_3$, or equivalently when $\theta_{iip3} = -10$ dBm. As the SBR increases, the power at the input of the LNA drops, and therefore the relative power of the blockers's self-interference drops. As the blockers become weaker, the optimum θ tends to the actual β_3 parameter of the receiver. Note that this behavior was not shown in [RSV13] where the compensation method sets θ to β_3 regardless of the power of the blockers. This is the reason for the limited compensation performance reported in [RSV13].

Similarly to the dependency of the ROC on the modulation type of the blockers, the power of the residual term $e[n]$ also varies with varying blockers' modulation type. We show in Fig. 5.10 the power of the $e[n]$ for a fixed SBR of -80 dB at an SNR of 3 dB for various θ-equivalent IIP3 values when the blockers are 4PAM and QPSK modulated. In fact, this result shows that the optimum weight θ is not only dependent on the blocker power level, but also on their modulation type. This further affirms our approach in Section 5.4 that a modulation-dependent

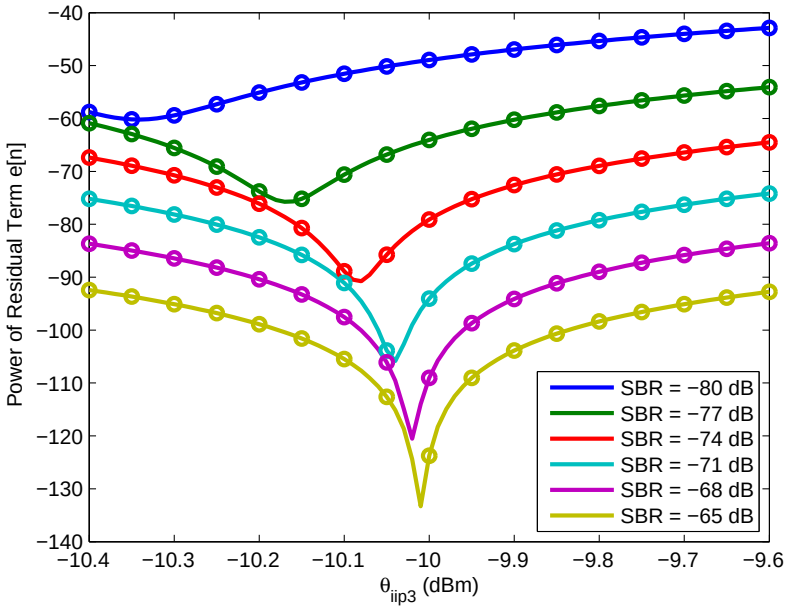

Figure 5.9: Power of residual term $e[n]$ as a function of the θ equivalent IIP3 values when blockers are 4PAM modulated under varying SBR levels for a fixed SNR of 3 dB. Solid lines correspond to the power of the residual term obtained by simulation, and the markers correspond to the power of $e[n]$ obtained through the approximation made in (5.34).

compensation algorithm is required in order to achieve the best compensation of nonlinearities.

5.5.6 Adaptive Estimation of the Compensation Coefficient θ

After estimating the scaling factor $\mathcal{P}$ that reflects the true blockers' power as seen by the LNA input, we perform the Step 2 of the Algorithm 1 which involves adaptively solving for the optimum weight θ as given by (5.37). The initial condition of the adaptive filter is set such that the θ-equivalent IIP3 is equal to the true IIP3 of the receiver, namely -10 dBm. Fig. 5.11 shows the convergence of the weight θ that should be applied to $\hat{z}[n]$ in order to minimize the power of the residual term $e[n]$ under SBR values of -80 and -77 dB. First, we note that the LMS algorithm converges to the optimum θ-equivalent IIP3 that we have shown in Fig. 5.10, and therefore the online algorithm proposed in Algorithm 1 can

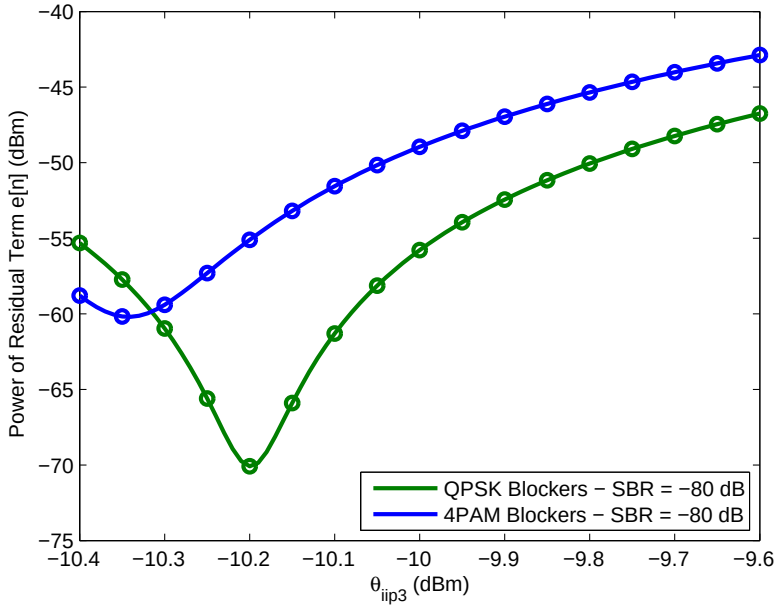

Figure 5.10: Power of residual term $e[n]$ as a function of the θ equivalent IIP3 values when blockers are 4PAM vs QPSK modulated for a fixed SBR of -80 dB, and SNR of 3 dB. Solid lines correspond to the power of the residual term obtained by simulation, and the markers correspond to the power of $e[n]$ obtained through the approximation made in (5.34).

adaptively adjust the optimum weight θ that is applied to $\hat{z}[n]$ before subtracting it from the samples $y[n]$ of the subband of interest. The next section will show the actual detection performance of energy and cyclostationary detectors after estimation of the optimum weight θ.

5.5.7 Detection Performance using the Proposed Adaptive IMD Cancellation Algorithm

We show in this subsection the impact of varying the SBR levels on the detection performance of energy and cyclostationary detectors for ideal front-ends, and non-linear front-ends using both RF-aware and compensated detectors. We set the sensing time to $N = 500$ samples, the false alarm rate to 0.1, and SNR at 3 dB. Then, we show the corresponding detection probability for varying SBR levels.

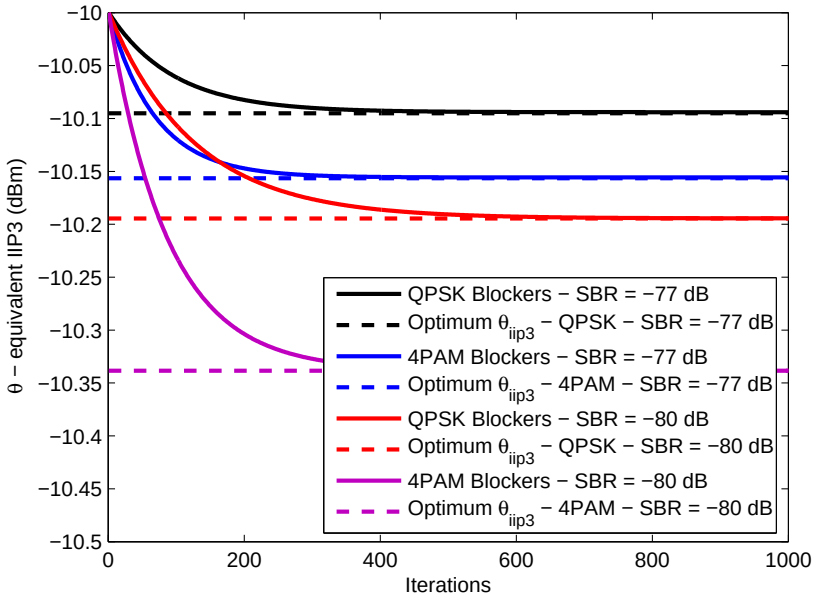

Figure 5.11: Convergence of the LMS algorithm for estimation of the optimum weight θ to minimize the power of the residual term $e[n]$ under an SBR of -80 and -77 dB, for QPSK and 4PAM modulated blockers.

Fig. 5.12 shows the detection probability of both ED and CD with varying SBR levels from -84 dB to -60 dB under two scenarios which differ by the blockers' modulations. We assume in these results that the receiver IIP3 is perfectly known. Under linear front-ends, the detection probability of ED and CD is at 0.94 and 0.91 respectively. In Fig. 5.12(a), both blockers $z_1[\cdot]$ and $z_2[\cdot]$ are QPSK modulated. In Fig. 5.12(b), both blockers and the SOI are 4PAM modulated. In both cases, the SOI $z_0[\cdot]$ is 4PAM modulated, and the detection is performed on the cyclic feature at $\alpha = 2f_{IF}$ and $\nu = 0$. First, the detection performance of RF-aware detectors starts to degrade at an SBR level of -62 dB. As a result, there is a threshold input power level of $x_{wb}[n]$ above which the detection performance of both energy and cyclostationary detectors starts to suffer. For circular constellations such as in Fig. 5.12(b), the detection performance of both CD and ED are identical as discussed in Section 5.5.1 over all ranges of SBR values where the IMD component is dominant.

Further, Fig. 5.12 shows the detection performance of the sample-based com-

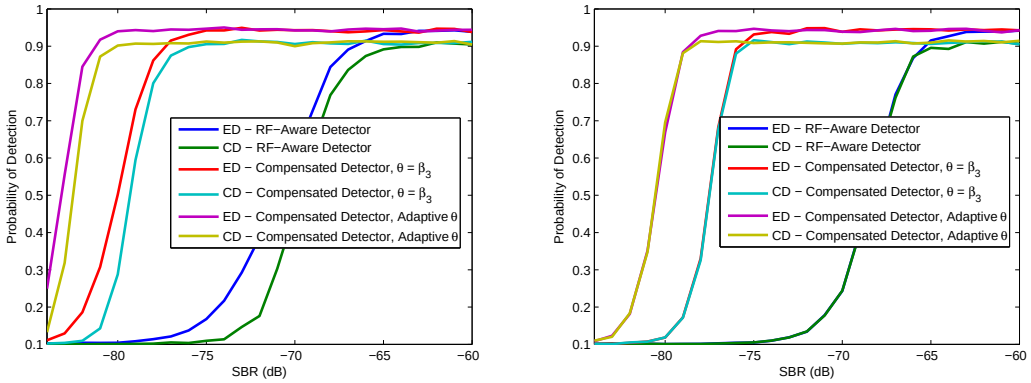

(a) QPSK Modulated Blockers

(b) 4-PAM Modulated Blockers

Figure 5.12: Effect of varying SBR levels on both energy and cyclostationary detectors at a SNR of 3 dB and fixed sensing time of $N = 500$ samples.

pensation algorithm when $\theta = \beta_3$. As a result of the blockers' self-interference at low SBR levels, the compensation algorithm fails to completely suppress the IMD term $z_{imd}[n]$ as discussed in Section 5.4. Setting $\theta = \beta_3$ does not exploit the knowledge of the modulation type of the blockers since it weights the IMD estimate by $\theta_{iip3} = -10$ dBm. In contrast, the proposed solution chooses the optimum modulation-dependent weight θ in order to minimize the power of the residual term $e[n]$ given in (5.34). In summary, a performance gain on the order of 3 dB compared to setting $\theta = \beta_3$ can be achieved for lower SBR regimes using the proposed adaptive algorithm as shown in Fig. 5.12. Note that this performance gain is achieved without incurring any additional sensing time.

5.5.8 Impact of IIP3 Uncertainty on Performance of Sample-Based Compensation Algorithm

We show the impact of IIP3 uncertainties on the ROC curve of the proposed sample-based compensation detector. As the receiver IIP3 is only needed for threshold setting in the RF-aware receiver, the IIP3 uncertainty will only affect the operating point along the ROC curve, and therefore will not degrade the ROC curve. As shown in (5.34), the residual term is a function of the β_3, which is directly related to the receiver's IIP3. When the receiver IIP3 is not exactly

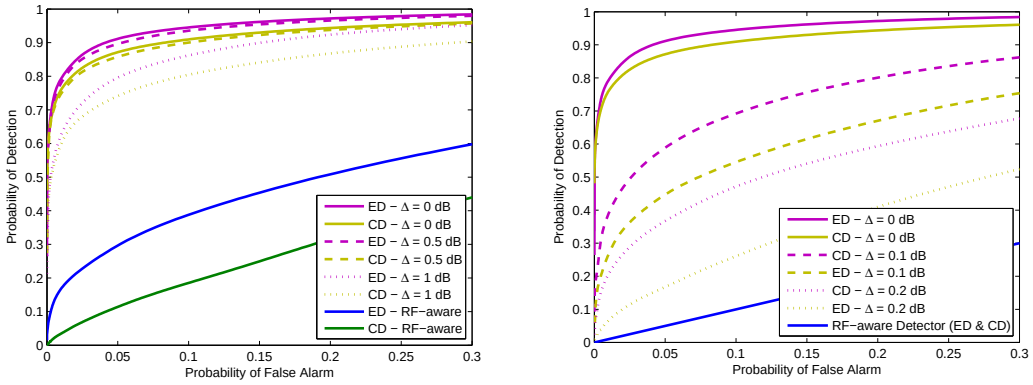

(a) SBR = −72 dB

(b) SBR = −80 dB

Figure 5.13: Effect of varying IIP3 uncertainty on the ROC curves of energy and cyclostationary detectors at a SNR of 3 dB and fixed sensing time of $N = 500$ samples for different SBR levels under QPSK modulated blockers.

known, the optimum scaling factor θ will therefore be computed based on the wrong β_3 parameter. We show in Fig. 5.13 the impact of IIP3 uncertainty Δ on the detection performance of both ED and CD. For instance, a curve annotated with $\Delta = 0.5$ dB means that the true receiver IIP3 is 0.5 dB away from the assumed one in the algorithm for estimating θ. Fig. 5.13(a) shows the ROC curves for both ED and CD under an SBR of −72 dB for various IIP3 uncertainties Δ ranging from 0 to 1 dB. Operating under an IIP3 uncertainty degrades the detection performance as the computed θ will no longer be the optimum scaling factor. Furthermore, the loss in detection performance is further exacerbated in the lower SBR regimes as shown in Fig. 5.13(b) which considers an SBR of −80 dB. In fact, this behavior is expected to occur as under the same uncertainty Δ, the power of the residual term $e[n]$ will be larger at lower SBR regimes. As a result, the behavior shown in Fig. 5.13 shows that the accuracy requirements of the receiver IIP3 are more stringent in lower SIR regimes.

5.6 Summary

This chapter studied the impact of radio front-end LNA non-linearities on both energy and cyclostationary spectrum sensing. Due to the presence of strong

blockers, the LNA could operate in its non-linear region, thus generating intermodulation terms that could fall in the subband of interest. We analytically derived the false alarm and detection probabilities of both considered detectors in closed-form and showed that the detection performance is dependent on the modulation types of the blockers and the signal of interest. Based on these results, we proposed an RF-aware detector that accounts for the RF nonlinearity by adapting the sensing time and detection threshold. We analytically quantified the robustness of RF-aware detectors to uncertainties in the receiver IIP3 and blockers' strength, and showed that cyclostationary detectors are more robust than energy detectors in that regard. Finally, we proposed a modulation-dependent intermodulation compensation algorithm that improves the detection performance of both energy and cyclostationary detectors, and have shown its robustness to IIP3 uncertainties. Our novel adaptive techniques for estimating the blockers' powers and the optimum weighting factor converge within relatively low iterations compared to the sensing time, making them attractive for real-time operation. Overall, the analysis and signal processing developments presented in this chapter demonstrate that wideband spectrum sensing receivers are very sensitive to nonlinear distortion of the RF components, and that substantial performance improvements can be obtained with DSP-enhanced receiver principles.

CHAPTER 6

Compressive Wideband Spectrum Sensing based on Cyclostationary Detection

Another challenge in deploying wideband sensing radios is the need for high-rate and high-resolution ADCs, which are hard to design and are power hungry. One solution to this problem is to adopt a compressive sensing approach, where different aliased versions of the wideband spectrum are downconverted and sampled at a lower rate than the Nyquist rate. Then, the original signal is reconstructed in DSP by means of an optimization technique that exploits the sparsity of the received signal in a given domain. We investigate in this chapter how the SCF sparsity the can be utilized to reduce the ADC sampling rates. Two such reconstruction examples can be found in [CRJ11] which uses the Modulated Wideband Converter (MWC) as the analog front-end [ME10], and [Tia11] where the SCF reconstruction is performed blindly with no *a priori* knowledge of the carriers and bandwidths of the signals to be detected.

This chapter is organized as follows. In Section 6.1, we present our system model, give a brief overview on cyclostationary-based detection using a different but equivalent approach than the one given in (2.9). In Section 6.2, we relate the SCF of the sub-Nyquist samples to the one using Nyquist samples, and formulate our reduced complexity optimization problem for reconstruction of the spectral peaks of interest. In Section 6.3 we derive the necessary conditions to guarantee a unique solution for the SCF peak reconstruction from sub-Nyquist samples. We derive in Section 6.4 the minimum sampling rate given the sparsity of the wideband channel. Section 6.5 gives the numerical results with a detailed

discussion on the regimes where a unique reconstruction of the features needed for detection is guaranteed. Finally, Section 6.6 concludes the chapter.

6.1 System Model and Problem Formulation

6.1.1 System Model

In typical CR scenarios, the sensing radios have some information about the signals to be detected. In other words, the goal of the CRs is to detect the presence or absence of one or many PUs simultaneously in a wideband channel, with *a priori* knowledge of their carrier frequencies, symbol rates, and modulation schemes. We explore a reduced complexity approach for cyclostationary detection that exploits the knowledge about carrier frequencies and signal bandwidths of the signals to be detected, and reconstructs the spectral correlation peaks of the SCF without reconstructing the Nyquist samples. In addition, to the best of the our knowledge, there has been no theoretical work with respect to the minimum achievable compression ratios under a given SCF sparsity that guarantee a unique solution to the reconstruction problem. This presents a design guideline in terms of the achievable sampling rate reductions.

For a fixed T_{sense}, instead of acquiring N_T samples at a high rate f_s, we acquire M_T samples at a rate $\frac{M_T}{N_T} f_s \leq f_s$. This can be performed using architectures such as the MWC [ME10], where the wideband signal is multiplied by M random mixing sequences which alias different parts of the wideband signal to baseband. These M branches are then sampled at a lower rate, where the sum of the rates is below the Nyquist rate f_s.

We perform frame-based processing, where we let $\mathbf{z} \in \mathbb{R}^M$ denote a frame of sub-Nyquist samples. The M_T samples will result in M_T/M different frames to be processed for detection. We further assume that a single sub-Nyquist frame $\mathbf{z} \in \mathbb{R}^M$ is related to a Nyquist frame $\mathbf{x} \in \mathbb{R}^N$ via $\mathbf{z} = \mathbf{A}\mathbf{x}$, where $\mathbf{A} \in \mathbb{R}^{M \times N}$

Table 6.1: Cyclic features for some modulation classes

Modulation	Peaks at (α, f)
BPSK	$(\frac{1}{T}, f_c)$, $(2f_c, 0)$, $(2f_c \pm \frac{1}{T}, 0)$
MSK	$(\frac{1}{T}, f_c)$, $(2f_c \pm \frac{1}{2T}, 0)$
QAM	$(\frac{1}{T}, f_c)$

is the sampling matrix. If one were to adopt the MWC as the analog front-end, the matrix $\mathbf{A}$ will be composed of the Fourier series coefficients of the mixing sequences [ME10]. As a result of the matrix multiplication, the *compression ratio* is defined as $\frac{M}{N}$. Note that for practical implementation of the compressive sensing algorithms, the vector $\mathbf{z}$ can be obtained directly from any of the analog front-ends [LKD07, YH09, CZL09]. As is the case for the MWC front-end, the Fourier series coefficients (and therefore the elements of $\mathbf{A}$) will be independent from one another as the sequences are orthogonal. In this chapter, we model $\mathbf{A}$ as a random Gaussian matrix in $\mathbb{R}^{M \times N}$ with i.i.d. components.

6.1.2 Non-Asymptotic Nyquist SCF and Two-Dimensional Sparsity

We start this section by showing an alternative method for estimating the SCF using Nyquist samples. The wideband channel is first downconverted to baseband and sampled. Given that the computation of the SCF includes computing the auto-correlation averaged over different frames of samples, we consider a frame-based model, where each frame is of length N samples, and where the remaining N_T/N frames (assumed to be integer) are used for statistical averaging. Let $\mathbf{x} \in \mathbb{R}^N$ denote a single frame of samples obtained from sampling $x(t)$ at the Nyquist rate f_s.

In the context of time constrained spectrum sensing, due to the limited number of samples acquired, perfect reconstruction of the SCF is not possible. Thus, the spectrum sensing process estimates the non-asymptotic SCF based on the N_T

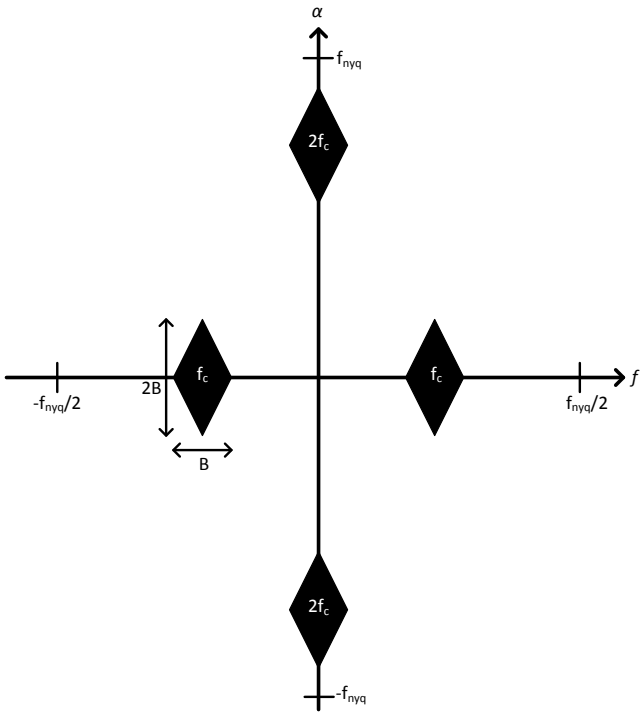

Figure 6.1: SCF Support for a Bandpass Signal.

samples acquired as follows

$$\mathbf{S}_x = \mathbf{F}_N \left(\frac{N}{N_T} \sum_{\ell=1}^{N_T/N} \mathbf{x}_\ell \mathbf{x}_\ell^T \right) \mathbf{F}_N, \tag{6.1}$$

where N_T/N is the number of spectral averages, $\mathbf{x}_\ell$ is the ℓ^{th} data frame received, and $\mathbf{F}_N$ is a $N \times N$ DFT matrix. The frame length N determines the SCF resolution in both angular and cyclic frequency (being $1/NT_s$), and the number of frames N_T/N emulates the expectation over different realizations. Note that as $N_T/N \to \infty$, the estimated discrete SCF approaches the asymptotic continuous SCF [Gar88], which is a sparse two-dimensional spectral map with non-zero features at the cyclic / angular frequency pairs shown in Table 2.1 [Gar88]. Fig. 6.1 shows the support of the SCF for a real bandlimited signal.

If we consider a sparse multiband signal $x(t)$ as in (2.1), the noise being

independent of the signal, the SCF of signal and SCF of noise are directly summed and the resultant SCF is sparse in both α and f as shown in Fig. 6.1.

The aim of this work is to 1) reduce the complexity of the SCF reconstruction by making use of the known signal parameters, 2) understand the impact of compression on sensing time and the resulting sensing performance, and 3) derive the conditions needed to guarantee uniqueness of the reconstructed SCF.

6.2 Nyquist-SCF Reconstruction using sub-Nyquist Samples

In this section, we start by our first goal, and reconstruct specific points of the SCF from samples obtained via a sub-Nyquist compressed sampling receiver and detects the presence or absence of $s_k(t)$ for any given index k. We derive an expression relating the Nyquist and sub-Nyquist SCF which is subsequently used to formulate an optimization problem for reconstruction.

6.2.1 Relating Nyquist and Sub-Nyquist SCF

Since the SCF requires finding the autocorrelation of the signal being processed, we start by defining the non-asymptotic auto-correlation matrix $\mathbf{R}_z \in \mathbb{R}^{M\times M}$

$$\mathbf{R}_z = \frac{1}{L}\sum_{\ell=1}^{L} \mathbf{z}_\ell \mathbf{z}_\ell^T, \tag{6.2}$$

where $L = M_T/M$ frames of $\mathbf{z}$ are considered for statistical averaging of the covariance matrix, and $\mathbf{z}_l \in \mathbb{R}^M$ is a frame of sub-Nyquist samples. Given that our compressive sampling model is defined as $\mathbf{z} = \mathbf{A}\mathbf{x}$, it follows that the Nyquist auto-correlation matrix $\mathbf{R}_x \in \mathbb{R}^{N\times N}$ and $\mathbf{R}_z$ are related via

$$\mathbf{R}_z \;=\; \mathbf{A}\mathbf{R}_x\mathbf{A}^T \tag{6.3}$$

Vectorizing both sides of the equation gives the following

$$\mathbf{r}_z \;=\; (\mathbf{A}\otimes\mathbf{A})\mathbf{r}_x \triangleq \mathbf{\Phi}\mathbf{r}_x \tag{6.4}$$

where $\otimes$ is the Kronecker product, $\mathbf{r}_x = \text{vec}(\mathbf{R}_x)$, $\mathbf{r}_z = \text{vec}(\mathbf{R}_z)$ and $\mathbf{\Phi} = \mathbf{A}\otimes\mathbf{A} \in \mathbb{C}^{M^2\times N^2}$.

The SCF matrix $\mathbf{S}_x$ can be obtained from the auto-correlation matrix $\mathbf{R}_x$ by taking Fourier transform of $\mathbf{R}_x$ with respect to its columns on the right and rows on the left. This can be expressed as

$$\mathbf{S}_x \;=\; \mathbf{F}_N\mathbf{R}_x\mathbf{F}_N^H \tag{6.5}$$

where $\mathbf{F}_N$ is a $N\times N$ DFT matrix. Again performing the vec operation on this equation gives

$$\mathbf{s}_x = \mathbf{T}_x\mathbf{r}_x \tag{6.6}$$

where $\mathbf{s}_x = \text{vec}(\mathbf{S}_x)$ and $\mathbf{T}_x = \mathbf{F}_N\otimes\mathbf{F}_N \in \mathbb{C}^{N^2\times N^2}$. The matrix $\mathbf{T}_x$ consists of two FFT matrices $\mathbf{F}_N$ which transform the (t,τ) time-domain pair of $\mathbf{r}_x$ to the (α, f) pair in the SCF. Similarly, we obtain $\mathbf{s}_z = \mathbf{T}_z\mathbf{r}_z$ where $\mathbf{s}_z = \text{vec}(\mathbf{S}_z)$, $\mathbf{T}_z = \mathbf{F}_M\otimes\mathbf{F}_M \in \mathbb{C}^{M^2\times M^2}$ and $\mathbf{F}_M$ is a $M\times M$ DFT matrix.

The $\mathbf{T}_x$ and $\mathbf{T}_z$ matrices are full rank non-singular matrices since they are composed of DFT matrices which are also full-rank non-singular and $Rank(\mathbf{A}\otimes\mathbf{B}) = Rank(\mathbf{A})Rank(\mathbf{B})$ [DB12]. Hence, $\mathbf{T}_x^\dagger\mathbf{T}_x = \mathbf{T}_x\mathbf{T}_x^\dagger = \mathbf{I}_{N^2\times N^2}$ where $\dagger$ denotes the pseudo-inverse operation. Also, $\mathbf{T}_x$ and $\mathbf{T}_z$ are orthogonal matrices since they are formed using DFT matrices. This can be seen as follows

$$\begin{aligned}(\mathbf{F}_N\otimes\mathbf{F}_N)^T(\mathbf{F}_N\otimes\mathbf{F}_N) &= (\mathbf{F}_N^T\otimes\mathbf{F}_N^T)(\mathbf{F}_N\otimes\mathbf{F}_N)\\ &= (\mathbf{F}_N^T\mathbf{F}_N\otimes\mathbf{F}_N^T\mathbf{F}_N) = \mathbf{I}_N\otimes\mathbf{I}_N = \mathbf{I}_{N^2}\end{aligned}$$

Now, as $\mathbf{T}_x$ is an orthogonal matrix, $\mathbf{T}_x^H = \mathbf{T}_x^\dagger$ and hence $\mathbf{T}_x^H\mathbf{T}_x = \mathbf{T}_x\mathbf{T}_x^H =$

$\mathbf{I}_{N^2 \times N^2}$. We can now relate $\mathbf{s}_x$ and $\mathbf{s}_z$ using equation (6.4) as follows

$$\begin{aligned} \mathbf{T}_z \mathbf{r}_z &= \mathbf{T}_z \mathbf{\Phi} \mathbf{r}_x \\ \mathbf{s}_z = \mathbf{T}_z \mathbf{\Phi} \mathbf{r}_x &= \mathbf{T}_z \mathbf{\Phi} \mathbf{T}_x^H \mathbf{T}_x \mathbf{r}_x \triangleq \tilde{\mathbf{\Phi}} \mathbf{s}_x, \end{aligned} \tag{6.7}$$

where $\tilde{\mathbf{\Phi}} = \mathbf{T}_z \mathbf{\Phi} \mathbf{T}_x^H \in \mathbb{C}^{M^2 \times N^2}$. Eq. (6.7) relates the vectorized SCF of the sub-Nyquist samples to that of the Nyquist samples, which we want to reconstruct. In order to ensure unique SCF reconstruction, the measurement matrix $\tilde{\mathbf{\Phi}}$ must satisfy the restricted isometry property (RIP) as has been shown by [Don06], [CT06]. We show in [Jai12] that the way we construct $\tilde{\mathbf{\Phi}}$ in our algorithm guarantees that it will satisfies the RIP with high probability.

6.2.2 Reconstruction of the Nyquist SCF

The fact that the matrix $\tilde{\mathbf{\Phi}}$ satisfies RIP with high probability, which makes the Nyquist SCF reconstruction feasible. Using (6.7) we formulate the reconstruction as a standard regularized least squares problem by introducing an l_1 minimization term, namely

$$\min_{\mathbf{s}_x} ||\mathbf{s}_x||_1 + \lambda ||\mathbf{s}_z - \tilde{\mathbf{\Phi}} \mathbf{s}_x||_2^2. \tag{6.8}$$

for some $\lambda > 0 \in \mathbb{R}$.

As was shown in Section 6.1.2, the spectral correlation peaks are discrete in the cyclic frequency domain α. The resolution in both f and α is solely determined by the FFT size N, and is equal to f_s/N where f_s is the Nyquist sampling rate. Therefore, in order to detect signals in a wideband channel, the resolution required for the spectral correlation peaks to be prominent would be high, leading to a large N. This leads to a large computational complexity in (6.8) since $\mathbf{s}_x$ is in $\mathbb{C}^{N^2}$. Due to the sparsity of the vectorized SCF $\mathbf{s}_x$, we could reconstruct only the K_f points at which spectral correlation peaks would be present, hence

making the reconstruction problem more computationally efficient. The number of features K_f is a function of the number of signals present in the wideband channel, their bandwidths, the resolution of the SCF (determined by N and the sampling rate) and the modulation class of the signals being detected (see Table 2.1).

We now find an expression for K_f from the two-dimensional SCF given in Fig. 6.1. Here, each bandlimited signal with bandwidth B occupies four lozenges with diagonals B and $2B$. Hence the total number of points K_f out of N^2 points of the SCF occupied by K signals is

$$K_f = 4K(\frac{BN}{f_{nyq}})^2 \tag{6.9}$$

where $(\frac{BN}{f_{nyq}})^2$ is the area of one of the four lozenges and K is the total number of signals present. The above expression for K_f assumes that we are operating in a high SNR regime($\geq$ 10dB). At low SNRs($<$ 10dB), as the noise power is high, the PSD is not sparse any more and we include points corresponding to the entire PSD in addition to those due to the signals giving the following expression for K_f

$$K_f = 4K(\frac{BN}{f_{nyq}})^2 + N - 2K(\frac{BN}{f_{nyq}}) \tag{6.10}$$

where N accounts for N PSD points in the SCF and the factor $2K(\frac{BN}{f_{nyq}})$ accounts for the overlap between the total number of points occupied by K signals at high SNRs and the PSD.

Given that the SCF has only K_f features, the reduced dimensionality SCF is defined as

$$\hat{\mathbf{s}}_x = \mathbf{M}_f \mathbf{s}_x, \tag{6.11}$$

where $\mathbf{M}_f \in \mathbb{R}^{K_f \times N^2}$ is a diagonal matrix with elements equal to 1 at the indices of possible cyclic features and $\hat{\mathbf{s}}_x \in \mathbb{C}^{K_f \times 1}$. Furthermore, we also define the

matrix $\hat{\mathbf{\Phi}} = \tilde{\mathbf{\Phi}}_{\{j=1:K_f\}}$, which selects the corresponding K_f columns of $\tilde{\mathbf{\Phi}}$ and stores them in $\hat{\mathbf{\Phi}}$. Given that we are only reconstructing the non-zero elements of the SCF vector, we can therefore drop the ℓ_1 minimization term related to the SCF sparsity, and the unconstrained optimization problem from (6.8) becomes

$$\min_{\hat{\mathbf{s}}_x} ||\mathbf{s}_z - \hat{\mathbf{\Phi}}\hat{\mathbf{s}}_x||_2^2, \tag{6.12}$$

which is an optimization in $\mathbb{C}^{K_f}$, where $K_f \ll N^2$. This formulation renders the optimization problem more computationally efficient since the cardinality of the search space has been reduced from N^2 to K_f. The reconstruction above is a regular least squares problem which can be solved in closed form as follows

$$\hat{\mathbf{s}}_x = \hat{\mathbf{\Phi}}^{\dagger}\mathbf{s}_z \tag{6.13}$$

The solution to (6.13) is unique if the matrix $\hat{\mathbf{\Phi}}$ is full column rank. Since $\hat{\mathbf{\Phi}} = \tilde{\mathbf{\Phi}}_{\{j=1:K_f\}}$, we analyze the measurement matrix $\tilde{\mathbf{\Phi}}$ and derive the conditions which result in a unique solution to the proposed reconstruction problem.

6.3 Uniqueness of the Proposed Sub-Nyquist Reconstruction

In this section, we study the conditions under which a unique solution exists for (6.13), as a function of the cardinality of the vector $\mathbf{s}_x$, defined as

$$\mathcal{C}(\mathbf{s}_x) = ||\mathbf{s}_x||_0 \triangleq K_f. \tag{6.14}$$

As the Nyquist SCF is sparse in both its angular and cyclic frequencies, $\mathcal{C}(\mathbf{s}_x)$ is therefore smaller than N^2. In fact, $\mathcal{C}(\mathbf{s}_x)$ is determined by the number of signals present in the wideband channel, and by their bandwidths. On the other hand, the location of the non-zero elements in $\mathbf{s}_x$ is determined by the carrier frequencies

and the bandwidths of the present signals. Note that (6.14) assumes that there are K_f non-zero elements in the Nyquist SCF when the number of averages L in (6.2) are sufficient to make the SCF sparse. Under a limited number of samples, noise would no longer not contribute to K_f, and therefore K_f acts as a lower bound to the number of non-zero points in the SCF.

To study the uniqueness of the reconstructed vector we start by finding the *Rank* of the measurement matrix $\tilde{\mathbf{\Phi}} = \mathbf{T}_z \mathbf{\Phi} \mathbf{T}_x^H$. From the *Rank* property of Kronecker product of matrices we have, $Rank(\mathbf{T}_z) = M^2$ since $Rank(\mathbf{F}_M \otimes \mathbf{F}_M) = Rank(\mathbf{F}_M) Rank(\mathbf{F}_M)$. Similarly, $Rank(\mathbf{\Phi}) = M^2$ and $Rank(\mathbf{T}_x^H) = N^2$. Hence, $\tilde{\mathbf{\Phi}}$ is the product of three full-rank matrices and the $Rank(\tilde{\mathbf{\Phi}}) = \min(M^2, M^2, N^2)$ $= M^2$ since $M \leq N$.

The above statement shows that there cannot exist a set of more than M^2 columns of $\tilde{\mathbf{\Phi}}$ that are linearly independent. However, this does not mean that every set of K_f columns of $\tilde{\mathbf{\Phi}}$ are linearly independent, even if $K_f < M^2$. For this reason, we use the *Spark* of a matrix to find when a unique solution exists. The *Spark* of a matrix is defined as

$$Spark(\mathbf{A}) = \min_d ||\mathbf{d}||_0 \text{ such that } \mathbf{Ad} = 0. \tag{6.15}$$

From the definition in (6.15), the *Spark* of a matrix is the smallest number s such that there exists a set of s columns in the matrix that are linearly dependent. In other words, any subset of columns formed of less than the *Spark* of a matrix will be full column rank with probability 1. Obviously, the *Spark* of a matrix cannot be greater than its $Rank + 1$. The section below is aimed at finding the *Spark* of the matrix $\tilde{\mathbf{\Phi}}$.

6.3.1 Finding the Spark of Sensing Matrix

In order to obtain the *Spark* of $\tilde{\mathbf{\Phi}}$, we start by finding the *Spark* of the matrices that compose it. From the definition of $\mathbf{\Phi}$, we have that $\tilde{\mathbf{\Phi}} = (\mathbf{F}_M \mathbf{A} \mathbf{F}_N^H) \otimes$

$(\mathbf{F}_M \mathbf{A} \mathbf{F}_N^H)$.

Given that the sampling matrix $\mathbf{A}$ is formed of i.i.d components, its $Spark$ is equal to $M+1$ with high probability. In other words, any subset of M columns of $\mathbf{A}$ will form a full-column rank sub-matrix.

It was shown in [JM09] that if $\mathbf{A}$ is a $M \times N$ rank-deficient matrix, i.e. $Rank(A) < N$, then the $Spark(\mathbf{A} \otimes \mathbf{A}) = Spark(\mathbf{A})$. Therefore, in order to find $Spark(\tilde{\mathbf{\Phi}})$, it is sufficient to find $Spark(\mathbf{F}_M \mathbf{A} \mathbf{F}_N^H)$. From [Jai12], we know the Gaussian distribution is invariant to unitary transformation. Hence, the elements of $(\mathbf{A}\mathbf{F}_N^H)$ are also i.i.d Gaussian distributed and thus $Spark(\mathbf{A}\mathbf{F}_N^H) = Spark(\mathbf{A}) = M+1$.

Lemma 1. *Let* $\mathbf{A}$ *be a* $N \times N$ *invertible matrix, and let* $\mathbf{B}$ *be a* $N \times M$ *rank deficient matrix. Then* $Spark(\mathbf{AB}) = Spark(\mathbf{B})$.

Proof. Using the definition of $Spark$,

$$Spark(\mathbf{AB}) = \min_{\mathbf{d}} ||\mathbf{d}||_0 \text{ such that } \mathbf{ABd} = \mathbf{0}.$$

Given that matrix $\mathbf{A}$ is invertible, the constraint therefore is equivalent to $\mathbf{Bd} = \mathbf{0}$, and therefore,

$$Spark(\mathbf{AB}) = \min_{\mathbf{d}} ||\mathbf{d}||_0 \text{ such that } \mathbf{Bd} = \mathbf{0},$$

which is the definition of $Spark(\mathbf{B})$. Therefore, $Spark(\mathbf{AB}) = Spark(\mathbf{B})$. □

Let $\mathbf{T} = \mathbf{A}\mathbf{F}_N^H$, where $\mathbf{T}$ is a $N \times M$ rank deficient matrix. Given that $\mathbf{F}_M$ is invertible since it is an M-point DFT matrix, $Spark(\mathbf{F}_M \mathbf{T}) = Spark(\mathbf{T}) = M+1$ as a result of Lemma 1.

The above results prove that $Spark(\mathbf{F}_M \mathbf{A} \mathbf{F}_N^H) = Spark(\mathbf{A}) = M+1$. Hence,

this proves that $Spark(\tilde{\mathbf{\Phi}}) = M + 1$ since [JM09]

$$Spark(\mathbf{F}_M \mathbf{A} \mathbf{F}_N^H \otimes \mathbf{F}_M \mathbf{A} \mathbf{F}_N^H) = Spark(\mathbf{F}_M \mathbf{A} \mathbf{F}_N^H). \tag{6.16}$$

6.3.2 Implications of the $Spark(\tilde{\mathbf{\Phi}})$ and Uniqueness of the Solution

As a result of the *Spark* of the matrix $\tilde{\mathbf{\Phi}}$, we can guarantee that as long as $K_f < M + 1$, then the resulting matrix $\hat{\mathbf{\Phi}}$ will be full column rank and the reconstruction in (6.13) will have a unique solution. From the definition of *Spark*, this result will hold for any set of M columns. These results prove the following theorem.

Theorem 1. *There exists a unique solution to the reconstruction problem* $\mathbf{s}_z = \hat{\mathbf{\Phi}} \hat{\mathbf{s}}_x$ *with probability 1, iff* $K_f = ||\mathbf{s}_x||_0 < Spark(\tilde{\mathbf{\Phi}}) = (M + 1)$.

Proof. This is a direct result of the definition of the Spark, and Spark was proved to be equal to $M + 1$. □

Theorem 1 guarantees the existence of a unique solution if the criteria $(M + 1) > K_f$ is met with probability 1. However, the uniqueness criteria can still be met with $(M + 1) \leq K_f$ with a non-zero probability. In the section below, we show that a unique solution to the reconstruction problem can be obtained with a quite high probability even when $(M + 1) \leq K_f$, which is a typical case in the problem of reconstruction of the Nyquist SCF as $K_f \sim N^2$.

6.3.3 Probabilistic Spark of the Sampling Matrix

We have shown in the previous section that if $(M + 1) > K_f$, then the resulting reconstruction method will result in a unique solution. Further, if $K_f > M^2$, then the resulting matrix $\hat{\mathbf{\Phi}} = \tilde{\mathbf{\Phi}}_{\{j=1:K_f\}}$ will be rank deficient with probability 1 since $Rank(\hat{\mathbf{\Phi}}) = M^2$. In the regime where $(M + 1) \leq K_f \leq M^2$, the resulting matrix can be full rank with a certain non-zero probability. Let p_k be the probability

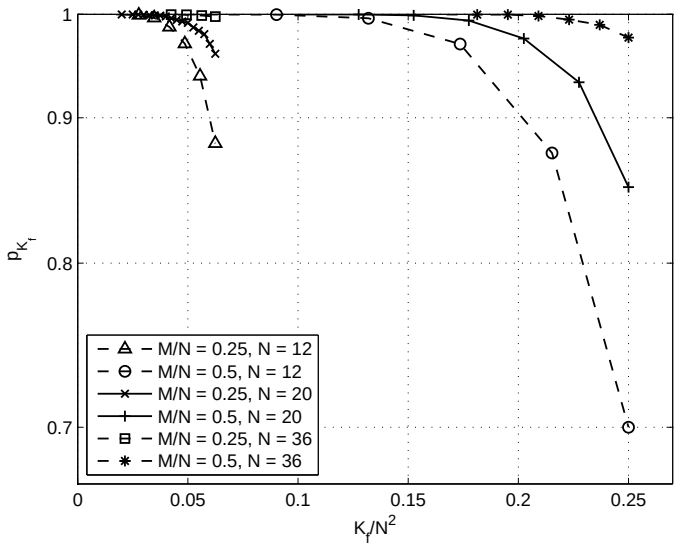

Figure 6.2: Simulation result: Probability that every K_f columns of $\tilde{\mathbf{\Phi}}$ forms a full-column rank $\hat{\mathbf{\Phi}}$, where $Spark(\tilde{\mathbf{\Phi}}) \leq K_f \leq Rank(\tilde{\mathbf{\Phi}})$ for $M/N = 0.25$ and $M/N = 0.5$ for increasing values of N.

that $\hat{\mathbf{\Phi}}$ is full column rank with $K_f = \kappa, (M+1) \leq \kappa \leq M^2$. Similar to the $Spark$ of a matrix, the probability p_k is NP-hard to compute since it requires us to find all the possible subsets of k columns of $\tilde{\mathbf{\Phi}}$ that are independent as is shown in [TP12]. In the rest of this section, we find empirically the probability p_k that the chosen matrix obtained by reconstructing $K_f \geq M+1$ features is full column rank, and hence will result in a unique reconstruction.

From the definition of the $Spark$, there is a non-zero probability of at least one subset of K_f columns being dependent where K_f is in the range $M+1 \leq K_f \leq M^2$. Here we focus on the maximum number of dependent sets of K_f columns to calculate the probability p_{K_f} that the chosen matrix is full-column rank.

Fig. 6.2 shows the probabililty p_{K_f} that all possible subsets of K_f columns of $\tilde{\mathbf{\Phi}}$ are independent as a percentage of total columns N^2. To analyze the effect of the compression ratio on p_{K_f}, we compare this for two compression ratios of $M/N = 0.25$ and 0.5. Also, at each compression ratio, we vary M and N to see if there is any gain or loss in terms of p_{K_f} while operating at

higher resolution in frequency (N). From the curves in Fig.6.2, we can make two important observations. Firstly, at lower compression ratios ($M/N = 0.25$), the probability that all subsets of $M + 1 \leq K_f \leq M^2$ columns will be independent is much higher as compared to higher M/N. This implies that the sparser the SCF is, the smaller the compression ratio can be. As a result, the probability of having a full-column matrix is higher, yielding a unique solution with a higher probability. Secondly, at a given M/N ratio, operating at higher values of M and N increases the probability of choosing a subset of K_f independent columns substantially. This results in an inherent trade-off between the reconstruction complexity which is directly proportional to M^2 and N^2 as $\mathbf{\Phi} \in \mathbb{C}^{M^2 \times N^2}$, and the probability that the solution to the reconstruction problem will be unique.

6.3.4 Condition for Uniqueness of the Reconstructed Vectorized Nyquist SCF $\hat{\mathbf{s}}_x$

The least-squares problem given in (6.12) can be solved if the system of equations is overdetermined, i.e, if $M^2 \geq K_f$. However, we have proven above that a unique solution to the reconstruction problem exists with probability 1 if $M+1 > K_f$. In addition, we have shown that if $(M+1) \leq K_f \leq M^2$, then a unique solution exists with a very high probability p_{K_f}. Thus we obtain the closed form expression of the least-squares problem whose solution is unique and always exists, resulting in the following theorem.

Theorem 2. *Let the system of equations, $\mathbf{s}_z = \hat{\mathbf{\Phi}}\hat{\mathbf{s}}_x$ be overdetermined with $M^2 \geq K_f$. The solution to the reconstruction of the cyclic features of the vectorized Nyquist SCF always exists and is unique with probability 1 iff $K_f \leq M$, or with probability p_{K_f} iff $M + 1 \leq K_f \leq M^2$, and is given by*

$$\hat{\mathbf{s}}_x = \hat{\mathbf{\Phi}}^{\dagger}\mathbf{s}_z = [\hat{\mathbf{\Phi}}^H\hat{\mathbf{\Phi}}]^{-1}\hat{\mathbf{\Phi}}^H\mathbf{s}_z. \tag{6.17}$$

In the next section, we relate the conditions for uniqueness of the reconstruc-

tion given by (6.17) to the compression ratio and the sparsity of the wideband channel.

6.4 Minimum Lossless Sampling Rates and its Relation to SCF Sparsity Level

In the compressive sensing literature, one question that often arises is how low can the compression ratio be for a given sparsity level enabling lossless recostruction of the signal. Lossless reconstruction refers to the error between original and reconstructed signal being negligible for the considered application. By only exploiting the sparsity level in the PSD, the minimum compression ratio for a non-blind reconstruction (*Landau rate*) can be as low as the spectrum occupancy [Lan67], defined as the ratio between occupied bandwidth to the total channel bandwidth. This minimum compression ratio can only be achieved in high SNR regimes SNR $>$ 20 dB, where the noise power is small relatively to the signals occupying the spectrum. At low SNRs, as the signal and noise are of similar strength, the PSD can no longer be considered sparse anymore even if the actual occupied signal bandwidth is negligible. Hence, the signal reconstruction will fail and sampling rates cannot reduced by exploiting the PSD sparsity only.

The *Landau rate*, which we define as the minimum sampling rate based on the PSD sparsity is expressed as

$$\left(\frac{M}{N}\right)_{Landau} = \frac{K_{f,PSD}}{N} = 2K\frac{B}{f_{nyq}}. \tag{6.18}$$

By operating in the cyclic domain, the sparsity has to account for non-zero cyclic frequencies as well, which yields a sparser transformation domain, and intuitively, the compression ratio can be reduced further. Since the noise is stationary, there are no features at non-zero cyclic frequencies which enables us to reduce sampling rates even at low SNRs.

From Theorem 2, we obtain a unique solution to the Nyquist SCF reconstruction with probability 1 iff $M \geq K_f$, or with probability p_{K_f} iff $M+1 \leq K_f \leq M^2$. For the case, $M \geq K_f$, the minimum sampling ratio is given by $(\frac{M}{N})_{\min} = \frac{K_f}{N}$. From (6.9) and (6.10), we have that $K_f \sim N^2$ and thus $\frac{K_f}{N} \sim N$. Hence, with increasing N, the resolution in f and α increases, and the minimum sampling ratio becomes greater than 1. This is mainly because the number of non-zero points K_f in the SCF is generally greater than M.

We now focus on the range $M+1 \leq K_f \leq M^2$ which guarantees a unique solution with probability p_{K_f}. From section IV-B, we see that the probability p_{K_f} is a function of compression ratio and N. To obtain a lower bound on the minimum sampling rate we study the case when $K_f = M^2$ which is achieved wih probability p_{M^2}. This choice of K_f is not unrealistic as is shown in section IV-B where for moderate M and N ($M = 18, N = 36$), p_{M^2} is greater than 0.98. Thus the lower bound is given by

$$\begin{aligned} \left(\frac{M}{N}\right)_{cyclic} &= \sqrt{\frac{K_f}{N^2}} \\ &= \begin{cases} 2\sqrt{K}\frac{B}{f_{nyq}} & \text{under high SNR} \\ \sqrt{\frac{4KB^2}{f_{nyq}^2} + \frac{1}{N} - \frac{2KB}{N^2 f_{nyq}}} & \text{under low SNR} \end{cases} \end{aligned} \tag{6.19}$$

where the low SNR case is obtained from (6.10). In (6.19), as $N \to \infty$, for low SNR $(\frac{M}{N})_{cyclic} \to 2\sqrt{K}\frac{B}{f_{nyq}}$ which is same as the result for high SNR. This is intuitive because as $N \to \infty$, the ratio $\frac{N}{N^2} \to 0$ and therefore the number of PSD points are negligible compared to the area of the SCF. Thus asymptotically the minimum sampling ratio is independent of SNR.

The minimum sampling rate for $K_f = M(M+1)/2$ under a high SNR regime can similarly be expressed as

$$\left(\frac{M}{N}\right)_{cyclic} = \frac{-1 + \sqrt{1 + \frac{32KN^2B^2}{f_{nyq}^2}}}{2N}. \tag{6.20}$$

Comparing the expressions for minimum achievable sampling ratios in (6.18) and (6.19) corresponding to Energy and Cyclostationary detection respectively, it is evident that Cyclostationary detectors require lower sampling rates for the same PSD sparsity levels for both high and low SNR regimes. As this difference in minimum sampling ratios is $\sim \sqrt{K}$, where $K > 1$, with increasing number of signals in the band/decreasing sparsity, Cyclostationary detectors have correspondingly increasing gains compared to Energy detectors.

6.5 Discussion And Numerical Results

We consider a wideband channel of bandwidth 300 MHz, occupied with K BPSK signals one of which is the signal of interest (SOI). Each of the K signals has an effective signal bandwidth of 15 MHz (taking into account the roll-off factor of the pulse-shaping filter). As mentioned earlier, we assume an equal in-band SNR for all signals, and a frame length $N = 36$ samples. The spectral correlation peak considered for single-cycle detection is at $(\alpha, f) = (2f_c, 0)$. In Section 6.5.1, we compare the minimum compression ratios of the proposed detector to that of energy detection at low and high SNRs. In Section 6.5.2, the reconstruction error is shown in terms of the resulting MSE for various compression ratios. Section 6.5.3 shows the relationship between the required sensing time for a given SNR and PSD sparsity to reach a desired point on the ROC curve. Finally, Section 6.5.4 shows the effect of the sensing time, compression ratio, and SNR on the resulting ROC curves.

6.5.1 Theoretical Minimum Lossless Compression

Here, we compare the minimum lossless sampling rates obtained from the Landau rate in (6.18) and the lower bounds on sampling rates for Cyclostationary detectors corresponding to $K_f = M^2$ and $M(M+1)/2$ in (6.19) and (6.20). From Fig. 6.3(a), we observe that at high SNRs, when the PSD is fully occupied and there-

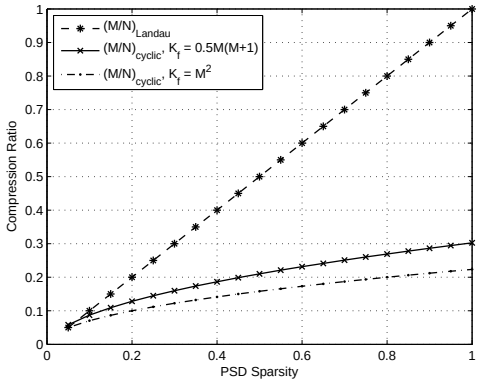

(a) Minimum Sampling Rates for Energy detection vs. Cyclostationary Detection at High SNRs

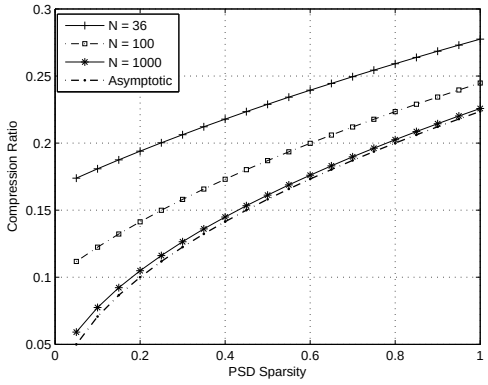

(b) Minimum Sampling Rates for Cyclostationary Detection, for $K_f = M^2$ at low SNRs (0 dB) for increasing values of N.

Figure 6.3: Minimum Sampling rate vs PSD Sparsity

fore non-sparse, one cannot sample below the Nyquist rate. However, exploiting the 2D sparsity in f and α, we can go as low as $M/N = 0.23$ for $K_f = M^2$, giving about 80% lower sampling rates. For $K_f = M(M+1)/2$, we get a gain in compression ratios of about 70% compared to the Landau rate.

In Fig. 6.3(b), we study the minimum acheivable sampling rates at a low SNR of 0 dB. In this scenario, with only PSD sparsity, we cannot sample lower than the Nyquist rate irrespective of the actual number of signals present in the band of interest as the PSD is not sparse due to high noise power. However, we can exploit the sparsity in the cyclic frequency domain to sample lower than the Nyquist rate. Fig. 6.3(b) shows that at low SNRs, with increasing N, the minimum sampling rates for Cyclostationary detectors converges with the rates achievable at high SNRs, which acts as a lower bound for the case when $K_f = M^2$. But for moderate values of N, for instance $N = 36$, we need about 10% higher sampling rates compared to the lower bound. Hence, there exists a tradeoff between the minimum lossless sampling rate and the reconstruction computational complexity which is also governed by N. In fact, the lower bound on the minimum sampling rate can only be achieved as N grows, which entails additional computational complexity during reconstruction.

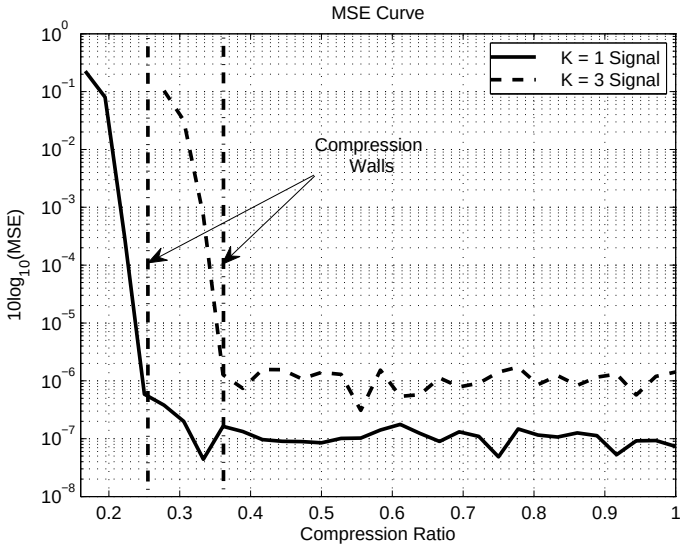

Figure 6.4: Minimum Squared Error(MSE) of Reconstructed Feature used for Signal Detection under Varying Sparsity Levels, $K = 1$ and $K = 3$ Signals.

6.5.2 SCF Reconstruction Mean Squared Error (MSE)

In this section, we consider noiseless signals, all of the same signal energy, and compute the mean squared error (MSE) of the cyclic feature used for detection at a compression ratio M/N with respect to its energy under no compression denoted by $\mathbf{s}_{x_i}$. We define the MSE as

$$\text{MSE} = \mathbb{E}\left[|\hat{s}_{x_i} - s_{x_i}|^2/|s_{x_i}|^2\right].$$

where $\hat{s}_{x_i}$ is the cyclic feature used for detection. We use the reconstruction algorithm with high L (of the order of 1×10^4) to ensure that the reconstructed $\hat{\mathbf{s}}_x$ is sparse with K_f non-zero spectral peaks, and show the loss in reconstructed cyclic feature with decreasing compression ratio. Fig. 6.4 shows the MSE versus compression ratio M/N for the channel populated with $K = 1$ and 3 signals, yielding a PSD occupancy of 5% and 15% respectively. The MSE curves show that there is no loss in spectral correlation peak energy up to a certain threshold compression ratio, below which the MSE starts increasing. Therefore, when $\hat{\mathbf{s}}_x$ is truly sparse (with sufficient L), the sampling rate can be reduced up to a certain

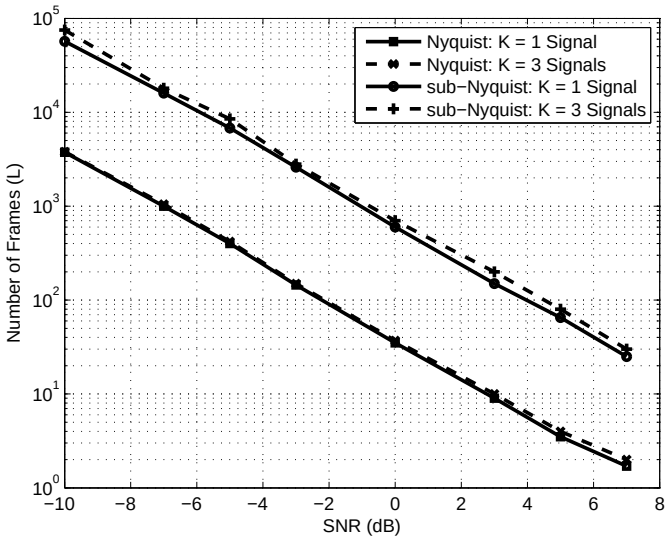

Figure 6.5: Number of frames(L) required to reach $(P_{fa}, P_d) = (0.1, 0.9)$ versus SNR for Nyquist and sub-Nyquist based detectors for a Compression Ratio of $M/N = 0.5$, with $K = 1$ and 3 Signals.

threshold with no loss incurred, a point that we refer to as *compression wall*. All compression ratios above this threshold yield a lossless reconstruction. Fig. 6.4 shows this trend for different spectral occupancies, and the vertical lines point to the location of the corresponding *compression walls*. Note that the minimum lossless compression ratios obtained numerically in Fig. 6.4 are higher than the theoretical bounds computed using Eq. (6.19). This is due to using a low frame length N, and as a result a small FFT size which results in the features leaking into other SCF bins, resulting in an effective number of non-zero features greater than (6.10).

6.5.3 Sensing Time Requirements and Comparison to Nyquist Detection

At relatively low SNRs below 10 dB, the noise starts to degrade the reconstruction of the SCF. In this section, we quantify the additional sensing time required to reach a given $(P_{fa}, P_d) = (0.1, 0.9)$ at various SNRs and compression ratios using our reduced-complexity detector.

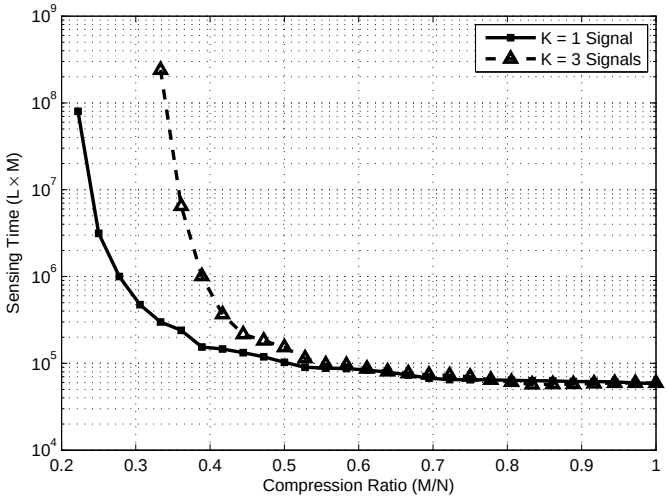

Figure 6.6: Sensing Time versus Compression Ratio to reach $(P_{fa}, P_d) = (0.1, 0.9)$ for Varying Sparsity Levels, $K = 1$ and 3 Signals and SNR = -5 dB.

We start by comparing the sensing time (number of frames L) required for both Nyquist and sub-Nyquist based detectors for varying SNR and sparsity levels. Fig. 6.5 compares the Nyquist-based sensing time as a function of SNR to the required sensing time of sub-Nyquist based detector with compression ratio $M/N = 0.5$ with a channel populated with $K = 1$ and 3 signals. The result shows that the sub-Nyquist detection using our algorithm maintains the same relationship between the sensing time and SNR as the Nyquist detection. The slope of the sub-Nyquist curve is equal to that of the Nyquist detector showing that the reconstruction conserves the linear relationship (in dB scale) between SNR and sensing time for cyclostationary detectors.

Fig. 6.6 shows the trend of total number of samples/sensing time $(L \times M)$ versus the compression ratio under a fixed sparsity of $K = 1$ and 3 signals at SNR $= -5$ dB. As expected, the minimum lossless compression ratio $(M/N)_{min}$ for the given sparsity is reached at about a compression ratio of 0.3 and 0.4 respectively as was also shown in the MSE plot in Fig. 6.4. With decreasing compression ratio, there is a steady but slight increase in the required sensing time up to the compression wall. The slight increase in required sensing time is

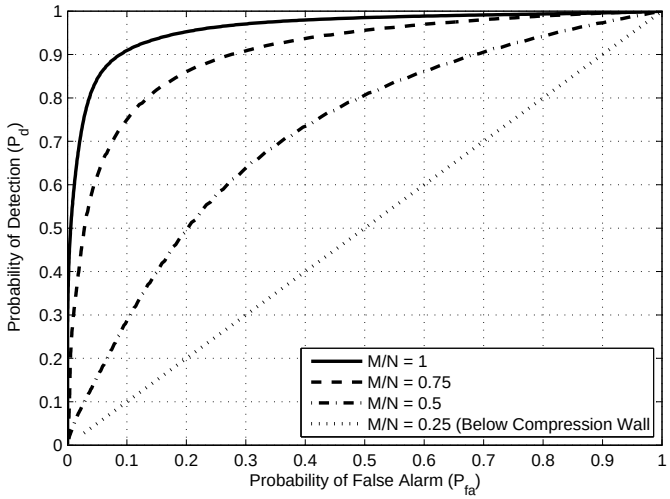

Figure 6.7: P_d versus P_{fa} for Varying Compression Ratio($\frac{M}{N}$) for $K = 3$ Signals, Number of Frame Averages L = 15000 and SNR = -10 dB.

a direct result of the noise being present, and therefore additional sensing time is required to make the SCF have only K_f features. However, operating at a compression ratio below the compression wall requires an exponentially increasing number of samples ($L \times M$) in order to operate at the same point on the ROC, which makes the detection infeasible within a constrained sensing time. This explains the tradeoff between the sensing time and reduction in sampling rates where being close to the compression wall is the optimum point to be at since the maximum savings in terms of sampling rates can be achieved with only a linear increase in sensing time.

6.5.4 Detection Performance Comparison

In this section we analyze the detection performance of the proposed algorithm (6.13) for varying parameters. Firstly, we show the effect of varying the compression ratio under a fixed SNR $= -10$dB and $L = 15000$ averages for a fixed sparsity of 15% ($K = 3$ signals). Fig. 6.7 shows that decreasing the sampling rate does actually result in a gradual decay in detection performance. The reason behind this is that number of averages L are not enough to ensure the the

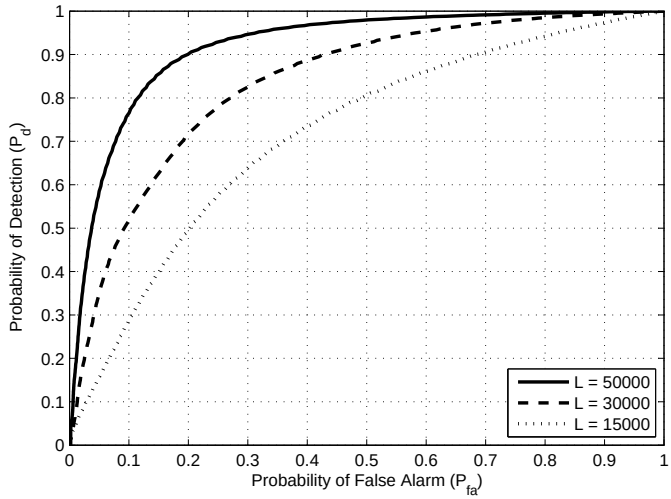

Figure 6.8: P_d versus P_{fa} for Varying Frame Averages for $K = 3$ Signals, Compression Ratio M/N = 0.5 and SNR = -10 dB.

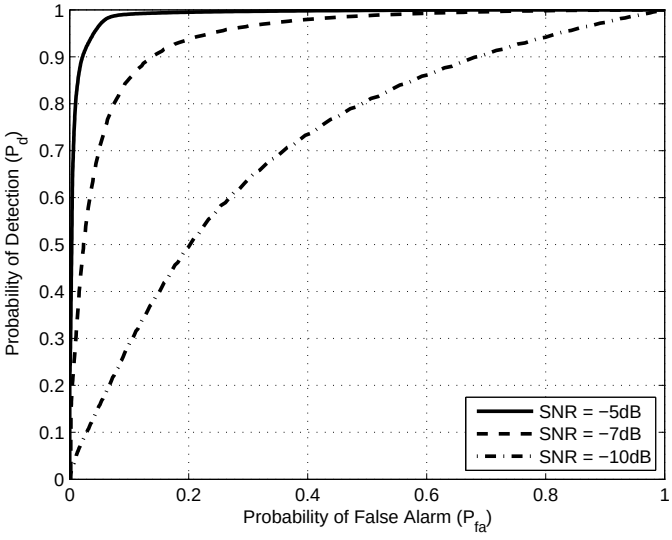

Figure 6.9: P_d versus P_{fa} for Varying SNR for $K = 3$ Signals, Compression Ratio M/N = 0.5 and Number of Frame Averages L = 15000.

noise exhibits no significant cyclic features at a SNR of -10 dB. As a result, taking into account only K_f spectral peaks according to Eq. (6.19) is not sufficient. Under enough averages, the MSE curve has shown that the reconstruction is lossless until the bound, and therefore the ROC curves will match with increasing L. The detection performance at sampling rates below the compression wall worsens

drastically giving a linear relationship between P_d and P_{fa}.

The presence of unwanted cyclic features at low SNRs in the reconstructed SCF can be compensated by increasing the number of frame averages L needed to compute the vectorized auto-correlation matrix $\mathbf{r}_z$. Fig. 6.8 shows the improvement in detection performance with increasing number of averages for fixed SNR $= -10$dB, compression ratio $M/N = 0.5$ and $K = 3$ signals. The detection performance improves with increasing L as this corresponds to additional sensing time and also as the sparsity of the reconstructed SCF converges to its true sparsity.

Finally, we show the impact of varying SNR on detection performance for fixed $L = 15000$, compression ratio $M/N = 0.5$ and $K = 3$ signals. From Fig. 6.9 we can see that the detection performance improves with increasing SNR as 1) the signal power increases and 2) with increasing SNR the reconstructed SCF approaches the true sparsity. In fact, increasing SNR is equivalent to increasing the number of samples used for averaging the SCF, and the trend is similar to the ROC curves presented in Fig. 6.8.

6.6 Summary

We have presented in this chapter a compressive sampling approach for wideband spectrum sensing using cyclostationary detection which directly reconstructs the test statistic used for cyclostationary detection without reconstructing the time-domain signal. The resulting measurement matrix is shown to satisfy the RIP property with high probability, ensuring the stability of the reconstruction algorithm. Further, bounds on the minimum compression ratio are theoretically derived that ensure the uniqueness of the reconstructed statistic with high probability. The resulting compression bound is then compared to the theoretical Landau rate for energy detection, and gains between 73% and 83% in sampling rates are shown to be achieved under the proposed detector using moderate frame

length, and hence without incurring high computational complexity. With respect to the detection performance resulting from the unique stable reconstruction, the relationship between SNR and sensing time remains linear on a logarithmic scale as for Nyquist detectors. Finally, it was shown that under the minimum compression ratio, the reconstruction becomes non-unique, which results in detection performance loss which could be made up for with exponentially increasing sensing time.

CHAPTER 7

Spectrum Sensing and Modulation Classification in Fading Environments

We investigate in this chapter the impact of fading on both spectrum sensing and the blind modulation classification algorithms presented in Chapter 4. As was discussed in Chapter 2 and 4, signal detection needs to be performed using energy detection. As a result, we analyze the impact of fading on energy detection, and then study the performance of the classification algorithms in Chapter 4 under multipath environments.

We quantify in Section 7.1 the effect of fading in the performance of energy detection in various communication scenarios. Then, Section 7.2 investigates the additional energy consumption required to meet the classification accuracy of 95% under realistic multipath environments.

7.1 Energy Detection-Based Spectrum Sensing over $\kappa - \mu$ Fading Channels

This section investigates the performance of an energy detector over the generalized $\kappa-\mu$ [Yac07] fading channels which have been shown to provide remarkably accurate fading characterization. As expected, the performance of the detector is highly dependent upon the severity of fading since even small variation of the fading conditions affect significantly the value of the average probability of detection. The results presented are particularly useful in assessing the effect of fading

in energy detection-based cognitive radio communication systems and therefore they can be used in quantifying the associated trade-offs between sensing performance and energy efficiency in cognitive radio networks.

The authors in [DAS07] derived closed-form expressions for the average probability of detection over Rayleigh, Rice and Nakagami fading channels for both single-channel and multi-channel scenarios. Likewise, the energy detection performance in the case of equal gain combining and Nakagami-m multipath fading has been investigated in [HR] whereas the corresponding performance in collaborative spectrum sensing and in relay-based cognitive radio networks has been evaluated in [ATJ, ATJ11a]. A novel semi-analytic method for analyzing the performance of energy detection of unknown deterministic signals was reported in [HRT11]. This important work is based on the moment-generating function (MGF) method and aims to overcome the analytical difficulties that arise from the presence of the Marcum Q-function. This method was utilized in the case of maximal-ratio combining (MRC) in the presence of Rayleigh, Rice and Nakagami-m fading in [HRT11] as well as for the useful case of correlated Rayleigh and Rician fading channels in [HB11]. Finally, the detection of unknown signals in low signal-to-noise-ratio (SNR) over K-distributed (K), generalized K (K_G) and the very flexible $\eta-\mu$ fading channels has been recently analyzed in [ATJ11b, RKJ09].

The $\kappa-\mu$ distribution is a generalized fading model that is distinctive for providing adequate characterization of multipath fading particularly for line-of-sight (LOS) communication scenarios. It was reported in [Yac07] along with the $\eta-\mu$ fading model which accounts for non-line-of-sight (NLOS) communication conditions. The $\kappa-\mu$ fading model has been shown to be particularly flexible and it includes as special cases the well known Rice, Nakagami-m, Rayleigh and one-sided Gaussian distributions [Yac07]. The $\kappa-\mu$ fading model has been shown to represent effectively the small-scale variations of a fading signal in LOS communications. Physically, this fading model considers a signal composed of clusters of multipath waves propagating in a non-homogeneous environment.

Within any one cluster, the phases of the scattered waves are random and have similar delay times with delay-time spreads of different clusters being relatively large. The clusters of multipath waves are assumed to have scattered waves with identical powers while each cluster consists of a dominant component with arbitrary power. To this effect, the parameters μ and κ correspond to the number of multipath clusters and the ratio between the total power of the dominant components and the total power of the scattered waves, respectively. These two parameters render this fading model remarkably flexible as its capturing range is particularly broad [Yac07, Fig. 9]. This is also evident by the fact that the widely known Rice and Nakagami-m fading models are included as special cases for $\mu = 1$ and $\kappa = 0$, respectively [Yac07]. Therefore, this model can provide a meaningful insight on how fading affects the performance of an energy detector which ultimately leads to a significant improvement on the design of cognitive radio systems in terms of energy efficiency and cost.

As mentioned in Chapter 2, energy detection is used in blind scenarios for signal detection. As such, the wideband received signal is first filtered, and its energy is computed over a fixed time interval as given by (2.2). Closed form expressions for the detection probability as a function of the fading environment variables and number of collaborating users can be found in [SRZ13].

7.1.1 Numerical Results

This section is devoted to the analysis of the behavior of energy detection in $\kappa-\mu$ fading channels. The corresponding performance is evaluated for different scenarios of interest through both $\overline{P}_d$ versus the average SNR $\overline{\gamma}$ curves and complementary receiver operating characteristics (ROC) curves (P_m versus P_f). In addition, the effect of the fading parameters κ, μ and m on the value of P_d is numerically quantified.

Fig. 7.1.1 demonstrates $\overline{P}_d$ vs $\overline{\gamma}$ curves for $\kappa-\mu$ fading for different κ and

μ values with $P_f = 0.1$ and $u = 2$. One can observe that the energy detector performs better as κ and μ increase due to the higher dominance of the LOS component and the relative advantage of the multipath effect, respectively. For example, for the case of $\overline{\gamma} = 15\,\text{dB}$ and $\kappa = 1.0$ (fixed), the $\overline{P}_d$ for $\mu = 0.7$ is nearly 10% higher than for $\mu = 0.5$. In the same context, when $\mu = 0.7$ (fixed), the $\overline{P}_d$ for $\kappa = 3.0$ is 9% higher than for the case of $\kappa = 1.0$.

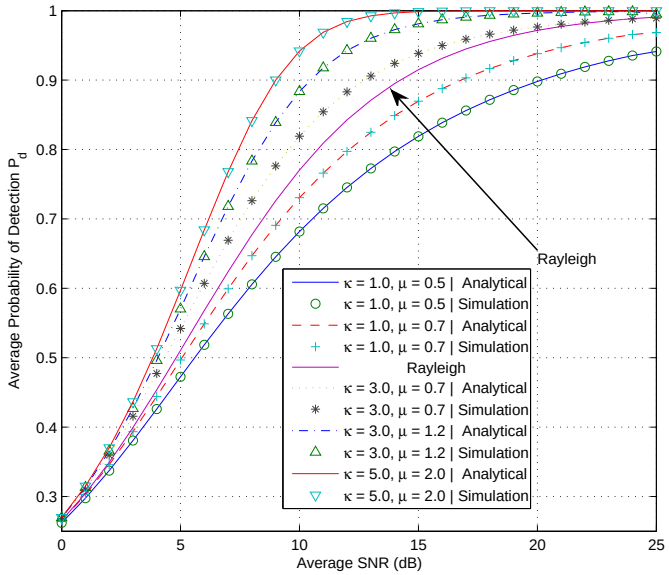

Figure 7.1: $\overline{P}_d$ vs $\overline{\gamma}$ for i.i.d κ–μ fading with $P_f = 0.1$, $u = 2$ and different values for κ and μ.

As the value of $\overline{\gamma}$ decreases to negative values, the effect of varying κ and μ is shown to decrease. Fig. 7.1.1 illustrates the complementary ROC for energy detection with up to eight collaborating users. The fading scenarios considered are the same as in the previous case while the average SNR is set to $\overline{\gamma} = 3\,\text{dB}$. As expected, the performance of the energy detector improves substantially as the number of users increases.

It is also important to quantify the effect of the fading parameters on the system performance. Although it is undoubtedly elucidating to carry out this task analytically, this is unfortunately impossible due to the high algebraic in-

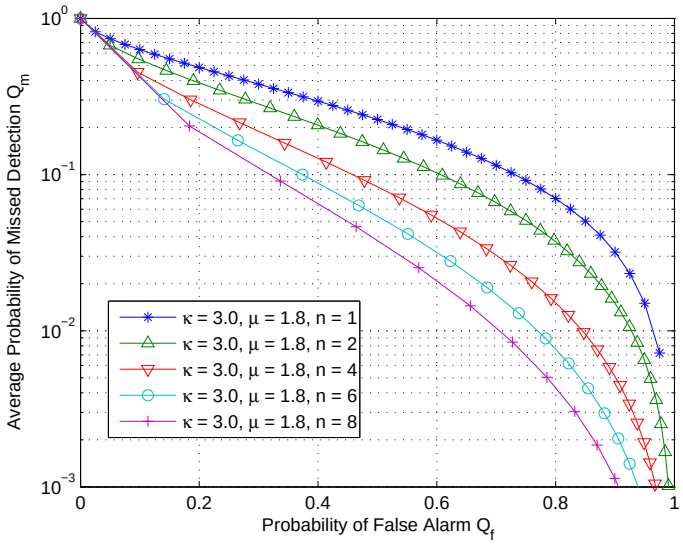

Figure 7.2: Complementary ROC curves for $\kappa-\mu$ fading with $u = 2$, $\kappa = 3$, $\mu = 1.8$, $\overline{\gamma} = 3\,\text{dB}$ and n collaborating users.

tractability of the involved mathematical representations. As a result, this effect is only analyzed numerically. To this end, Fig. 7.1.1 depicts the behaviour of $\overline{P}_d$ versus κ for $P_f = 0.1$, $u = 3$, $\mu = 0.2$ and different values of $\overline{\gamma}$. One can observe the significant deviation of the $\overline{P}_d$ even for small variations of κ and/or $\overline{\gamma}$. For example, for $\gamma = 13\,\text{dB}$, it is shown that $\overline{P}_d = 0.55$ and $\overline{P}_d = 0.675$ for $\kappa = 1$ and $\kappa = 4$, respectively. Furthermore, for $\kappa = 8$, $\overline{P}_d = 0.47$ for $\overline{\gamma} = 5\,\text{dB}$ and $\overline{P}_d = 0.67$ for $\overline{\gamma} = 9\,\text{dB}$. Likewise, the behavior of $\overline{P}_d$ versus μ is illustrated in Fig. 7.1.1 for $P_f = 0.1$, $u = 3$, $\kappa = 2.0$ and different values of $\overline{\gamma}$. Clearly, for $\overline{\gamma} = 10\,\text{dB}$, it is shown that $\overline{P}_d = 0.52$ and $\overline{P}_d = 0.815$ for $\mu = 0.2$ and $\mu = 1.0$, respectively. Also, for $\mu = 0.8$, one obtains $\overline{P}_d = 0.55$ for $\overline{\gamma} = 6\,\text{dB}$ and $\overline{P}_d = 0.88$ for $\overline{\gamma} = 13\,\text{dB}$.

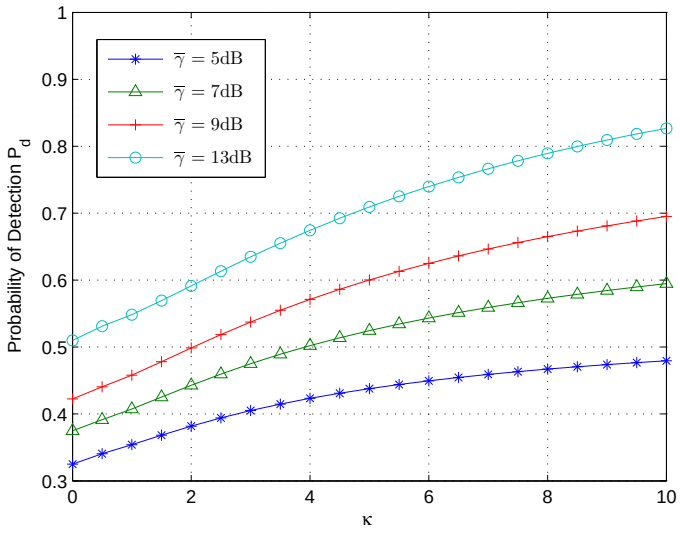

Figure 7.3: $\overline{P}_d$ vs κ for $\kappa-\mu$ fading with $P_f = 0.1$, $u = 3$, $\mu = 0.2$ and different values of $\overline{\gamma}$.

7.2 Blind Signal Classification in the Multipath Environments

In this section, we analyze the impact of fading on the classification algorithms. Given that flat fading would essentially result in a loss in SNR, the modulation classifier presented in Chapter 4 would correctly classify the incoming signals when the signal meets the design specifications given in Table 4.1. For this reason, we dedicate this section to studying the impact of frequency selective fading on the classification performance of the proposed processor.

In typical communication receivers, frequency selective multipath fading is dealt with by means of equalization. Typically, the transmitter and receiver agree on a sequence of information symbols referred to as a training sequence which is used to estimate the frequency selective channel. As such, this training sequence is repeated every coherence time in order to keep track of the temporal variations of the channel.

However, channel estimation and equalization can be performed without any

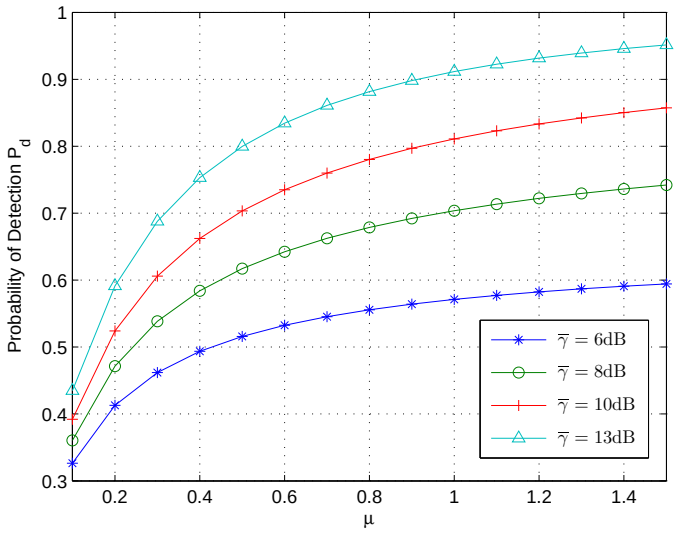

Figure 7.4: $\overline{P}_d$ vs μ for $\kappa-\mu$ fading with $P_f = 0.1$, $u = 3$, $\kappa = 2.0$ and different values of $\overline{\gamma}$.

training sequences. This method is referred to as blind equalization, whereas the receiver estimates the channel without having the transmitter transmit any known training sequence. However, blind equalization is performed by exploiting some known statistical property of the received signal. Most commonly used blind equalizers are the Constant Modulus Algorithm (CMA) [KS98,TA83,JSE98], and the Alphabet Matched Algorithm (AMA) [BC06]. However, estimating the channel blindly without knowledge of the modulation type or order of the received signal is a challenging task because the cost function being minimized by the adaptive filter is unknown as it is dependent on the modulation of the incoming signal. For this reason, the conventional blind channel equalizers cannot be applied in our setting when the receiver's goal is to classify the incoming signal.

After estimating the received signal parameters such as frequency and timing information, the transceivers can be properly synchronized and the information symbols can be extracted. Once the symbols are extracted, AMA algorithms such as the one presented in [SBS00] can be used for modulation classification. Intuitively, the receiver performs multiple blind channel equalizations based on

each of the hypotheses. The hypothesis with the smallest cost function is then decided as the modulation of the received signal. Note that since the cost function of AMA algorithms operates on information symbols, blind modulation classification can only be performed once the symbols have been extracted. For this reason, we propose algorithmic methods to improve the classification probability of the proposed processor in Chapter 4 without estimating the channel. Once the modulation type has been identified, we use blind equalization techniques to determine the modulation level of the received signal.

7.2.1 Considered Channel Models

In order to evaluate the performance of our proposed algorithms in multipath environments, we have adopted practical channel models obtained from the LTE standard, and have tested our classification algorithms under these standardized channels. The three channels that we have considered are the 1) Extended Pedestrian A model (EPA), 2) Extended Vehicular A Model (EVA), and 3) Extended Typical Urban model (ETU) [Cha97, Cha07]. The delay spread of these three channels are 410 ns, 2.5 μs, and 5 μs respectively, and therefore range from the least to the most severe multipath channels. The power-delay profiles of each of the three considered channels are given below in Fig. 7.8 where R is the total number of rays for each of the channel models, and where (a_i, τ_i) denote the power of the ray i at delay τ_i. Given the signal bandwidth BW, the total number of resolved rays is given by $L = \lceil \text{BW} \times \text{rms delay spread} \rceil$. As a result, the power of each of the resolved paths is obtained by interpolating the power-delay profile as follows

$$P[l] = \sum_{n=0}^{R-1} a_n |sinc(l - \tau_n \text{BW})|, \forall l \in [0, ..., L-1]. \tag{7.1}$$

Each of the channel taps are assumed to follow a Rayleigh distribution, and are therefore generated as following $h[l] = CN \sim (0, P[l])$, and the received signal is

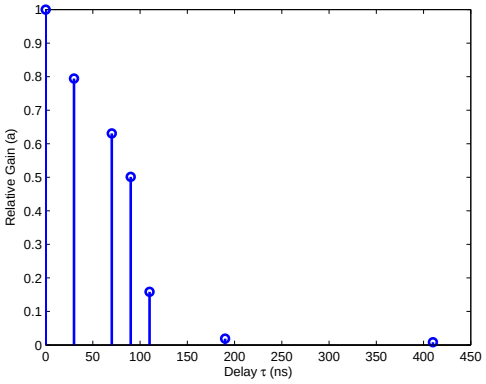

Figure 7.5: EPA Channel Power-Delay Profile

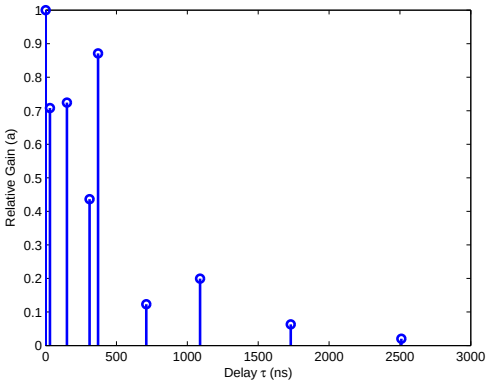

Figure 7.6: EVA Channel Power-Delay Profile

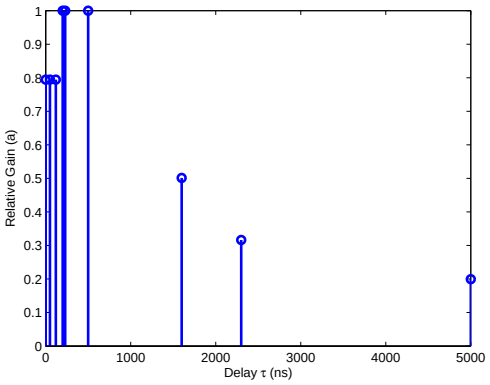

Figure 7.7: ETU Channel Power-Delay Profile

Figure 7.8: Delay-power profiles of different channel models considered in the LTE standard.

given by

$$y[n] = \sum_{l=0}^{L-1} h[l]x[n-l] + w[n], \tag{7.2}$$

where $x[n]$ is the transmitted signal, and where $w[n]$ is the AWGN. Multipath fading introduces Inter-Symbol Interference (ISI) whenever 1/BW $<$ rms delay spread.

Multipath fading is typically dealt with by estimating the channel and inverting its effect. Channel estimation can be performed by means of a training sequence, or by exploiting the knowledge of a statistical property of the received signal also known as blind equalization. Both kinds of equalization require knowledge of the carrier frequency and symbol rate of the received signal. Once acquired, frequency offset estimation (due to Doppler or frequency mismatch) and timing synchronization are performed on a known preamble. When a training sequence is utilized, the symbols are first extracted and the channel is estimated using an MMSE, zero-forcing, LMS, or RLS (among others) equalizer. When that is not the case, a modulation-dependent cost function is minimized in order to estimate the channel.

The challenge in *blind* modulation classification is that 1) fine timing and frequency estimation is not available in the first few processing blocks, and 2) blind equalization does not work since the modulation type (and therefore the cost function of the adaptive filter) is unknown. As a result, we resort to making our classifiers robust to multipath fading, until enough information about the received signal is gathered to perform blind equalization.

We show in Fig. 7.9 the modified hierarchical modulation classification tree, where the highlighted blocks are the ones that need to be modified in order to meet the required classification accuracy. Note that once timing, frequency, and symbol extraction is performed, blind equalization can be performed for each of the possible modulation levels, and the modulation level can be estimation

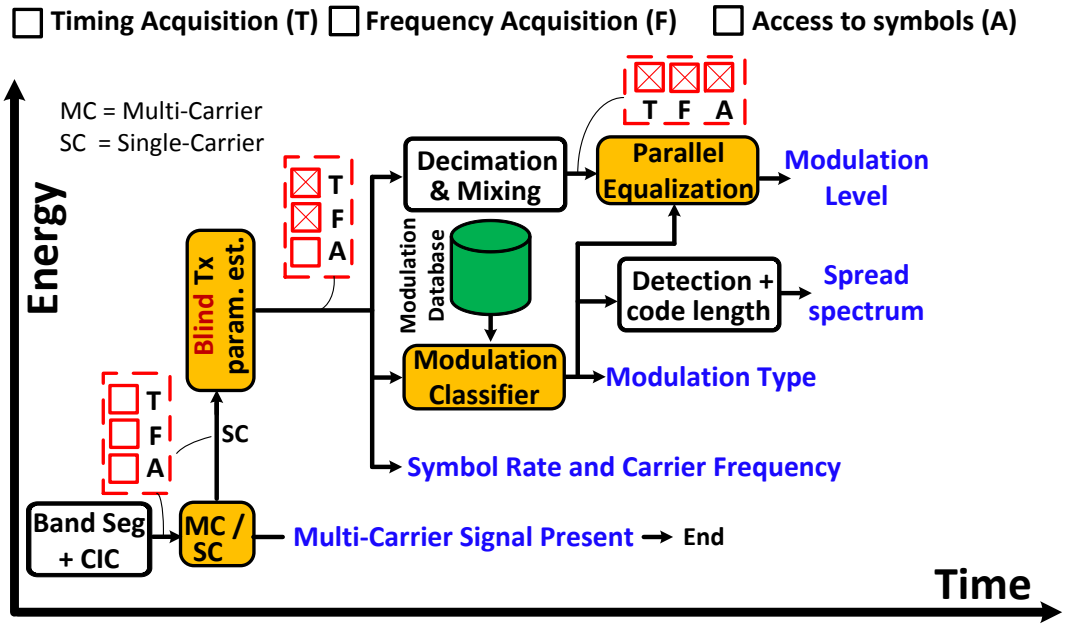

Figure 7.9: Hierarchal modulation classifier with the required information for blind equalization checked at each stage.

based on the smallest cost function. This will be further expanded on at the end of this section. With respect to computing the total consumed energy, the chip implemented in [RYU13] consumes 20pJ/cycle, and that number is used to compute the consumed energy of all processing kernels.

7.2.2 Multi-Carrier vs Single-Carrier Classification

As shown in the top-level diagram of the proposed classifier in 7.9, the first processing block is the single vs multi-carrier classifier based on the C_{42} test statistic computed as shown in [RYU13]. Table 7.1 shows the mean of the C_{42} statistic for different modulation types and orders.

Since this step is crucial for further classification tasks, we focus on the worst case scenario, which is the classification of 64-QAM signals vs OFDM signals. Since the test statistic C_{42} measures the Gaussianity of the received signal, it is expected that passing a SC signal through a multipath fading channel will

Table 7.1: Mean of C_{42} statistic for different modulation types and orders

Modulation	$\mathbb{E}[C_{42}]$
BPSK	-2.0
4-PAM	-1.36
PSK	-1.0
16-QAM	-0.68
64-QAM	-0.6191
OFDM	0

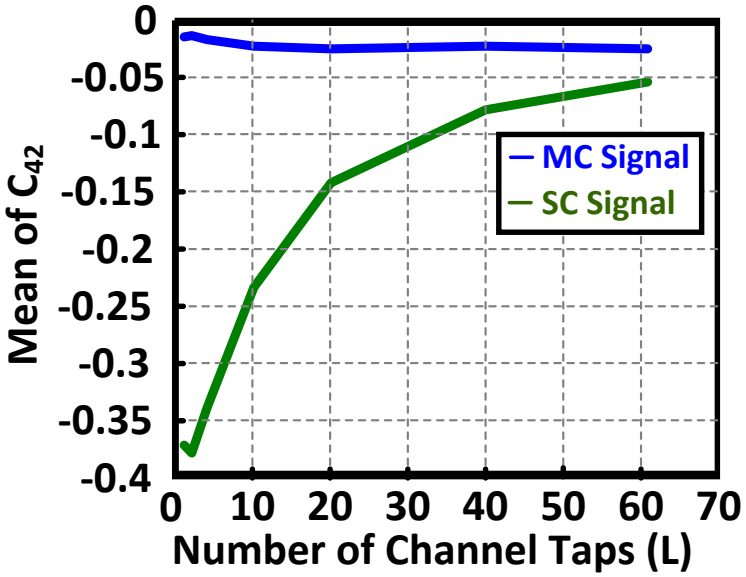

Figure 7.10: Mean of the C_{42} statistic as a function of the number of channel taps.

increase its Gaussianity, resulting in a loss in classification performance. Fig. 7.10 shows the impact of channel taps on the $\mathbb{E}[C_{42}]$, where the channel $h[\cdot]$ follows the ETU channel model.

As can be seen in Fig. 7.10, the distance between the asymptotic values of the C_{42} test statistic for 64-QAM signals and OFDM signals gets closer with increasing number of taps. We consider in all the results 20 MHz signals, resulting in $\lceil 20 \times 10^6 \tau_{spread} \rceil$, where τ_{spread} is the delay spread of the considered channel. We show results at an SNR of 10 dB, but report the energy increase of the proposed solution at both SNRs of 0 and 10 dB.

As shown in Fig. 7.11, 500 samples are enough to guarantee a classification

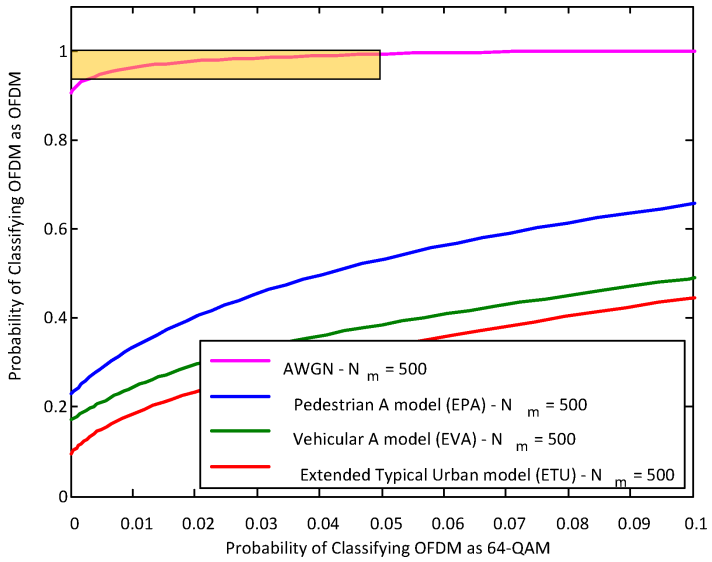

Figure 7.11: Performance of MC/SC classifier under varying multipath channels using a fixed number of samples $N_m = 500$ samples.

accuracy of 0.95 in AWGN. The yellow rectangle is the area in which we would like to operate to meet the specifications. We see that the classifier suffers a big loss in terms of its classification accuracy in all three of the considered multipath models. Since the ETU model is the most severe one as it has the higher rms relay spread, the performance of the MC/SC classifier is the worst under this multipath channel. As channel equalization is not possible at this stage since fine frequency/timing acquisition are not yet performed, we resort to increasing our sensing time N_m in order to reduce the variance of the test statistic C_{42}. We show in Fig. 7.12 the required sensing time increase in order to meet a classification accuracy of 95% under all three multipath models. We show that in order to meet the required classification accuracy, the sensing time needs to be increased by a factor 22x in the worst case scenario of ETU multipath fading. In terms of energy consumption, this increase in sensing time costs an additional 0.2 μJ under an SNR of 10 dB, and 4.8 μJ at an SNR of 0 dB.

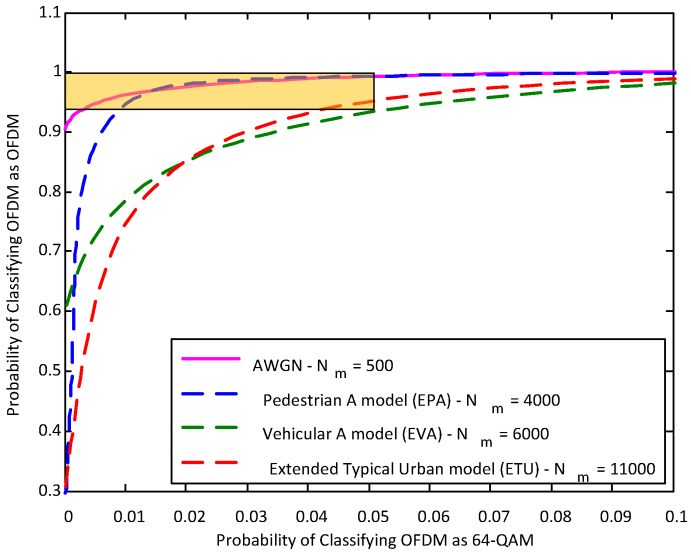

Figure 7.12: Sensing time required for each of the channel models in order to meet the required classification accuracy.

7.2.3 Transmit Parameters Estimation and Modulation Type Classification

Since both the pre-processors and the modulation type classifier are based on detecting present cyclic features using the CAC, we focus our attention in this subsection on the impact of multipath channels on the CAC statistic. Given the multipath model in (7.2), the CAC of $y[\cdot]$ is related to that of $x[\cdot]$ as follows

$$R_y^\alpha(\nu) = \sum_{\ell=0}^{L-1} h^2[\ell] R_x^\alpha(\nu) + \sum_{\ell=0}^{L-1} \sum_{u=0, u\neq\ell}^{L-1} h[\ell]h[\nu] R_x^\alpha(\nu+\ell-u), \tag{7.3}$$

$$R_{y^*}^\alpha(\nu) = \sum_{\ell=0}^{L-1} |h[\ell]|^2 R_{x^*}^\alpha(\nu) + \sum_{\ell=0}^{L-1} \sum_{u=0, u\neq\ell}^{L-1} h[\ell]h^*[\nu] R_{x*}^\alpha(\nu+\ell-u), \tag{7.4}$$

As a result, although we are interested in computing the CAC at lag $\nu = 0$, the CAC of $y[n]$ is a function of the CAC of $x[n]$ at non-zero lags, weighted by the unknown channel. As a result, the newly introduced term in (7.4) can be thought of as additional noise as it is an undesirable term, and its effect can be thought of as a loss in cyclic SNR. This behavior is shown in Fig. 7.13, where we

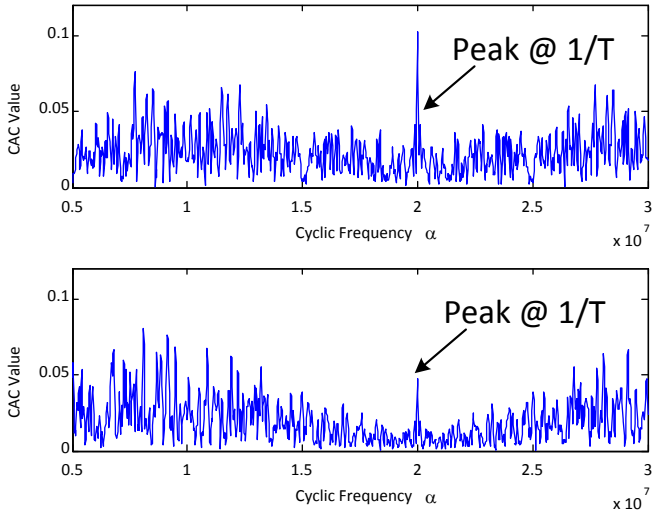

Figure 7.13: Impact of multipath fading on the CAC at different cyclic frequencies . Top figure corresponds to AWGN case, bottom figure corresponds to the multipath ETU channel.

demonstrate the impact of the ETU multipath fading on estimating the symbol rate of the received signal.

As can be seen, the feature at $\alpha = 1/T$ is no longer the strongest feature under multipath fading, and therefore increasing the sensing time for estimating the CAC is required in order to boost the cyclic SNR. As we have previously shown, the modulation type classification cannot meet the required accuracy if the symbol rate / carrier frequency offsets are above a certain threshold. For instance, the symbol rate estimate cannot be more than 1000 ppm away from the true symbol rate at an SNR of 10 dB, and more than 100 ppm at SNR of 0 dB. As a result, we measure the probability that the symbol rate estimate is within these bounds. Fig. 7.14 shows the required number of samples required in estimating the CAC within the search window in order to meet the probability of estimating the symbol rate within 1000 ppm from the true symbol rate.

Under just AWGN, $N_T = 320$ samples are enough to estimate the symbol rate and meet the maximum offset requirement. As shown in Fig. 7.14, the sensing

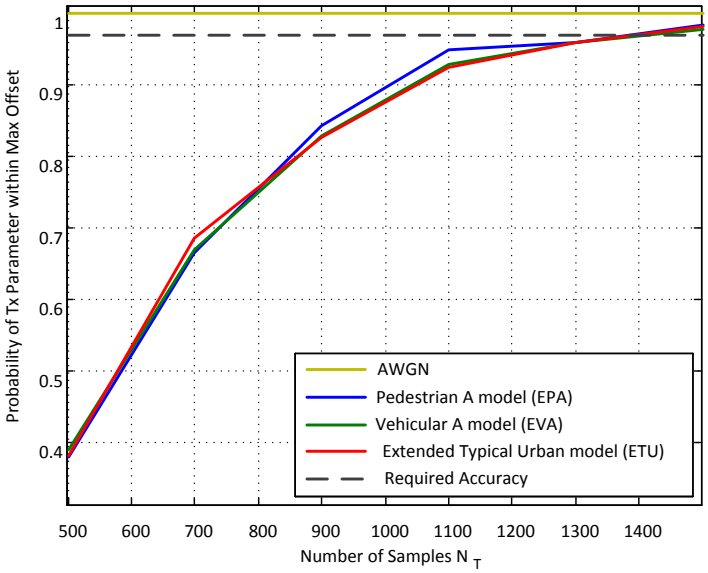

Figure 7.14: Probability of estimating the symbol rate within 1000 ppm from true symbol rate vs number of samples for AWGN and the 3 considered multipath channels.

time of the pre-processors needs to be increased by a factor of 4x in order to meet the required accuracy under all three multipath models. This results holds as well for estimating the carrier frequency. As a result, the cost of increasing the sensing time costs an additional 6.9 μJ and 59 μJ at SNRs of 10 and 0 dB respectively for the symbol rate estimation.

As for the modulation type classification, we summarize in Table 7.2 the present cyclic features of SC signals, along with the asymptotic normalized feature vector F. Similarly to estimating the symbol rate and carrier frequency, as the variance of the CAC increases under multipath fading, the number of samples needed to estimate the feature vector $\mathbf{F}$ used for modulation type classification need to be increased.

Note that when a given signal has a unique cyclic feature associated with it, it is therefore easier to differentiate it from other signals. M-QAM and M-PSK signals only have a single feature that is shared among the rest of the signals, and the feature at $\alpha = 1/T$ is also to weakest in strength. As a result, M-

Table 7.2: Cyclic features of all considered SC signals and their respective normalized asymptotic feature vectors.

Modulation Type	Present Cyclic Features	Asymptotic Feature Vector
M-QAM, M-PSK	$\alpha = 1/T$	$\mathbf{F} = [1, 0, 0, 0, 0, 0]$
M-PAM	$\alpha = [1/T, 2f_c - 1/T, 2f_c, 2f_c + 1/T]$	$\mathbf{F} = [0.13, 0.13, 0, 0.97, 0, 0.13]$
GMSK	$\alpha = [1/T, 2f_c - 1/2T, 2f_c + 1/2T]$	$\mathbf{F} = [0.1, 0, 0.7, 0, 0.7]$

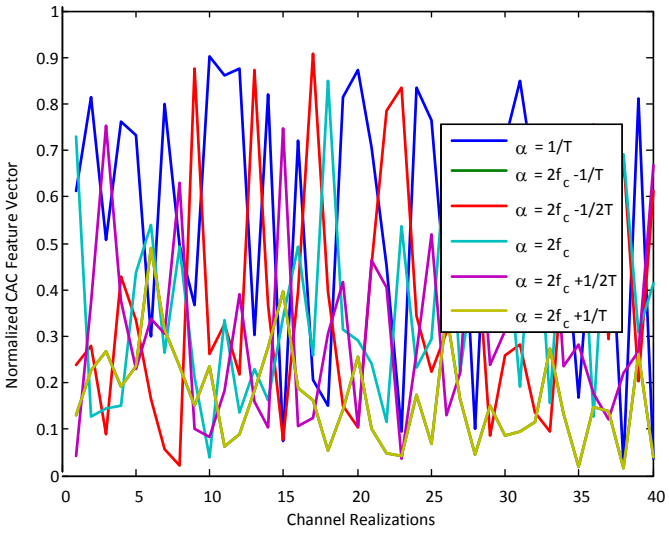

Figure 7.15: Feature vector of M-QAM/M-PSK signals at an SNR of 10 dB using 500 samples under the ETU multipath channel.

QAM/M-PSK signals are the hardest modulation type to classify. Fig. 7.15 shows the feature vector of M-QAM/M-PSK signals at an SNR of 10 dB using $N_c = 500$ samples, which is enough to classify M-QAM/M-PSK with a 95% accuracy in AWGN. Asymptotically, the feature vector converges to $[1, 0, 0, 0, 0, 0]$ as M-QAM/M-PSK signals only have one feature at their symbol rate. However, it is shown in Fig. 7.15 that the feature vector of M-QAM/M-PSK signals is nowhere close its asymptotic value as a result of the multipath.

Although the symbol rate and carrier frequency have been acquired at this stage and therefore symbol extraction can be performed, the number of hypothe-

ses to test at this stage using blind equalization is equal to 10 (4/8/16 PSK, 4/16/64 QAM, 2/4/8 PAM, and GMSK). Instead, we keep our hierarchal classifier that first estimates the modulation type before resorting to estimating the level using blind equalizers. As a result, we resort to increasing the sensing time to meet the required classification accuracy here as well. Fig. 7.16 shows the average feature vector of M-QAM/M-PSK and M-PAM signals versus number of samples used in estimating the CAC N_c, along with the average probability of correct classification.

As shown in Fig. 7.16, the feature vector of M-QAM signals converges to the asymptotic feature vector of [1, 0, 0, 0, 0, 0] with increasing number of samples N_c, and the probability of correct classification of QAM signals increases as well. Further, given that M-PAM signals have a unique feature at $\alpha = 2f_c$, their classification accuracy is not affected as much as M-QAM signals as shown on the right plot of Fig. 7.2.3. The classification accuracy of 95% is achieved with an increase of sensing time N_c of 2.2x, which costs an energy increase of 0.07 μJ at a SNR of 10 dB, and 0.29 μJ at an SNR of 0 dB.

Moreover, achieving the required classification accuracy can be achieved by means of collaboration of multiple sensors. It can be assumed that since multiple sensors will be far apart from one another, the channel observed by each of the sensors will be independent of each other. From (7.4), the impact of the multipath fading can be mitigated by collaboration among the users. In expectation, we get

$$\mathbb{E}[R^{\alpha}_{y^*}(\nu)] \rightarrow \sum_{\ell=0}^{L-1} \mathbb{E}\left[|h[\ell]|^2\right] R^{\alpha}_{x^*}(\nu) + \sum_{\ell=0}^{L-1} \sum_{u=0, u\neq\ell}^{L-1} \mathbb{E}\left[h[\ell]h^*[\nu]\right] R^{\alpha}_{x*}(\nu+\ell-u). \tag{7.5}$$

Note that the above expression utilized the fact that averaging the CAC of the noise of different users will converge to zero as the noise is uncorrelated across

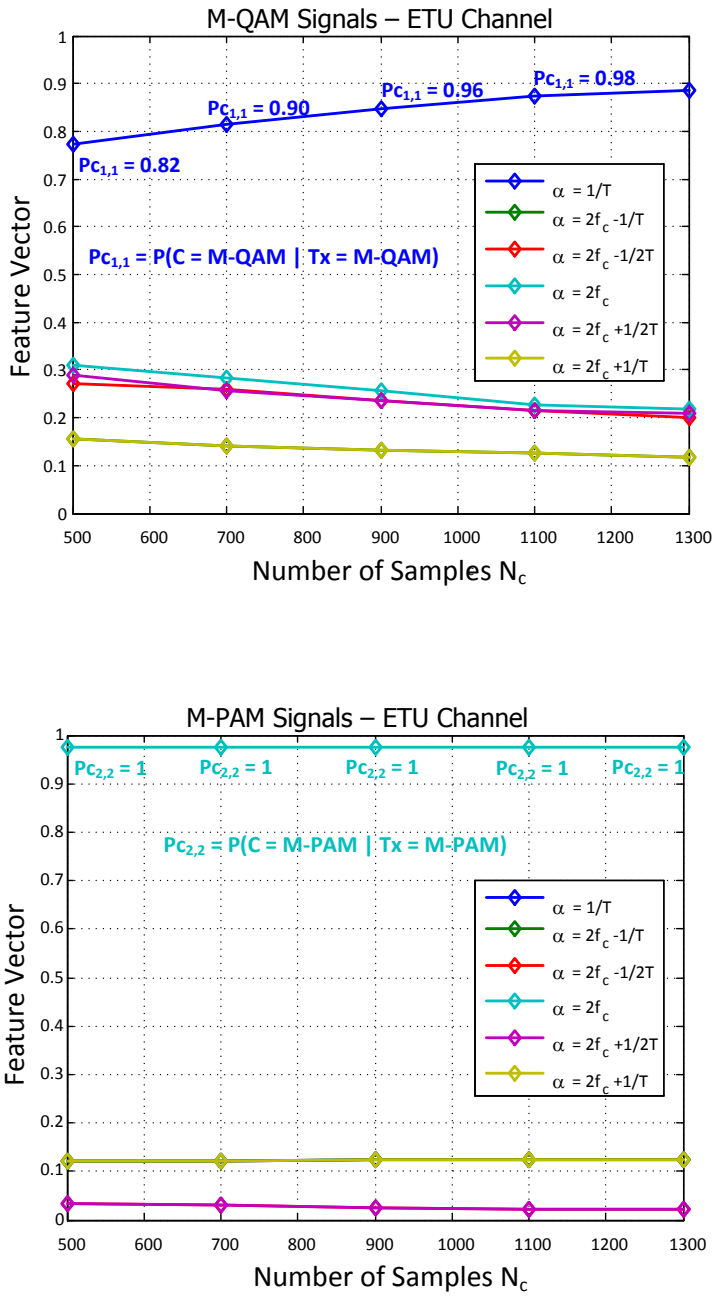

Figure 7.16: Average feature vector of M-QAM signals and M-PAM signals under ETU channels as a function of number of samples N_c at an SNR of 10 dB

users. Since different channel taps fade independently, then

$$\mathbb{E}[h[\ell]h^*[\nu]] = \mathbb{E}[h[\ell]] \times \mathbb{E}[h^*[\nu]] = 0,$$

since each of the channel taps have a zero mean. As a result, as the numbers of sensors tends to infinity, we obtain

$$\mathbb{E}\left[R^{\alpha}_{y^*}(\nu)\right] \rightarrow \sum_{\ell=0}^{L-1} \mathbb{E}\left[|h[\ell]|^2\right] R^{\alpha}_{x^*}(\nu), \tag{7.6}$$

where $\mathbb{E}[|h[\ell]|^2]$ reflects the average gain per tap. In effect, this solution results in removing the impact of the multipath channel on the CAC as the additional term converges to zero. Further, since noise among different sensors is uncorrelated, impact of noise has been reduced with collaboration, resulting in a boost in SNR without the additional need for increase in sensing time on each of the sensors.

7.2.4 Modulation Level Classification under Multipath Fading

Now that we have narrowed down the total number of classes to test in the level classification step, we resort to blind channel equalization techniques. In fact, using our previously proposed reduced complexity Kuiper classifier cannot be applied in multipath channels as it requires knowledge of the CDF for any given SNR. However, given that the CDF is a function of the channel realization itself, which is unknown, the level classifier would then fail. Instead, we look at conventional blind equalization techniques. For M-PSK modulations whose symbols lie on a circle, the Constant Modulus Algorithm (CMA) is typically adopted. We let $\mathbf{y}$ denote a vector of L demodulated symbols, and w be the channel estimate. The equalized symbols are therefore obtained by $z = \mathbf{w}^T\mathbf{y}$. The CMA algorithm minimizes the following cost function

$$\mathbb{E}_z[(|z|^2 - \gamma)^2], \text{where } \gamma = \frac{\mathbb{E}[|x|^4]}{\mathbb{E}[|x|^2]}. \tag{7.7}$$

However, it was shown that the CMA operating on complex symbols can result in a phase offset with respect to the ideal constellation, and we therefore implement the CMA using the real part of the demodulated symbols only z_r. The CMA update equation is therefore given by

$$w[i+1] = w[i] - \mu < 2(|z_r|^2 - \gamma)y^* z_r >_N, \tag{7.8}$$

where the $< \cdot >_N$ operation is the time averaging operation using N symbols.

Even when the received symbols do not satisfy the CMA criterion, CMA-based equalization can still result in a coarse estimate of the true channel $\mathbf{h}$. As a result, the CMA is used as an initial step to get a good coarse estimate of the true channel. Then, we resort to an Alphabet Matched Algorithm (AMA) that maps the received demodulated symbols to a set of known information symbols of cardinality M. The AMA cost function is given by

$$\mathbb{E}_z \left[1 - \sum_{i=1}^{M} e^{-\frac{|z-c(i)|^2}{2\sigma^2}} \right], \tag{7.9}$$

where $c(i)$ are the information symbols that we wish to map z to, and M is total number of symbols. When all symbols $\mathbf{z}$ lie on top of the symbols $\mathbf{c}$, the cost function tends to zero. The update equation is derived and is given by

$$w[i+1] = w[i] - \frac{\mu}{2\sigma^2} \sum_{i=1}^{M} < y^*(z - c(i)) e^{-\frac{|z-c(i)|^2}{2\sigma^2}} >_N . \tag{7.10}$$

The reason the AMA equalizer cannot be used without the CMA is because it requires a good channel estimate for the AMA algorithm to converge. For this reason, we adopt the following equalization strategy under the example of differentiating between 4/16/64 QAM. For $M \in [4, 16, 64]$, we 1) Run CMA under hypothesis H_M until cost function is below threshold or for a fixed number of iterations, 2) Switch to AMA equalizer to map symbols to constellation of size M. The hypothesis H_M with the lowest cost function is declared as the modulation

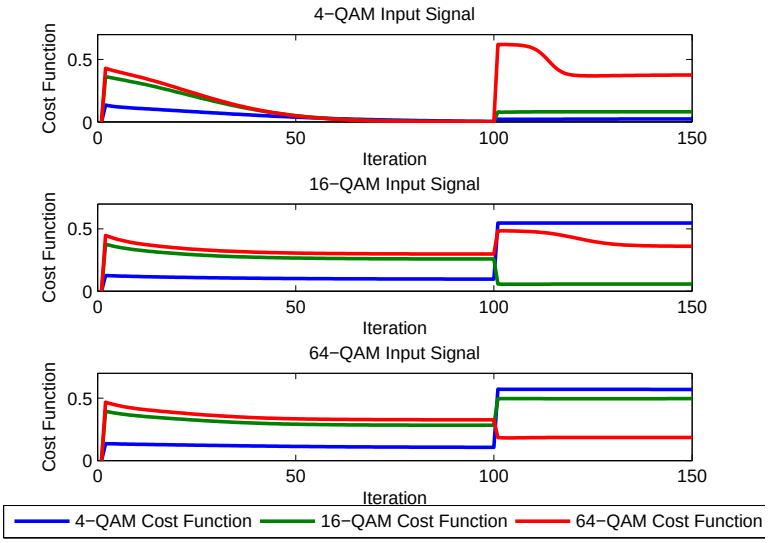

Figure 7.17: Evolution of the cost function with varying number of iterations when the input signal is 4, 16, and 64 QAM. Switch to AMA equalization is done after 100 CMA iterations.

level of the signal being classified.

Fig. 7.17 shows the evolution of the cost function following the algorithm described above. Once the CMA algorithm coarsely estimates the channel itself, the AMA equalizer kicks in. As shown in Fig. 7.17, the cost function of M-QAM is the smallest after the AMA equalization step when the input is M-QAM, for M being 4, 16, and 64.

As a result, this method shows that when a coarse estimate of the channel can be obtained through the CMA, the AMA can map symbols to their true symbols, and therefore symbol demodulation and modulation level classification can be performed. An example of the evolution of the equalized/demodulated symbols over different iterations is given in Fig. 7.18.

As was noted earlier, the AMA algorithm does not converge unless a good channel estimate is already obtained. However, the CMA equalizer performance worsens with decreasing SNR which degrades the classification performance. We give in Table 7.3 the classification accuracies of 4, 16 and 64 QAM as a function of the received SNR, in addition to the average classification accuracy where the

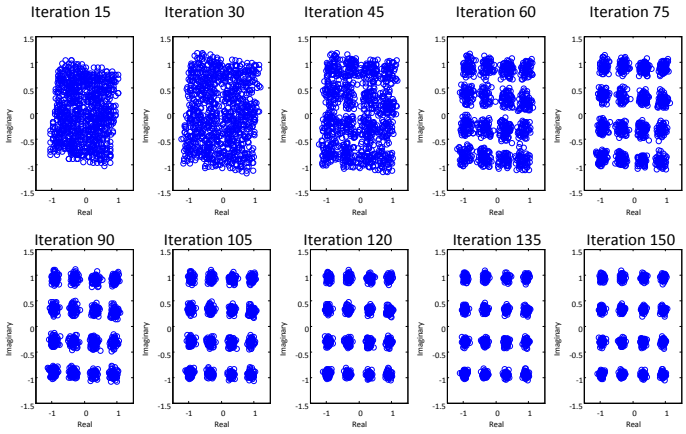

Figure 7.18: Demodulated/equalized symbols z as a function of iterations when the equalizer input is a 16-QAM signal.

Table 7.3: Average probability of level classification for various SNR levels when the signals are 20 MHz 4-16-64 QAM modulated passed through the ETU channel model.

SNR (dB)	10	12	14	16	18	20
P_c(4-QAM)	1	1	1	1	1	0.95
P_c(16-QAM)	1	1	0.9	0	0	0
P_c(64-QAM)	1	1	1	1	1	1
Average P_c	1	1	0.96	0.67	0.67	0.65

average is taken with respect to the classification of 4, 16, and 64 QAM signals. As can be seen, the average classificationa accuracy is degraded as a result of misclassifying 16-QAM signals, which are classified as 64-QAM signals instead.

We next compute a rough energy estimate of the proposed equalizer with the assumption that each clock cycle consumes 20 pJ/cycle as was the case in the first version of our chip. If we assume that an accumulation of N symbols takes N clock cycles, then each iteration needs around N clock cycles. Since convergence requires around 150 iterations, that sums up to $150N$ clock cycles, where N is 1000 in our examples, so $150,000$ clock cycles needed for each equalizer. Since we need to run a blind equalization for each of the 3 modulation levels, $450,000$ total cycles are required for classification. Assuming the 20 pJ/clock cycle number, the energy consumption is estimated at 9 μJ, as compared to 0.15 μJ for the Kuiper

Table 7.4: Energy comparison of AWGN vs. multipath fading at SNR of 10 dB and 0 dB.

Processing Block	AWGN (SNR 10 dB)	Multipath (SNR 10 dB)	AWGN (SNR 0 dB)	Multipath (SNR 0 dB)
MC/SC identification	10 nJ	200 nJ	0.24 uJ	5.04 uJ
$1/T$ Estimation	2.3 uJ	9.2 uJ	19.5 uJ	78.5 uJ
f_c Estimation	8 uJ	32 uJ	96 uJ	384 uJ
Mod. Type Class.	60 nJ	132 nJ	240 nJ	528 nJ

classifier [URP11] that works in AWGN.

Table 7.4 summarizes the total energy consumption of the proposed classifier (with the exception of the level classification) at SNRs of 0 and 10 dB for both AWGN and worst case ETU multipath fading.

7.3 Summary

We have analyzed in this chapter the performance of our proposed spectrum sensing and modulation classifier in fading environments. We have analyzed the sensing performance of energy detection under severe fading environments, and have shown that collaborative detection can substantially improve the detection performance under fading environments. With respect to modulation classification, we have addressed the challenges with blind channel equalization in the context of modulation classification. Then, we have quantified the additional energy consumption required to meet the desired classification accuracy under severe multipath environments, and have analyzed the performance of blind channel equalization algorithms that we used to determine the modulation level of the received signal.

CHAPTER 8

Conclusions

8.1 Research Contributions

In this thesis, we have analyzed some of the challenges associated with wideband cyclostationary spectrum sensing and modulation classification. We have looked at algorithmic challenges that arise due to wideband circuitry imperfections, and also energy challenges that arise due to blindly processing the wideband spectrum. Overall, the findings provided in this thesis can be used to design future wideband cognitive radios that are both energy efficient, and robust to various wideband impairments. The contributions of this thesis are listed below

- We have presented in this thesis some of the challenges that arise when cognitive radios operate in wideband channels. Imperfect knowledge of the transmit parameters such as the signal's symbol rate and carrier frequency are shown to degrade the performance of cyclostationary detectors, especially in the low SNR regimes. In fact, increasing the sensing time under non-zero cyclic frequency offsets results in a degradation in the cyclic feature to be detected. As a result, although increasing the sensing time suppresses the noise, the detection performance of cyclostationary detectors degrades with increasing sensing time under frequency offsets. It is shown that multi-frame processing of the incoming samples makes the signal detector more robust to cyclic frequency offsets. Further, we considered the sampling clock offset defined as an unknown offset in the sampling clock at the ADC stage as an additional impairment. Using the proposed detector, reliable signal

detection can be guaranteed until relatively large cyclic frequency offsets at low SNRs. We showed that the proposed multi-frame statistic achieves the most gains compared to the conventional detector when the cyclic frequency offset is more severe than the sampling clock offset. Further, we formulated an optimization problem that solves for the optimum method to split the incoming samples that achieves the best average detection performance, where the average is taken with respect to the distribution of both the cyclic frequency and sampling clock offsets.

- We have proposed a low-power modulation classification processor that can differentiate among multi-carrier and single-carrier modulations, estimate their transmit parameters, their modulation type, and determine if they are spread signals. Further, we have developed algorithms not presented in this thesis that can extract the symbols using the estimated parameters, and estimate the modulation order of the signal being classified. Unlike other cyclic-based modulation classifiers which assume accurate knowledge of the transmit parameters, we studied the tradeoffs between the estimation of the signal's symbol rate and carrier frequency, and the achievable classification accuracy. We showed that there exists a feasible region that determines which accuracies on the symbol rate and carrier frequency can be tolerated while achieving the required classification accuracy of 95%. Then, we formulated an optimization problem to minimze the total consumed energy. The result of this optimization resulted in an area in the feasible region in which the total energy is minimized. Further, we optimized the processor architecture by the co-design methodology to enhance block reusability and reconfigurability. These algorithms for this modulation classification processor are selected to have functional similarities in order to build a processing architecture that maximizes hardware utilization. Finally, we analyzed the impact of fading on the signal detection that is performed prior to the the modulation classification. We considered composite models

that take into account both small and large scale fading through the $\kappa - \mu$ fading model, and show the impact of different fading models on the detection performance of energy detectors. Further, we analyze the impact of multipath fading in frequency selective environments on the classification accuracy of the proposed processor, and proposed algorithmic methods to achieve the required classification accuracy under unkown channels.

- With respect to the analog impairments, we analyzed the impact of RF front-end nonlinearities on the detection performance of cyclostationary and energy detectors. Although nonlinearities can be mitigated by passing the received signal through an attenuator after the antenna, this solution results in a loss in dynamic range. The presence of strong blockers in the wideband spectrum can generate intermodulation terms that fall subbands within the bandwidth of interest. We have shown that that under low signal to interference ratios, front-end nonlinearities severely degrade the detection performance of both energy and cyclostationary detectors. We theoretically derived the probability of false alarm and detection of both detectors under a finite number of samples, and showed that the receiver operating characteristic curve is dependent not only on the strength of the blockers, but also on their modulation type. As a result, unlike the case where the interference is generated from adjacent strong signals, setting the detection threshold requires knowing the modulation type and order of the blockers. This further motivates the need for modulation classification, which can be utilized to guarantee the threshold, and therefore the operating point on the ROC curve. Further, we proposed an interference cancellation algorithm which re-generates the intermodulation term from the blockers at baseband, and subtracts it from the I/Q samples of the subband of interest. We have shown that the interference cancellation completely recovers the loss in detection performance when the blockers' signal to interference ratio is above 30 dB. Under lower ratios, the cancellation

algorithm shows a loss with respect to the ideal detection performance, but still improves on the performance of uncompensated detectors.

- We have also investigated the possible sampling rate reduction at the ADC that could be achieved when the wideband spectrum is sparse. We analyze a compressive sensing solution based on cyclostationary detection to reconstruct the spectral correlation function of the acquired sub-Nyquist samples. Contrary to the typical compressive sensing formulations which usually result in a LASSO formulation that cannot be solved in closed-form, we reconstructed the SCF of the wideband spectrum when the frequency support is known at the receiver. We formulated the SCF reconstruction problem as a least-square problem which has a closed-form solution, and is therefore easily implementable in hardware. Based on this formulation, we studied the uniqueness of the reconstructed SCF by analyzing the spark and restricted isometry property of the measurement matrix. The results show that cyclostationary detection from sub-Nyquist samples can be achieve more sampling rate reductions than energy detectors as a result of the additional sparsity on the SCF. In addition, the sampling rate can be reduced up to a compression ratio threshold that we refer to as the compression wall with minimal increase in the sensing time to operate at the same point on the receiver operating curve. When the compression ratio is pushed below the compression wall, the sensing time required to achieve the desired detection and false alarm probabilities increases exponentially. With respect to the computational complexity of the proposed sub-Nyquist detector, we have shown that minimum compression ratio can only be achieved with increasing FFT size on the DSP side which reduces the leakage in the SCF. As a result, there exists a tradeoff between the achievable compression ratio, and the computational complexity on the digital side.

8.2 Future Work

Although LNA nonlinearities are the most prominent source of nonlinearities in wideband receivers, other impairments such as mixer nonliearities, and I/Q mismatch can result in further degradation in the spectrum sensing performance. In order to get more intuition regarding the performance of spectrum sensing algorithms in commercial radio recievers, the effects of these impairments should be quantified, and the adaptive cancellation solution should be modified to compensate for the composite effect of the different analog impairments. Further, although the performance of the proposed interefence cancellation algorithm degrades when the blockers' self intereference is relatively high, signal demodulation and re-modulation can be performed knowing the blocker's modulation type and order. By doing so, the blockers' self-interference can be suppressed, and therefore removing the limitation of the proposed compensator.

The developed compressive sensing algorithm and its analysis was performed for the case where the frequency support of the wideband spectrum is known. An extension of this work could be to study the sampling rate reduction gains that can be achieved with blind cyclostationary compressive sensing algorithms that do not assume knowledge of the frequency support.

APPENDIX A

Appendix

A.1 Second Moment of Multi-Frame Statistic Under Noise Only

We start with the noise conjugate multi-frame test statistic under a zero lag $\nu = 0$ and we expand the term of interest as follows

$$|\hat{R}_{w^*}^{\alpha_k}(0)|^2 = \frac{1}{M^2N^2} \sum_{m_1=1}^{M} \sum_{m_2=1}^{M} \sum_{n_1=0}^{N-1} \sum_{n_2=0}^{N-1} |w_{m_1}[n_1]|^2 \times |w_{m_2}[n_2]|^2 e^{-j2\pi\alpha_k(n_1-n_2)T_s}. \tag{A.1}$$

When $m_1 \neq m_2$, $w_{m_1}[n_1]$ and $w_{m_2}[n_2]$ are independent for all $n_1, n_2 \in [0, ..., N-1]$. Therefore, $\mathbb{E}[|w_{m_1}[n]|^2|w_{m_2}[n]|^2] = \mathbb{E}[|w_{m_1}[n]|^2]\mathbb{E}[|w_{m_2}[n]|^2] = \sigma_w^4$.

The expectation is therefore computed as

$$\mathbb{E}[|\hat{R}_{w^*}^{\alpha_k}(0)|^2 \mid m_1 \neq m_2] = \frac{\sigma_w^4}{M^2N^2} \sum_{m_1=1}^{M} \sum_{\substack{m_2=1 \\ m_2 \neq m_1}}^{M} \sum_{n_1=0}^{N-1} \sum_{n_2=0}^{N-1} e^{-j2\pi\alpha_k(n_1-n_2)T_s} = \sigma_w^4 \frac{(M-1)}{MN^2} \cdot \frac{\sin^2(\pi\alpha_k NT_s)}{\sin^2(\pi\alpha_k T_s)} \tag{A.2}$$

When $m_1 = m_2$, we expand Eq. (A.1) as

$$|\hat{R}_{w^*}^{\alpha_k}(0)|^2 = \frac{1}{M^2N^2}\sum_{m=1}^{M}\sum_{n=0}^{N-1}|w_m[n]|^4 + \frac{1}{M^2N^2}\sum_{m=1}^{M}\sum_{n_1=0}^{N-1}\sum_{n_2=0}^{N-1}|w_m[n_1]|^2|w_m[n_2]|^2 e^{-j2\pi\alpha_k(n_1-n_2)T_s}. \tag{A.3}$$

It can be shown after some manipulations that the expectation of Eq. (A.3) is equal to

$$\mathbb{E}[|\hat{R}_{w^*}^{\alpha_k}(0)|^2 \mid m_1 = m_2] = \frac{2\sigma_w^4}{MN} + \frac{\sigma_w^4}{MN^2}\left(\frac{\sin^2(\pi\alpha_k NT_s)}{\sin^2(\pi\alpha_k T_s)} - N\right). \tag{A.4}$$

Finally, adding Eq. (A.2) and (A.4), we obtain

$$\mathbb{E}[|\hat{R}_{w^*}^{\alpha_k}(0)|^2] = \frac{\sigma_w^4}{MN} + \frac{\sigma_w^4\sin^2(\pi\alpha_k NT_s)}{N^2\sin^2(\pi\alpha_k T_s)}. \tag{A.5}$$

In a similar procedure, it can be shown that the second moment of the non-conjugate CAC is equal to

$$\mathbb{E}[|\hat{R}_{w}^{\alpha_k}(0)|^2] = \frac{2\sigma_w^4}{MN}, \tag{A.6}$$

which is independent of the cyclic frequency α_k.

Under non-zero lag ν, the second-order moment of the multi-frame CAC can be found as follows

$$|\hat{R}_{w^*}^{\alpha_k}(\nu)|^2 = \frac{1}{M^2N^2}\sum_{m_1=1}^{M}\sum_{m_2=1}^{M}\sum_{n_1=0}^{N-1}\sum_{n_2=0}^{N-1} w_{m_1}[n_1]w_{m_1}^*[n_1-\nu] w_{m_2}^*[n_2]w_{m_2}[n_2-\nu]e^{-j2\pi\alpha_k(n_1-n_2)T_s}.$$

When $m_1 \neq m_2$, $\mathbb{E}[|\hat{R}_{w^*}^{\alpha_k}(\nu)|^2] = 0$ as none of the indices coincide. Similarly, when $m_1 = m_2$, the second-order moment is only non-zero when $n_1 = n_2$. As a result,

we obtain the following result

$$|\hat{R}_{w^*}^{\alpha_k}(\nu)|^2 = \frac{1}{M^2N^2}\sum_{m=1}^{M}\sum_{n=0}^{N-1} w_m[n]w_m^*[n-\nu]w_m^*[n]w_m[n-\nu],$$

the expectation of which is given by

$$\mathbb{E}[|\hat{R}_{w^*}^{\alpha_k}(\nu)|^2] = \frac{\sigma_w^4}{MN}. \tag{A.7}$$

Similarly, it can be shown that the second-order moment of the non-conjugate multi-frame CAC under $\mathcal{H}_0$ under non-zero lag yields the same result as above, namely

$$\mathbb{E}[|\hat{R}_{w}^{\alpha_k}(\nu)|^2] = \frac{\sigma_w^4}{MN}. \tag{A.8}$$

A.2 Second Moment of Multi-Frame Statistic Under Noiseless Conditions With No Impairments

We start by finding the theoretical second moment of the conjugate CAC at any lag ν, which we expand as

$$\begin{aligned}\hat{R}_{s^*}^{\alpha_k}(\nu) =& \frac{1}{MN}\sum_{m=1}^{M}\sum_{n=0}^{N-1}\sum_{\ell=-\infty}^{\infty}\sum_{j=-\infty}^{\infty} a(\ell T)\times \\ & p(nT_s-\nu-\ell T)a^*(jT)p(nT_s-jT)e^{-j2\pi\alpha_k nT_s},\end{aligned} \tag{A.9}$$

where T denotes the symbol period of the signal of interest, and T_s denotes the sampling period. We assume a pulse shape $p(t)$ with support limited to $[0, T)$. Therefore,

$$p(nT_s-\nu-\ell T) \neq 0 \text{ when } \ell = \left\lfloor \frac{nT_s-\nu}{T} \right\rfloor, \tag{A.10}$$

and Eq. (A.9) gets simplified to

$$\hat{R}_{s^*}^{\alpha_k}(\nu) = \frac{1}{MN}\sum_{m=1}^{M}\sum_{n=0}^{N-1}\left|a\left(\left\lfloor\frac{nT_s}{T}\right\rfloor T\right)\right|^2 \times p\left(nT_s - \left\lfloor\frac{nT_s}{T}\right\rfloor T\right) p\left(nT_s - \left\lfloor\frac{nT_s-\nu}{T}\right\rfloor T\right) e^{-j2\pi\alpha_k nT_s}. \quad \text{(A.11)}$$

We can write

$$\begin{aligned}|\hat{R}_{s^*}^{\alpha_k}(\nu)|^2 = \frac{1}{M^2N^2}\sum_{m_1=1}^{M}\sum_{m_2=1}^{M}\sum_{n_1=0}^{N-1}\sum_{n_2=0}^{N-1}&\left|a\left(\left\lfloor\frac{n_1}{\mathcal{L}}\right\rfloor T\right)\right|^2 \times \\ &\left|a\left(\left\lfloor\frac{n_2}{\mathcal{L}}\right\rfloor T\right)\right|^2 p\left(n_1T/\mathcal{L} - \left\lfloor\frac{n_1}{\mathcal{L}}\right\rfloor T\right) \times \\ &p\left(n_1T/\mathcal{L} - \left\lfloor\frac{n_1}{\mathcal{L}} - \frac{\nu}{T}\right\rfloor T\right) p\left(n_2T/\mathcal{L} - \left\lfloor\frac{n_2}{\mathcal{L}}\right\rfloor T\right) \times \\ &p\left(n_2T/\mathcal{L} - \left\lfloor\frac{n_2}{\mathcal{L}} - \frac{\nu}{T}\right\rfloor T\right) e^{-j2\pi\alpha_k(n_1-n_2)T_s}. \quad \text{(A.12)}\end{aligned}$$

For ease of notation, we denote $|a(\lfloor\frac{n_1}{\mathcal{L}}\rfloor T)|^2$ and $|a(\lfloor\frac{n_2}{\mathcal{L}}\rfloor T)|^2$ by $|a(n_1)|^2$ and $|a(n_2)|^2$ respectively. We split Eq. (A.12) into two case: $m_1 = m_2$ and $m_1 \neq m_2$. In the following two cases, we drop the $\frac{1}{M^2N^2}$ factor.

Case 1: $m_1 = m_2$

For ease of notation, we denote by k both indices m_1 and m_2. Eq. (A.12) therefore becomes

$$\begin{aligned}|\hat{R}_{s^*}^{\alpha_k}(\nu)|^2 = &\sum_{m=1}^{M}\sum_{n=0}^{N-1}|a(n)|^4 g(n,n,\nu) + \\ &\sum_{m=1}^{M}\sum_{n_1=0}^{N-1}\sum_{\substack{n_2=0\\ n_2\neq n_1}}^{N-1}|a(n_1)|^2|a(n_2)|^2 g(n_1,n_2,\nu)e^{-j2\pi\alpha_k(n_1-n_2)T_s}. \quad \text{(A.13)}\end{aligned}$$

Using the fact that symbols are independent from each other, we obtain

$$\begin{aligned}\mathbb{E}[|\hat{R}_{s^*}^{\alpha_k}(\nu)|^2 \mid m_1 = m_2] = &u_4 M\sum_{n=0}^{N-1} g(n,n,\nu) + \\ &Mu_2^2\left[\sum_{n_1=0}^{N-1}\sum_{n_2=0}^{N-1} g(n_1,n_2,\nu) - \sum_{n=0}^{N-1} g(n,n,\nu)\right]. \quad \text{(A.14)}\end{aligned}$$

Using the definitions in (3.18), Eq. (A.14) simplifies to

$$\mathbb{E}[|\hat{R}_{s^*}^{\alpha_k}(0)|^2 \mid m_1 = m_2] = u_4 P_4 M + u_2^2 M[|P_2|^2 - P_4]. \tag{A.15}$$

Case 2: $m_1 \neq m_2$

Under Case 2, since the information symbols of different frames are independent, the second moment is equal to

$$\begin{aligned}\mathbb{E}[|\hat{R}_{s^*}^{\alpha_k}(\nu)|^2 | m_1 \neq m_2] =& u_2^2 M(M-1)u_4 \times \\ & \sum_{n_1=0}^{N-1} p\left(\frac{n_1 T}{\mathcal{L}} - \left\lfloor \frac{n_1}{\mathcal{L}} \right\rfloor T\right) p\left(\frac{n_1 T}{\mathcal{L}} - \left\lfloor \frac{n_1}{\mathcal{L}} - \frac{\nu}{T} \right\rfloor T\right) \times \\ & \sum_{n_2=0}^{N-1} p\left(\frac{n_2 T}{\mathcal{L}} - \left\lfloor \frac{n_2}{\mathcal{L}} \right\rfloor T\right) p\left(\frac{n_2 T}{\mathcal{L}} - \left\lfloor \frac{n_2}{\mathcal{L}} - \frac{\nu}{T} \right\rfloor T\right) e^{-j2\pi\alpha_k(n_1-n_2)T_s} \\ =& u_2^2 |P_2|^2 M(M-1). \end{aligned} \tag{A.16}$$

Finally, adding the results of Eq. (A.15) and (A.16) and bringing back the $\frac{1}{M^2N^2}$, we obtain the final result for the second moment of the conjugate CAC as

$$\mathbb{E}[|\hat{R}_{s^*}^{\alpha_k}(\nu)|^2] = \frac{P_4}{MN^2}[u_4 - u_2^2] + \frac{|P_2|^2 u_2^2}{N^2}. \tag{A.17}$$

The result for the second moment of the non-conjugate CAC can be obtained in a similar fashion. In fact, the final expression in Eq. (A.17) still holds for the non-conjugate CAC second moment where P_2 is replaced by P_2'.

References

[ATJ] S. Atapattu, C. Tellambura, and H. Jiang. "Relay based cooperative spectrum sensing in cognitive radio networks." In *IEEE GLOBECOM 2009*.

[ATJ11a] S. Atapattu, C. Tellambura, and H. Jiang. "Energy detection based cooperative spectrum sensing in cognitive radio networks." *IEEE Trans. Commun.*, **10**(4):1232–1241, April 2011.

[ATJ11b] S. Atapattu, C. Tellambura, and H. Jiang. "Spectrum Sensing via Energy Detector in Low SNR." In *International Conference on Communications*, June 2011.

[BBB01] G. Burel, C. Bouder, and O. Berder. "Detection of direct sequence spread spectrum transmissions without prior knowledge." In *Proc. IEEE GLOBECOM*, San Antonio, TX, USA, November 25–29 2001.

[BC06] A. Beasley and A. Cole-Rhodes. "SPC06-2: Blind Adaptive Equalization for QAM Signals Using an Alphabet-Matched Algorithm." In *Global Telecommunications Conference*, pp. 1–5, 2006.

[BCC07] A. Barbieri, G. Colavolpe, and G. Caire. "Joint Iterative Detection and Decoding in the Presence of Phase Noise and Frequency Offset." *IEEE Trans. Commun.*, **55**(1):171–179, Jan 2007.

[BLK12] D. Bai, J. Lee, S. Kim, and I. Kang. "Near ML modulation classification." In *IEEE VTC Fall*, 2012.

[BW98] B.F. Beidas and C.L. Weber. "Asynchronous classification of MFSK signals using the higher order correlation domain." *IEEE Trans. Commun.*, **46**(4):480–493, 1998.

[Cha97] "Guidelines For Evaluation Of Radio Transmission Technologies For IMT-2000." Technical Report ITU-R M.1225, 1997.

[Cha07] "User Equipment (UE) radio transmission and reception." Technical Report R4-070872, 2007.

[CMB04] D. Cabric, S. Mishra, and R. Brodersen. "Implementation issues in spectrum sensing for cognitive radios." In *Proc. ACSSC*, Pacific Grove, CA, USA, November 7–10, 2004.

[CRJ11] D. Cohen, E. Rebeiz, V. Jain, Y. C. Eldar, and D. Cabric. "Cyclostationary Feature Detection from Sub-Nyquist Samples." In *Proc. IEEE 4th International Workshop on Computational Advances in Multi-Sensor Adaptive Processing*, 2011.

[CS04] P. Ciblat and E. Serpedin. "A fine blind frequency offset estimator for OFDM/OQAM systems." *IEEE Trans. Signal Processing*, **52**(1):291–296, January 2004.

[CT06] E.J. Candes and T. Tao. "Near-Optimal Signal Recovery From Random Projections: Universal Encoding Strategies?" *IEEE Trans. Inform. Theory*, **52**(12):5406 – 5425, Dec 2006.

[CZL09] X. Chen, L. Zhao, and J. Li. "A Modified Spectrum Sensing Method for Wideband Cognitive Radio Based on Compressive Sensing." In *IEEE International Conference on Communications and Networking in China*, 2009.

[DAB05] O.A. Dobre, A. Abdi, Y. Bar-Ness, and Wei Su. "Blind modulation classification: a concept whose time has come." In *Advances in Wired and Wireless Communication, 2005 IEEE Sarnoff Symposium on*, April 2005.

[DAB07] O.A. Dobre, A. Abdi, Y. Bar-Ness, and W. Su. "Survey of automatic modulation classification techniques: classical approaches and new trends." *Communications, IET*, **1**(2):137 –156, Apr 2007.

[DAS07] F. F. Digham, M. S. Alouini, and M. K. Simon. "On the energy detection of unknown signals over fading channels." *IEEE Trans. Commun.*, **55**(1):21–24, January 2007.

[DB12] M.F. Duarte and R.G. Baraniuk. "Kronecker Compressive Sensing." *IEEE Trans. Image Processing*, **21**(2):494 – 504, Feb. 2012.

[DG94] A. V. Dandawate and G. B. Giannakis. "Statistical tests for presence of cyclostationarity." *IEEE Trans. Signal Processing*, **42**(9):2355–2369, September 1994.

[DMR00] A. Demir, A. Mehrotra, and J. Roychowdhury. "Phase noise in oscillators: a unifying theory and numerical methods for characterization." *IEEE Trans. Circuits Syst. I*, **47**(5):655–674, May 2000.

[DNL10] M. Derakhshani, M. Nasiri-Kenari, and Tho Le-Ngoc. "Cooperative Cyclostationary Spectrum Sensing in Cognitive Radios at Low SNR Regimes." In *Proc. IEEE ICC*, Cape Town, South Africa, May 23–27, 2010.

[Don06] D.L. Donoho. "Compressed sensing." *IEEE Trans. Inform. Theory*, **52**(4):1289 – 1306, Apr 2006.

[FC11] M. F. Duarte and Y. C. Eldar. "Structured Compressed Sensing: From Theory to Applications." *IEEE Trans. Signal Processing*, **59**(9):4053–4085, Mar. 2011.

[FLP05] G. Fettweis, M. Lohning, D. Petrovic, M. Windisch, P. Zillmann, and W. Rave. "Dirty RF: a new paradigm." In *Proc. IEEE PIMRC*, 2005.

[Gar88] W. A. Gardner. *Statistical spectral analysis: a non probabilistic theory.* Prentice Hall, 1988.

[Gar91] W. A. Gardner. "Exploitation of spectral redundancy in cyclostationary signals." *IEEE Signal Processing Mag.*, **8**(2):14–36, April 1991.

[gha11] A. Shahed hagh ghadam. *Contributions to Analysis and* DSP*-based Mitigation of Nonlinear Distortion in Radio Transceivers.* Ph.D. dissertation, Tampere University of Technology, 2011.

[HB11] K. T. Hemachandra and N. C. Beaulieu. "Novel analysis for performance evaluation of energy detection of unknown deterministic signals using dual diversity." In *IEEE VTC Fall*, 2011.

[Hog81] E. Hogenauer. "An economical class of digital filters for decimation and interpolation." *IEEE Trans. Acoust., Speech, Signal Processing*, **29**(2):155–162, April 1981.

[HP95] Chung-Yu Huan and A. Polydoros. "Likelihood methods for MPSK modulation classification." *IEEE Trans. Commun.*, **43**(234):1493–1504, 1995.

[HR] S. P. Herath and N. Rajatheva. "Analysis of equal gain combining in energy detection for cognitive radio over Nakagami channels." In *IEEE GLOBECOM 2008.*

[HRT11] S. P. Herath, N. Rajatheva, and C. Tellambura. "Energy detection of unknown signals in fading and diversity reception." *IEEE Trans. Commun.*, **59**(9):2443–2453, September 2011.

[Jai12] V. Jain. *"Compressive Wideband Spectrum Sensing based on Cyclostationary Detection."*. Master's thesis, University of California, Los Angeles, 2012.

[JM09] Sadegh Jokar and Volker Mehrmann. "Sparse solutions to underdetermined Kronecker product systems." *Linear Algebra and its Applications*, **431**(12):2437 – 2447, 2009.

[JSE98] R. Johnson, P. Schniter, T.J. Endres, J.D. Behm, D.R Brown, and R.A. Casas. "Blind equalization using the constant modulus criterion: a review." *Proceedings of the IEEE*, **86**(10):1927–1950, 1998.

[KH09] Eart Art Keehr and Ali Hajimiri. "Digitally assisted equalization of third-order intermodulation products in wideband direct conversion receivers." *Int. Journal of Microw. and Wireless Tech.*, **1**(Special Issue 04):377–385, June 2009.

[KKY03] Namjin Kim, N. Kehtarnavaz, M.B. Yeary, and S. Thornton. "DSP-based hierarchical neural network modulation signal classification." *IEEE Trans. Neural Networks*, **14**(5):1065–1071, September 2003.

[KS98] Young-Hoon Kim and S. Shamsunder. "Adaptive algorithms for channel equalization with soft decision feedback." *IEEE J. Select. Areas Commun.*, **16**(9):1660–1669, 1998.

[Lan67] H.J. Landau. "Necessary Density Conditions for Sampling and Interpolation of Certain Entire Functions." *Acta Math*, **117**:37–52, Jul. 1967.

[LKD07] Jason Laska, Sami Kirolos, and Marco Duarte. "Theory and Implementation of an Analog-to-Information Converter using Random Demodulation." In *Proc. IEEE ISCAS*, 2007.

[LKS09] F. Lehmann, A. Kazem, and G. Salut. "Blind turbo-detection in the presence of phase noise." *Communications, IET*, **3**(8):1343–1353, 2009.

[LTY11] J. Lee, D. Toumpakaris, and W. Yu. "Interference Mitigation via Joint Detection." *IEEE J. Select. Areas Commun.*, **29**(6):1172 –1184, June 2011.

[MC11] M. Mishali and Y. C. Eldar. "Wideband Spectrum Sensing at Sub-Nyquist Rates." *IEEE Signal Processing Mag.*, **28**(4):102–135, Jul. 2011.

[MCD11] M. Mishali, Y. C. Eldar, O. Dounaevsky, and E. Shoshan. "Xampling: Analog to digital at sub-Nyquist rates." *Circuits, Devices Systems, IET*, **5**(1):8–20, Jan. 2011.

[ME10] Moshe Mishali and Yonina Eldar. "From Theory to Practice: Sub-Nyquist Sampling of Sparse Wideband Analog Signals." **4**(2):375–391, April 2010.

[MKH10] D.H. Mahrof, E. A. M. Klumperink, J. C. Haartsen, and B. Nauta. "On the Effect of Spectral Location of Interferers on Linearity Requirements for Wideband Cognitive Radio Receivers." In *Proc. DySPAN*, April1–9 2010.

[MM98] M. Morelli and U. Mengali. "Feedforward frequency estimation for PSK: A tutorial review." *European Transactions on Telecommunications*, **9**(2):103–116, March 1998.

[MM99] J. Mitola III and G. Q. Maguire Jr. "Cognitive radio: making software radios more personal." *IEEE Personal Commun. Mag.*, **6**(4):13–18, August 1999.

[Mos96] S. Moshavi. "Multi-user detection for DS-CDMA communications." *IEEE Commun. Mag.*, **34**(10):124–136, oct 1996.

[MTM06] Mark A. McHenry, Peter A. Tenhula, Dan McCloskey, Dennis A. Roberson, and Cynthia S. Hood. "Chicago spectrum occupancy measurements & analysis and a long-term studies proposal." In *Proceedings of the first international workshop on Technology and policy for accessing spectrum*, TAPAS '06, New York, NY, USA, 2006. ACM.

[NA98] A.K. Nandi and E. E. Azzouz. "Algorithms for automatic modulation recognition of communication signals." *IEEE Trans. Commun.*, **46**(4):431–436, 1998.

[OD11] M. Oner and O. Dobre. "On the Second-Order Cyclic Statistics of Signals in the Presence of Receiver Impairments." *IEEE Trans. Commun.*, **59**(12):3278–3284, December 2011.

[One09] M. Oner. "On the Effect of Random Sampling Jitter on Cyclostationarity Based Spectrum Sensing Algorithms for Cognitive Radio." In *Proc. IEEE VTC Spring*, Barcelona, Spain, April 26–29, 2009.

[Pic94] B. Picinbono. "On circularity." *IEEE Trans. Signal Processing*, **42**(12):3473–3482, 1994.

[PK90] A. Polydoros and K. Kim. "On the detection and classification of quadrature digital modulations in broad-band noise." *IEEE Trans. Commun.*, **38**(8):1199–1211, 1990.

[QCP08] Zhi Quan, Shuguang Cui, H.V. Poor, and A.H. Sayed. "Collaborative wideband sensing for cognitive radios." *IEEE Softw.*, **25**(6):60–73, 2008.

[Ram09] B. Ramkumar. "Automatic modulation classification for cognitive radios using cyclic feature detection." *IEEE Circuits Syst. Mag.*, **9**:27 –45, 2nd Quarter 2009.

[Raz98] B. Razavi. *RF Microelectronics*. Englewood Cliffs, New Jersey: Prentice Hall, 1998.

[Raz10] Behzad Razavi. "Cognitive Radio Design Challenges and Techniques." **45**(8):1542–1553, August 2010.

[RC11a] E. Rebeiz and D. Cabric. "Blind Modulation Classification Based on Spectral Correlation and Its Robustness to Timing Mismatch." In *Proc. IEEE MILCOM*, Baltimore, MD, USA, November 7–10, 2011.

[RC11b] E. Rebeiz and D. Cabric. "Low Complexity Feature-Based Modulation Classifier and Its Non-Asymptotic Analysis." In *Proc. IEEE GLOBECOM*, Houston, TX, USA, December 5–9, 2011.

[RKJ09] K. Ruttik, K. Koufos, and R. Jantti. "Detection of unknown signals in a fading environment." *IEEE Commun. Lett.*, 2009.

[RSV13] E. Rebeiz, A. Shahed, M. Valkama, and D. Cabric. "Suppressing RF Front-End Nonlinearities in Wideband Spectrum Sensing." In *Proc. Crowncom*, Washington, DC, USA, 2013.

[RYU13] E. Rebeiz, F-L. Yuan, P. Urriza, D. Markovic, and D. Cabric. "Energy-Efficient Processor for Blind Signal Classification in Cognitive Radio Networks." *IEEE Trans. Circuits Syst. I*, 2013.

[SBS00] A. Swami, S. Barbarossa, and B.M. Sadler. "Blind source separation and signal classification." In *Signals, Systems and Computers Conference*, volume 2, pp. 1187–1191 vol.2, 2000.

[SCZ10] Chengqi Song, Dawei Chen, and Qian Zhang. "Understand the Predictability of Wireless Spectrum: A Large-Scale Empirical Study." In *IEEE ICC*, pp. 1 –5, May 2010.

[SH92] S.S. Soliman and S.-Z. Hsue. "Signal classification using statistical moments." *IEEE Trans. Commun.*, **40**(5):908–916, 1992.

[SK11] Qinghua Shi and Y Karasawa. "Noncoherent Maximum Likelihood Classification of Quadrature Amplitude Modulation Constellations: Simplification, Analysis, and Extension." *IEEE Trans. Wireless Commun.*, **10**(4):1312–1322, April 2011.

[SLB08] Miao Shi, A. Laufer, Y. Bar-Ness, and Wei Su. "Fourth order cumulants in distinguishing single carrier from OFDM signals." In *Proc. IEEE MILCOM*, San Diego, CA, USA, November 17–19, 2008.

[SRZ13] P.C. Sofotasios, E. Rebeiz, Li Zhang, T.A. Tsiftsis, D. Cabric, and S. Freear. "Energy Detection Based Spectrum Sensing Over κ -μ and κ -μ Extreme Fading Channels." *IEEE Trans. Veh. Technol.*, **62**(3):1031–1040, 2013.

[SS00] A. Swami and B.M. Sadler. "Hierarchical digital modulation classification using cumulants." *IEEE Trans. Commun.*, **48**(3):416–429, March 2000.

[SVT09] V. Syrjala, M. Valkama, N.N. Tchamov, and J. Rinne. "Phase noise modelling and mitigation techniques in OFDM communications systems." In *Proc. of Wireless Telecom. Symposium*, pp. 1 –7, 2009.

[TA83] J. Treichler and B. Agee. "A new approach to multipath correction of constant modulus signals." *IEEE Trans. Acoust., Speech, Signal Processing*, **31**(2):459–472, 1983.

[TCB07] A. Tkachenko, D. Cabric, and R. Brodersen. "Cyclostationary Feature Detector Experiments using Reconfigurable BEE2." In *Proc. IEEE DySPAN*, Dublin, Ireland, April 17–20, 2007.

[Tia11] Zhi Tian. "Cyclic Feature based Wideband Spectrum Sensing using Compressive Sampling." In *Proc. IEEE ICC*, 2011.

[TP12] Andreas M. Tillmann and Mark E. Pfetsch. "The Computational Complexity of the Restricted Isometry Property, the Nullspace Property, and Related Concepts in Compressed Sensing." *ArXiv e-prints*, May 2012.

[TS08] R. Tandra and A. Sahai. "SNR Walls for Signal Detection." **2**(1):4–17, February 2008.

[URC11] Paulo Urriza, Eric Rebeiz, and Danijela Cabric. "Hardware implementation of Kuiper-based modulation level classification." In *Proc. ACSSC*, Pacific Grove, CA, USA, November 6–9, 2011.

[URP11] Paulo Urriza, Eric Rebeiz, P. Pawelczak, and D. Cabric. "Computationally Efficient Modulation Level Classification Based on Probability Distribution Distance Functions." *IEEE Commun. Lett.*, **15**(5):476–478, may 2011.

[VRD10] J. Verlant-Chenet, J. Renard, J.-M. Dricot, P. De Doncker, and F. Horlin. "Sensitivity of Spectrum Sensing Techniques to RF Impairments." In *Proc. IEEE VTC Spring*, Taipei, Taiwan, May 16–19, 2010.

[VRK01] Mart Valkama, Mart Renfors, and Vart Koivunen. "Advanced methods for I/Q imbalance compensation in communication receivers." *IEEE Trans. Signal Processing*, **49**(10):2335–2344, October 2001.

[WM00a] Wen Wei and J. M. Mendel. "Maximum-likelihood classification for digital amplitude-phase modulations." *IEEE Trans. Commun.*, **48**(2):189–193, February 2000.

[WM00b] Wen Wei and J.M. Mendel. "Maximum-likelihood classification for digital amplitude-phase modulations." *IEEE Trans. Commun.*, **48**(2):189–193, 2000.

[WP11] Dennis Wieruch and Volker Pohl. "A Cognitive Radio Architecture based on sub-Nyquist Sampling." In *Proc. IEEE DySPAN*, 2011.

[WRP09] Matthias Wellens, Janne Riihijrvi, and Petri Mhnen. "Empirical time and frequency domain models of spectrum use." *Physical Communication*, **2**(1-2):10 – 32, 2009.

[XSZ10] J.L. Xu, Wei Su, and MengChu Zhou. "Software-Defined Radio Equipped With Rapid Modulation Recognition." *IEEE Trans. Veh. Technol.*, **59**(4):1659 –1667, May 2010.

[YA09] T. Yucek and H. Arslan. "A survey of spectrum sensing algorithms for cognitive radio applications." **11**(1):116–130, First Quarter 2009.

[Yac07] M. D. Yacoub. "The $\kappa-\mu$ distribution and the $\eta-\mu$ distribution." *IEEE Antennas Propagat. Mag.*, **49**(1):68–81, February 2007.

[Yan05] J. Yang. "Spatial Channel Characterization for Cognitive Radios." Technical Report UCB/ERL M05/8, EECS Department, University of California, Berkeley, Jan 2005.

[YH09] Z. Yu and S. Hoyos. "Compressive Spectrum Sensing Front-ends for Cognitive Radios." In *IEEE International Conference on Systems, Man, and Cybernetics*, 2009.

[YL98] Yawpo Yang and Ching-Hwa Liu. "An asymptotic optimal algorithm for modulation classification." *IEEE Commun. Lett.*, **2**(5):117–119, 1998.

[YSR11] Tsung-Han Yu, O. Sekkat, S. Rodriguez-Parera, D. Markovic, and D. Cabric. "A Wideband Spectrum-Sensing Processor With Adaptive Detection Threshold and Sensing Time." *IEEE Trans. Circuits Syst. I*, **58**(11):2765–2775, November 2011.

[ZL10] Y. Zeng and Y. C. Liang. "Robustness of the cyclostationary detection to cyclic frequency mismatch." In *Proc. IEEE PIMRC*, Istanbul, Turkey, September 26–29, 2010.

[ZMS09] Qiyue Zou, Mart Mikhemar, and Art Hart Sayed. "Digital compensation of cross-modulation distortion in software-defined radios." *IEEE Journal of Selected Topics in Signal Processing*, **3**(32):348–361, June 2009.

[ZTD10a] A. Zahedi-Ghasabeh, A. Tarighat, and B. Daneshrad. "Sampling clock frequency offset compensation for feature detection in spectrum sensing." In *Proc. IEEE ICC*, Cape Town, South Africa, May 23–27, 2010.

[ZTD10b] A. Zarashi-Ghasabeh, A. Tarighat, and B. Daneshrad. "Cyclostationary sensing of OFDM waveforms in the presence of receiver RF impairments." In *IEEE Proc. WCNC'10*, April1–6 2010.

[ZTD12] A. Zahedi-Ghasabeh, A. Tarighat, and B. Daneshrad. "Spectrum Sensing of OFDM Waveforms Using Embedded Pilots in the Presence of Impairments." *IEEE Trans. Veh. Technol.*, **61**(3):1208–1221, March 2012.